UNIVERSITÀ DEGLI STUDI DI PADOVA

Scuola di Ingegneria
Dipartimento di Ingegneria dell'Informazione
Dipartimento di Ingegneria Industriale

Corso di Laurea Magistrale in Bioingegneria

BIOMECHANICS OF THE LOWER URINARY TRACT: INVESTIGATION OF FLOW CONDITIONS DURING URINATION AND ANALYSIS OF SPHINCTERIC OCCLUSION ACTIONS

Relatore: Ch.mo Prof. EMANUELE LUIGI CARNIEL

Laureanda: BEATRICE SABBADINI

Anno accademico 2016-2017

ABSTRACT

Urinary dysfunction can lead to incontinence, with relevant impact on the quality of life. This severe dysfunction can be surgically overcome by using an artificial urinary sphincter. However, several complications may result from an inappropriate prosthesis functionality, in many cases due to an unsuitable mechanical action of the device on urethral tissues.

Computational models allow the investigation of mechanical interaction between biological tissues and biomedical devices, representing a potential support for surgical practice and prosthesis design.

The present activities aim at investigating the mechanism of sphincter occlusion action and the urine flow conditions during urination. Results from preliminary experimental activities are processed adopting specific model formulations, also providing the definition of parameters that identify elastic and viscous tissues behavior.

The results obtained represent a preliminary support for the information to be assumed for prosthesis design, integrating surgical and biomechanical competences.

CONTENTS

INTRODUCTION

Urinary incontinence (UI) is defined by the International Continence Society as "the complaint of involuntary leakage of urine" (Abrams et al., 2002; Hampel et al.,2004).

UI is a pathology affecting a large part of the population worldwide and significantly reducing the quality of life (Landefeld et al., 2008).

Urinary incontinence is increasingly recognized as a health and economic problem, which affects the physical, psychological, social and economic well-being of individuals and their families and poses a substantial economic burden on health and social services (Hampel et al., 2004).

Incontinence affects about 400 million people worldwide; it is common in both men and women, with an incidence increasing with age. Prevalence of urinary incontinence in women living in the community increases with age, from 19% at age younger than 45 years to 29% in age 80 years or older; the rate levels off from age 50 to 70 years, after which prevalence again increases. Current national estimates are that more than 20 million women have urinary incontinence or have experienced it at some point in their lives. For women, stress incontinence decreases with age, whereas urge incontinence increases with age. Information comparing prevalence in racial or ethnic groups suggests that urinary incontinence is prevalent in all ethnic groups, with some suggestion of higher rates among white women.

The epidemiology of urinary incontinence in men has not been studied to the same extent as that in women. In men living in the community, the prevalence of urinary incontinence is 5% to 15% and exhibits a more steady increase with age than among women: 5% at younger than 45 years of age to 21% in men age 65 years or older.

This increase primarily reflects urge incontinence and mixed urinary incontinence, with stress incontinence decreasing after age 65 years. Nationally, the prevalence of urinary incontinence in men during their lifetime is approximately 6 million. Few studies have examined racial or ethnic differences in prevalence of urinary incontinence among men, so reliable comparisons cannot be made.

Prevalence of urinary incontinence in nursing homes is much higher than that in the community. Rates are 60% to 78% in women and 45% to 72% in men and increase with age. This may be due, in part, to impaired mobility and difficulty getting to the toilet.

Urinary incontinence can also be a reason for admission to a nursing home or a complication of other conditions that prompt admission.

The few studies that have evaluated racial or ethnic differences suggest that such differences are minimal. As a first suggestion, it is found that the risk factors in many existing studies can be categorized as

- physical status (for example, age, sex, obesity, limited physical activity),
- genetic factors (for example, family history),
- neuropsychiatric conditions (for example, multiple sclerosis, spinal cord injury, dementia, depression, stroke, diabetic neuropathy),
- trauma (for example, childbirth, prostatectomy, radiation),
- associated causalities (for example, diarrhea, inflammatory bowel disease, the irritable bowel syndrome, menopause, smoking, constipation) (Landefeld et al., 2008).

Different congenital or acquired pathologies determine anatomical and functional alterations of the bladder-sphincter-urethra apparatus with consequent debilitating incontinence.

Lower urinary tract dysfunction (LUTD) may cause storage (51% of men and 59% of women), voiding (26% of men and 20% of women) and post-micturition symptoms (17% of men and 14% of women). Patients with LUTD symptoms suffer because of a decrease in life quality.

The most effective surgical solution currently considered for men is the artificial urinary sphincter. The artificial urinary sphincter devices allow continence by means of an occlusion obtained by the application of a constant pressure on urethral duct.

The AMS 800™ (American Medical Systems, USA) is the most renowned artificial urinary sphincter, which has been implanted to almost 150,000 patients during last 40 years (Figure 1).

Scott, Bradley and Timm were the first to perform the artificial urinary sphincter implantation in 1972 (Ostrowski et al., 2015). The AMS 800™ Urinary Control System restores continence with an occlusive cuff and a corresponding pump that the patient controls. This device is a completely concealed, implantable, fluid-filled, solid silicone elastomer device that treats male stress urinary incontinence resulting from internal sphincter deficiency.

It mimics normal sphincter function by opening and closing the urethra at the control of the patient.
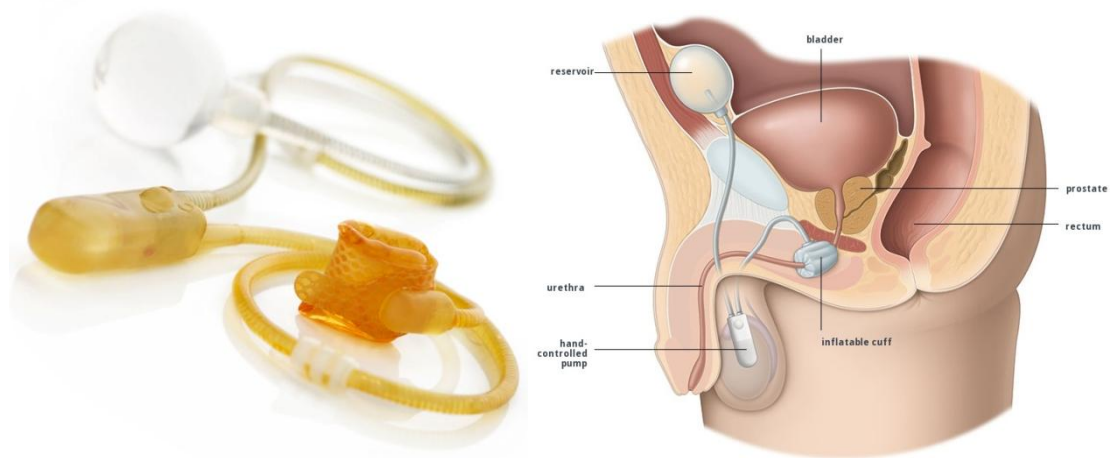
Figure 1 AMS 800^{TM} device and its placement.

The use of the cuff involves potential complications as atrophy and erosion that entail surgical revision, removal and possible replacement of the device. Urethral atrophy consists in the circumferentially reduction of bulk tissue properties in time. As a consequence of tissue atrophy, a cuff that was initially sized appropriately may become inadequate for ensuring continence.

The intensity and distribution of the force induced within the region of application determine a different occlusion process and potential degradation of the urethral tissue, mostly at the borders of the cuff. With the engineering approach can be paid attention to the interaction occurring between the cuff and the urethral tissues, through the implementation of a computational model.

The mechanical functionality of the prosthetic device and the biomechanical response of urethra to imposed pressure can be approached by means of experimental and computational biomechanics investigation.

Computational models of the urethra can be developed to identify the artificial sphincter pressure that ensures lumen occlusion and stress and strain distributions within biological tissues.

Moreover with this approach, it is possible to identify the sphincter pressure conditions that ensure continence, as well as the device conformation to minimize the prosthesis invasiveness. A computational approach to the analysis of flow conditions of healthy male urethra and urethra response during lumen occlusion is proposed below.

To realize a computational model of the urethra, it is necessary to know the geometry of the duct and the mechanical behavior of the constituent tissues.

In Chapter 1 is reported the anatomy of the lower urinary tract and the grave problem of incontinence.

Regarding the geometry of the duct, it is a tube with different constitutive tissue, deducted from histological analysis while regarding the mechanical behavior, tensile tests on tissue are needed and these are described in Chapter 2. Moreover, to validate the model it is necessary to have inflation tests, described in Chapter 2.

Then, developed and validated the model, are necessary suitable algorithms to evaluate the relationship between lumen volume and applied sphincter pressure to assess what is happening inside the urethra into mechanical functionality developed from the cuff, described in Chapter 3.

In this chapter are reported four structural models with different length.

In Chapter 4 is described the functionality of the healthy urethra and then the correlation between the inlet pressure of the urethra and urine flow. Seven different models are reported to evaluate the difference of urine flow rate.

CHAPTER 1

LOWER URINARY TRACT

1.1 Anatomy

The urethra is a tubular structure through which urine is expelled after accumulating in the bladder (Dunnick et al., 1997).

The male urethra has a mean length of 16–18 cm and is subdivided into posterior and anterior urethra.

Posterior urethra stretches from the bladder neck to the lower edge of the urogenital diaphragm and includes:

- Prostatic urethra: 3–4 cm long in the young male; this reaches 8–10 cm in cases of benign prostatic hyperplasia. It begins at the vesical neck and passes through the prostate gland assuming an arcuate course up to the prostate apex.

  Two parts are identified: the supramontanal tract from which the periurethral gland ducts emerge and the submontanal tract where the excretory ducts of the peripheral gland are located. The submontanal urethra is surrounded by the striated sphincter.

- Membranous urethra, approximately 1–2 cm long, which passes through the urogenital diaphragm which contains the Cowper glands. In this tract the urethra is surrounded by striate sphincter and the perineal muscles.

Anterior urethra, 14–15 cm long, is subdivided into:

- Bulbar urethra, which is of larger diameter (1.5-2 cm), is surrounded by the bulb of the corpus spongiosum, does not have stiff fascia, and extends from the perineal area to the suspensor ligament of the penis.

- Penile or pendulous urethra, stretching from the penile ligament to the external urethral meatus. Before its emergence at the meatus, there is an ampullar dilatation called fossa navicularis. Its diameter is relatively uniform, approximately 1 cm, and many small glands (of Littre) are located at its lumen, more numerous in the bulbar urethral area and near to the fossa navicularis (Figure 2) (Pavlica et al., 2003).

Male Urethra
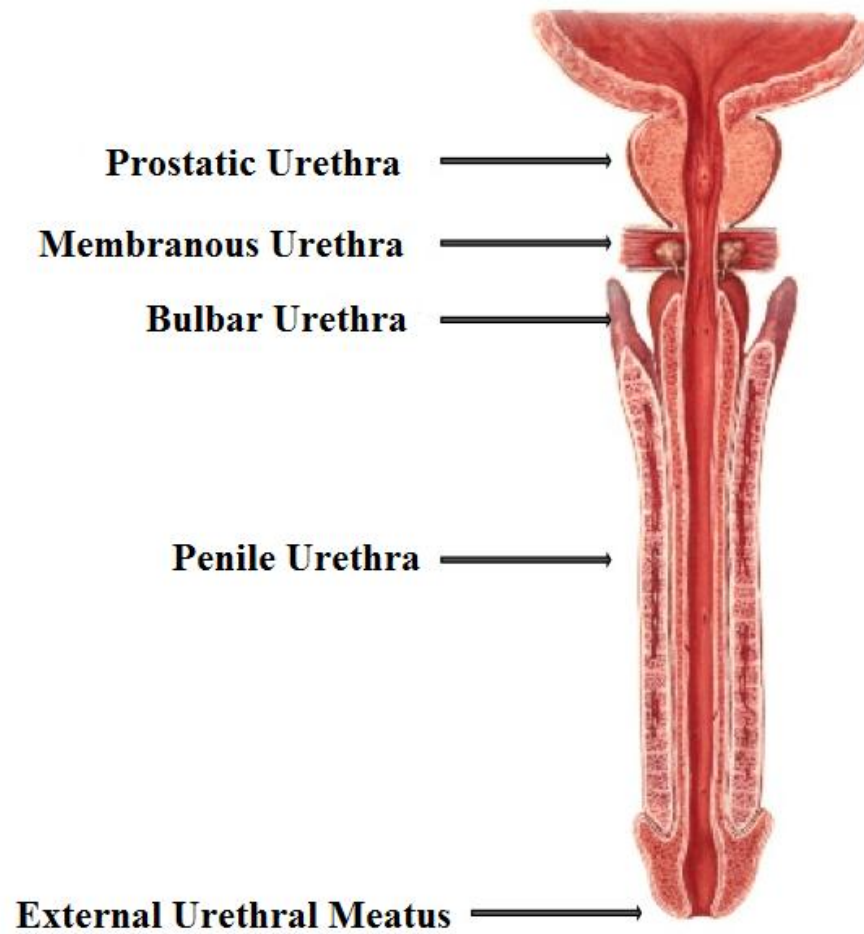
Figure 2 Anatomy of male urethra.

On account of its complex embryological origin, the urethral epithelial lining differs depending on the tract under consideration:

1. Transitional, from the bladder neck to the seminal verumontanum
2. Cylindrical, as far as the fossa navicularis
3. Squamous, up to the external meatus

1.2 Incontinence

Urinary incontinence, often related to sphincter damage, is found in male patients, leading to a miserable quality of life and to huge costs for the healthcare system.

Urinary incontinence can affect persons of all ages and is most common in child-bearing women and older men and women. Urinary incontinence is generally classified as urge incontinence (when a person has the sudden urge to urinate and cannot get to the bathroom in time); stress incontinence (when a person leaks urine after strains, such as laughing, coughing, sneezing, or lifting); mixed incontinence (when a person has both urge and stress incontinence); and other incontinence (for example, when urine continues to leak after urination or leaks constantly) (Landefeld et al., 2008; Brooks et al., 2007).

The most effective surgical solution currently considered for men is the artificial urinary sphincter that exerts a pressure field on the urethra, occluding the duct.

The action induced by artificial sphincteric devices to provide urinary continence is related to the problem of evaluating the interaction between the occlusive cuff and the urethral duct. The intensity and distribution of the force induced within the region of application determine a different occlusion process and potential degradation of the urethral tissue, mostly at the borders of the cuff.

Consequent mechanical effects on the urethral tissues may induce some modifications and possible degenerative.

In healthy conditions, the external sphincter muscle and the internal sphincter provide physiological occlusion. In case of severe incontinence (Figure 3), prosthetic devices are applied typically in the bulbar urethra region. Surgical solutions include artificial urinary sphincter and slings.
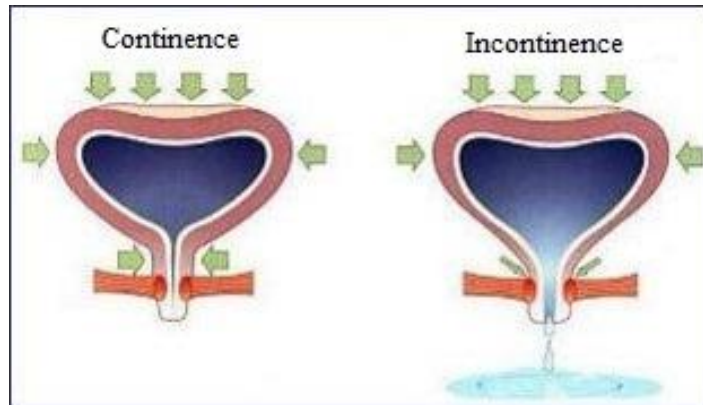
Figure 3 Representation of urinary incontinence.

The Artificial Urinary Sphincter (AUS) is generally considered a safe and reliable treatment for stress urinary incontinence. The AUS consists of an inflatable silicone cuff placed circumferentially at the bulbar urethra or nearby the bladder neck, a pressure-regulating balloon and a control unit composed by a deflating pump, a refill resistor and a deactivating button. The occlusive cuff ranges from 3.5 cm to 11 cm in length and is approximately 2.0 cm wide when deflated (Cordon et al., 2016; Hussain et al., 2005), providing lumen occlusion by an external pressure field, that can range up to 90 cmH$_2$O (Figure 4).
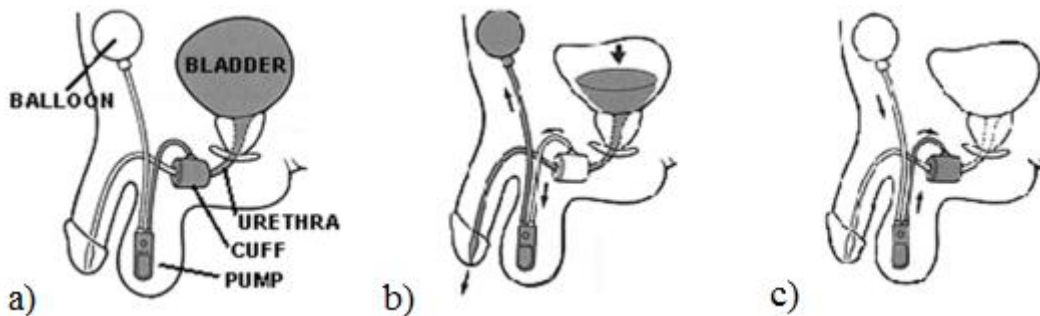
Figure 4 Operation of the artificial urinary sphincter AMS 800^{TM}. a) Configuration with sphincter closed; b) opening of the sphincter; c) closing of the sphincter.

The goal of pressure regulation is to provide the lowest amount of pressure that is sufficient for continence. The pressure field constantly acts on urethral tissues, while is suspended when the patient releases the device for inducing micturition. Particular attention should be paid to the interaction occurring between the cuff and the urethral tissues, in consideration of potential damages as atrophy and erosion. Urethral atrophy and erosion lie on a spectrum and are both most often secondary to the constant

compression experienced by the urethra, erosion being the more severe complication. The urethra may lose tissue bulk circumferentially with time, and a cuff that was initially sized appropriately may become too large for adequate urethral coaptation (Cordon et al., 2016; Bates et al., 2015). Complications entail surgical revision, removal and possible replacement of the device.

The AUS has undergone some improvements, as the addition of a fluoro-silicone gel in the inner surface of the cuff to prevent excessive internal friction induced by local bending. Moreover, a narrow-backed cuff was adopted, leading to a modified shape of the cuff shell that interacts with soft tissue in the border region with reduced shear effect, thus decreasing the risk of erosion and tissue atrophy. The cuff pressure is determined at the time of device implantation and set as constant value. Therefore, pressure cannot increase for any unexpected intensification of intra-abdominal pressure, thus inducing occasional incontinence episodes, and cannot be decreased for low intra-vesical urine volumes, with possible long-term risk of urethral atrophy. Despite positive post-surgery outcomes, a relevant proportion of patients requires revision surgery, due to complications including infection, urethral atrophy, erosion, and mechanical failure. In particular, urethral atrophy and tissue erosion are different effects of the same problem, due to persistent cuff-induced urethral compression (Cordon et al., 2016). Urethral atrophy consists in the circumferentially reduction of bulk tissue properties in time. As a consequence of tissue atrophy, a cuff that was initially sized appropriately may become inadequate for ensuring continence. Narrow-backed cuffs were specifically designed to provide a more stable mechanical action, by improving the stiffness of the posterior region. Over time, tissue degradation may become erosion, inducing degenerative effects that are related to the stress and strain distributions within urethral tissues during occlusion.

The mechanical functionality of the prosthetic device and the biomechanical response of urethra to imposed pressure can be approached by means of experimental and computational biomechanics investigation.

CHAPTER 2

EXPERIMENTAL TESTS

The experimental protocol includes the morphometric and histologic analysis of urethral tissues, the mechanical characterization of tissues response by tensile and stress relaxation tests and the evaluation of urethral structural behavior by inflation tests.

Several animals (including pig, dog, sheep and calf) were compared to find a suitable model for ex vivo characterization. Indeed, the experimental investigation on humans is complex and must take into account an extended group of subjects with similar age, body conformation and health conditions. At present, experimental testing on human urethrae is performed in vivo.

Stallion and carnivores own a musculocavernous penis, with larger septa in cavernous and spongy regions and a higher amount of muscular fibers, inducing some approximation in the comparison with human case. Between these last two groups, also considering the availability of samples, the horse was assumed to represent a suitable model for ex-vivo characterization. In general, any animal model is an uncertain correlation with humans about mechanical properties change due to age and health conditions (Wolfe et al., 1999; Cavalcanti et al., 2007; Clark et al., 1987).

The equine urethra can be considered similar to human in lumen, hysto-morphometric conformation and micturition functional process (Pozor and McDonnell, 2002; Arrighi et al., 2004). These reasons motivate the selection of horse urethra for the investigation of the biomechanical response of urethra under sphincteric contraction.

The following is a case study conducted by Natali et al. (2016b).

Fresh penises from fifteen male saddle horses were obtained from a local slaughterhouse. Two urethrae were addressed to the histological investigation, stored in formaldehyde for fixation. The other thirteen urethrae were divided to provide the specimens for the mechanical tests of urethral tissues and structures.

2.1 Histological analysis

The histological analysis aims at identifying tissues configuration, including the content of collagen or muscular fibers in the different layers. The analysis of histological samples allowed evaluating the structural components of the urethra and their

distribution. Urethral lumen shows a complex cross-sectional shape, ranging between slit- and star-like ones (Pullan et al., 1982; Dobrin et al., 1996).

Figure 5 reports a histological view of a transversal section of the most proximal urethra. The Masson trichrome staining makes it possible to identify the tissue conformation and the different layers (Figure 5a). A mucosa layer, surrounding the lumen of the urethra and the epithelium, was clearly identified as transitional epithelium (Figure 5b). Above the mucosa there is a layer of dense connective tissue showing collagen fibrils arrangement (Figure 5c). Above the dense connective tissue there was a loose tissue containing corpora spongiosa, blood vessels and smooth muscular fibers (Figure 5a).
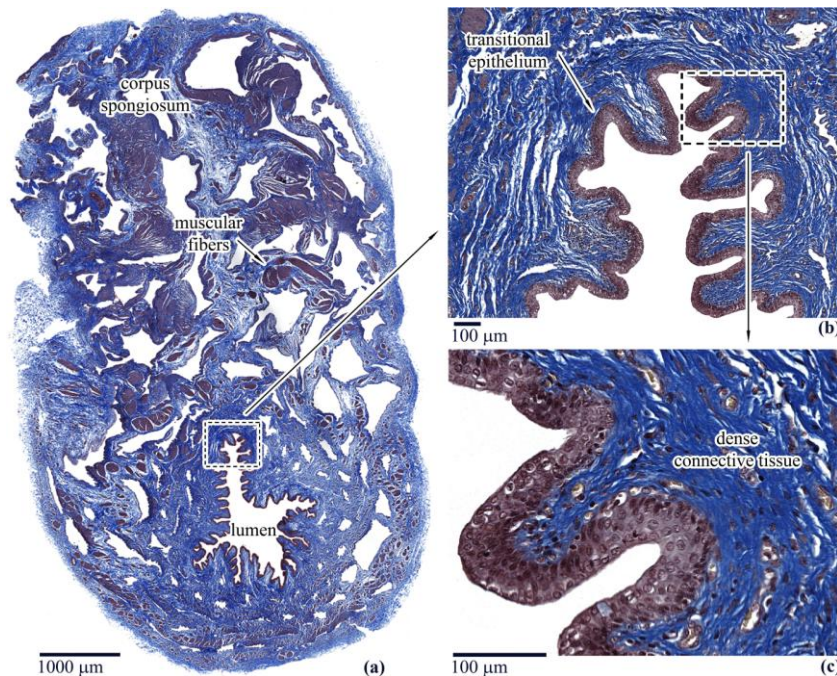
Figure 5 Trichrome histological section of the proximal urethra.

General view of the urethra transversal section (a) and details (b,c) to show the conformation of the epithelium and connective tissues surrounding the lumen. The section is taken at 50 mm from the most proximal end of the urethra.

The mechanical behavior was investigated by means of experimental tests of the urethral tissues (tensile and stress relaxation tests) and structure (inflation tests).

As concerning morphology, both in human and equine penis, a transitional epithelium and a thin layer of dense connective tissue surround the lumen. Above such layers, the urethra is composed of loose tissue containing corpora spongiosa, blood vessels and smooth muscular fibers.

Histological analysis on horse showed different micro- and macro-structural conformations of the urethral section when moving from the proximal to the distal region (Figure 6). The area of the section progressively decreases (Figure 6c). The area of the occluded lumen does not change significantly, while the lumen perimeter progressively increases (Figure 6d). The amount of collagen fibers is relevant along the overall urethra, with a marginal decrease in the proximal region (Figure 6b). The amount of muscular fibers decreases from proximal to distal urethra (Figure 6a).

The results of mechanical tests can be related to the urethral tissue microstructure evidenced by histological analysis. With particular regard to the proximal region of the urethra, the histology showed a preferential orientation of muscular fibers along longitudinal direction that may be regarded as the reason for tissue anisotropy.
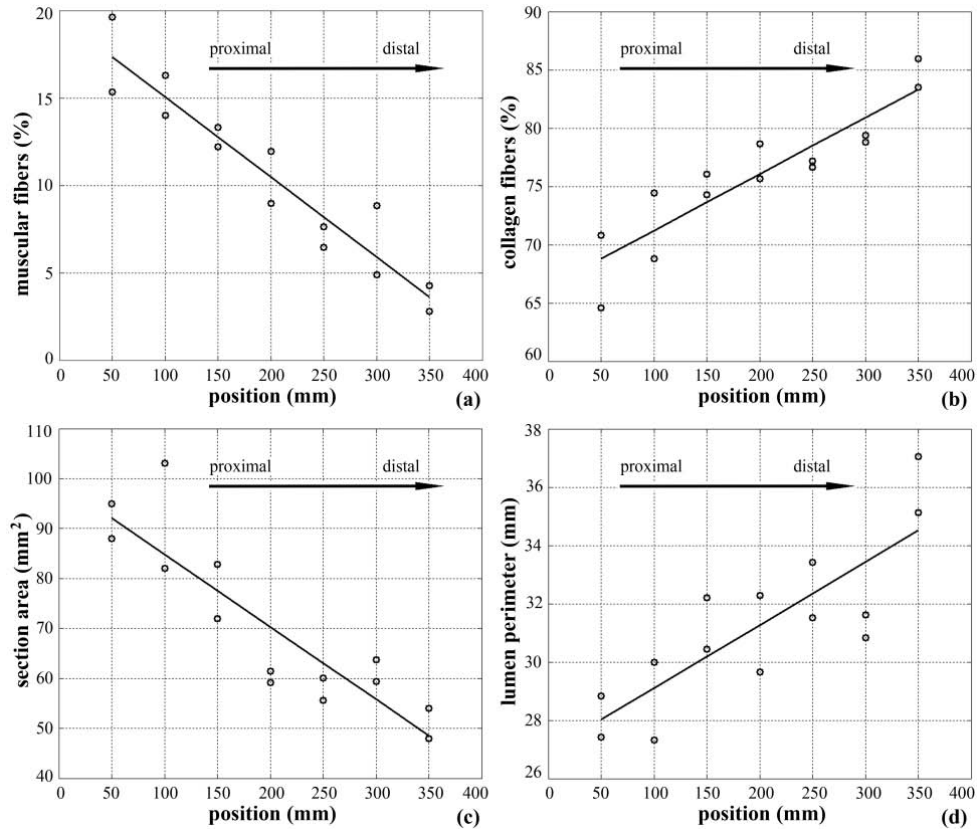
Figure 6 Quantitative analysis of urethra histology. Post-processing of histological images shows the almost linear correlation between muscular (a) and collagen (b) content and positioning. In addition, geometrical properties, as the urethra section area (c) and the lumen perimeter (d), show good linear correlation with position. The experimental data at 50 mm from the most proximal end correspond to the histological section shown in Figure 5. Measurement errors are ±5% of experimental values for muscular, collagen fibers and section area, ±0.5 mm for lumen perimeter and ±0.1 mm for position.

2.1 Mechanical tests

The most proximal and the most distal regions of each urethra were addressed to tensile and stress relaxation tests. The residual parts of the urethrae were almost equally divided into two segments to provide proximal and distal specimens for inflation tests. Each segment was longitudinally cut (Figure 7a) and straightened on a metal plate (Figure 7b). Rectangular specimens (with gauge-length of about 20 mm and width of about 5 mm) were dissected along longitudinal and circumferential directions (Figure 7c).
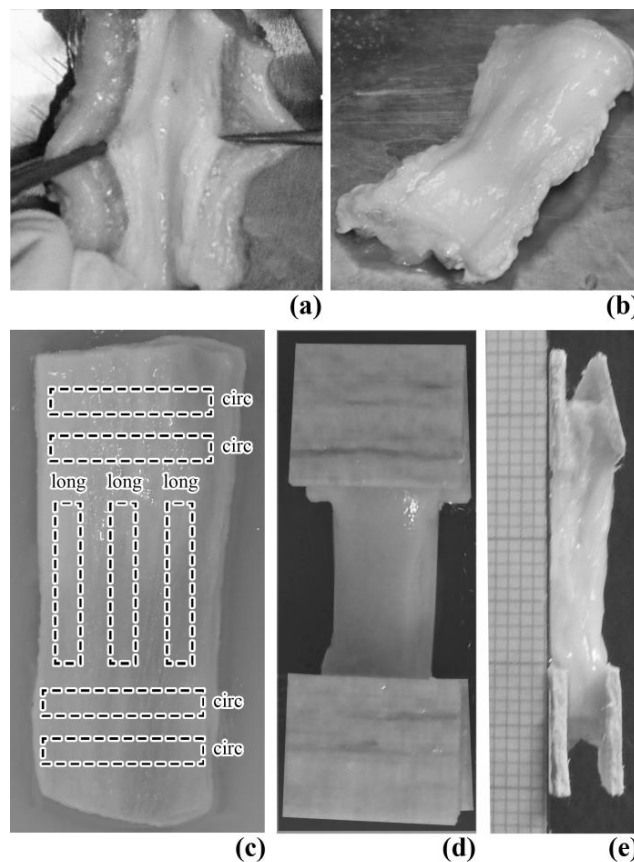
Figure 7 Samples preparation for mechanical tests of urethral tissues. The tubular segment is longitudinally cut (a) and straightened (b). Tissue specimens are dissected according to rectangular shape; two to four specimens are prepared along longitudinal and circumferential directions (d). Patches of balsa wood are glued to the sample ends to ease the specimen gripping: frontal (d) and lateral (e) views.

A Bose[®] ElectroForce[®] (Bose Corporation, ElectroForce Systems Group, Eden Prairie, MN, USA) machine was used to perform tensile tests (Figure 8). Each specimen was stretched up to 60 % strain and the strain was then kept constant for 300 s to investigate stress relaxation phenomena. Based on a preliminary evaluation of the tissue stiffness, a

load cell with capacity of 20 N with accuracy of ± 0.1 % was adopted. Preliminary tests were also performed to evaluate the influence of strain rate on viscous effects. The results showed that a 60 % s^{-1} strain rate minimizes the influence of viscous phenomena and prevents the dynamic effects that may develop when higher strain rates are adopted.

(a)

(b)
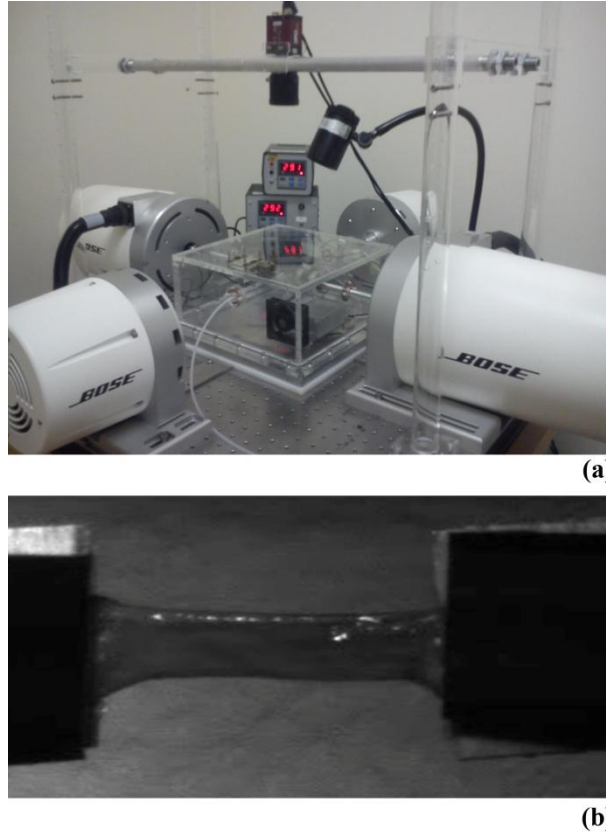
Figure 8 General experimental set-up (Bose® ElectroForce®) (a).
A tissue sample gripped to the experimental apparatus for uniaxial testing (b).

The strain was computed as the ratio between the current lengthening and the initial gauge length. The stress was calculated as the ratio between force measured by the load cell and the initial cross-sectional area of the specimen. The normalized stress is defined as the ratio of the stress at the current time and the peak stress at the beginning of the relaxation phase.

Exponential functions were adopted to interpret stress-strain and stress-time behavior and get preliminary information about elastic and viscous behavior of the tissue:

$$\sigma(\varepsilon) = \frac{k}{\alpha}\left[\exp(\alpha\varepsilon) - 1\right] \tag{1}$$

$$\sigma^{\text{norm}}(t) = (1 - \gamma_1 - \gamma_2) + \gamma_1 \exp\left(-\frac{t}{\tau_1}\right) + \gamma_2 \exp\left(-\frac{t}{\tau_2}\right) \tag{2}$$

Equation (1) aims at interpreting the nonlinear stress (σ) versus strain (ε) response of the tissue during loading. The parameter k specifies the tissue initial stiffness, while α is related to the non-linearity of the response due to stiffening. Equation (2) interprets the exponential decay of the normalized stress σ^{norm} with time t because of stress relaxation phenomena. The equation (2) accounts for two viscous branches. The number of viscous branches was defined to contemporarily minimize the number of parameters and correctly interpret the trend of experimental data.

According to the standard theory of visco-elasticity, the parameter $\gamma_\infty = 1 - \gamma_1 - \gamma_2$ identifies the ratio between the equilibrium stress (when relaxation phenomena are completed) and the peak stress (at the beginning of the relaxation phase). The parameters τ_1 and τ_2 are relaxation times. Data from tensile and stress relaxation tests developed on each specimen were fitted by Equations (1) and (2) respectively.

The effects of the imposed strain on the results from tensile tests were evaluated by means of a multivariate analysis of variance (ANOVA), considering three levels of strains: 10%, 20%, and 40% and comparing the mean stress values among different groups of samples (proximal longitudinal, proximal circumferential, distal longitudinal and distal circumferential samples).

The observation of muscular structures on subsequent transversal serial sections suggested the preferential alignment of muscular fibers along the urethra longitudinal direction. The orientation of muscular structures was confirmed by the histological analysis of longitudinal sections. The amount of smooth muscular fibers was greatly larger in the proximal region of the urethra than the distal portion.

Generally, the results of mechanical testing show that urethral tissue has a non-linear stiffening and time-dependent behavior, which is also anisotropic only in the proximal region. The statistical distribution of the experimental results are shown in the graphs of Figure 9, where median curves are reported together with the 50% probability scatter bands. Processing of the experimental curves from mechanical tests performed on the different samples led to a preliminary evaluation of elastic and viscous parameters.
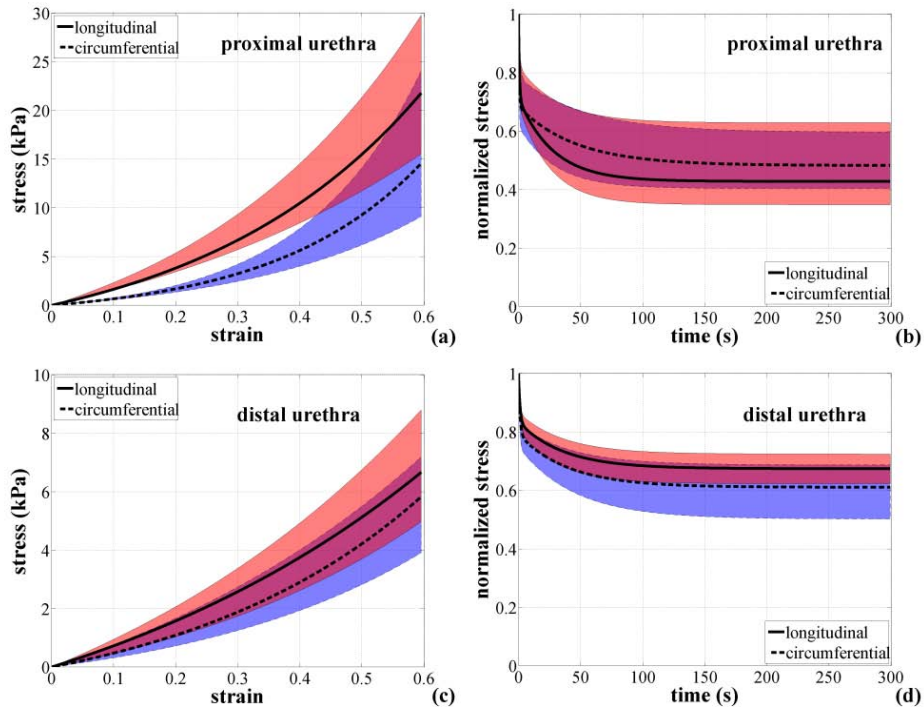
Figure 9 Results from mechanical tests of the urethral tissues. Tests were performed on specimens from proximal (a,b) and distal (c,d) regions of the urethra and accounting for constant strain rate (a,c) and stress relaxation (b,d) conditions. Data pertain to tests performed along both longitudinal (continuous lines and pink bands) and circumferential (dotted lines and blue bands) directions. Violet regions state the superposition of longitudinal and circumferential scatter bands.

The analysis of median curves made it possible to identify further sets of parameters (Table 1).

	k (kPa)	α	γ_1	γ_2	τ_1 (s)	τ_2 (s)
proximal region circumferential direction	5.41	4.22	0.33	0.18	0.74	52.72
proximal region longitudinal direction	14.41	2.75	0.32	0.26	1.07	37.02
distal region circumferential direction	4.46	2.32	0.23	0.17	1.46	51.13
distal region longitudinal direction	6.55	1.69	0.18	0.15	1.53	41.33

Table 1 Identification of tissue parameters by analysis of mechanical tests of the urethral tissues: elastic and viscous parameters from median curves.

2.2 Inflation tests

Mechanical tests of urethral structure were performed on tubular specimens taken from distal and proximal regions. Each sample was placed over a metal plate and straightened along the longitudinal direction.

The proximal extremity of the sample was fixed by means of a surgical elastic seam to a Teflon cannula with internal and external diameters of 4 and 6 mm, respectively. The other extremity was sealed to prevent any liquid leak (Figure 10a).

The inflation test was performed according to a two-step procedure. The first step was an almost instantaneous liquid in-flow, up to a prescribed inflated volume (Figure 10).
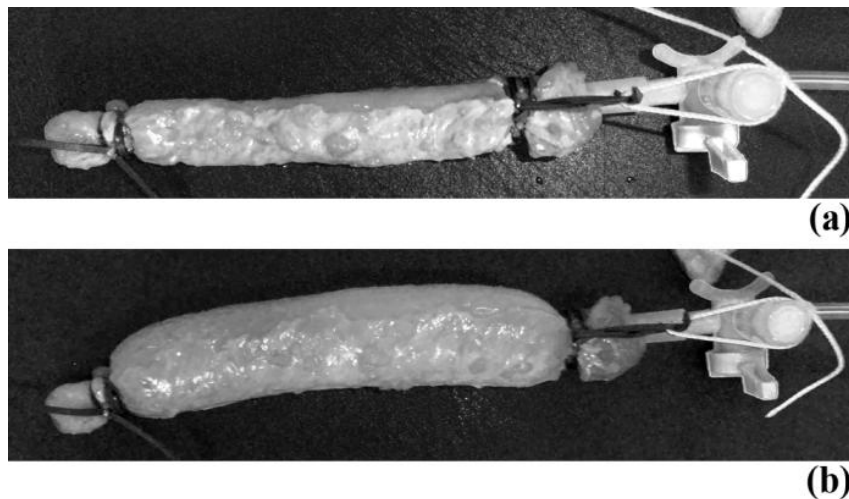
Figure 10 Samples preparation and mechanical testing at the structure level. The proximal end of the tubular sample is fixed by means of a surgical elastic seam to a Teflon cannula, coming from a syringe, while the other end is hermetically sealed. Not inflated (a) and inflated (b) conformations of a typical experimental sample.

Therefore, in this phase an elastic response of the structure may be assumed. In the second step, the volume of the sample was held constant for about 300 s to allow the development of visco-elastic processes, up to steady-state condition. Five to seven inflation tests were performed on each sample according to different inflated volumes, ranging between 5 and 50 ml. The inflation time was always lower than 0.1 s.

Exponential functions were adopted to interpret the behavior of pressure versus volumetric ratio and normalized pressure versus time to identify preliminary information about the structural elastic and viscous response of the tubular structure (Carniel et al., 2014a):

$$P(v) = \frac{K}{A}\left[\exp(Av) - 1\right] \qquad (3)$$

$$P^{\mathrm{norm}}(t) = (1 - \Gamma_1 - \Gamma_2) + \Gamma_1 \exp\left(-\frac{t}{T_1}\right) + \Gamma_2 \exp\left(-\frac{t}{T_2}\right) \qquad (4)$$

Equation (3) describes pressure (P) versus volumetric ratio (v) response of the tissue during the inflating step. The parameter K specifies the initial stiffness of the tubular segment, while A is related to the non-linearity of the mechanical response because of stiffening phenomena. Equation (4) describes the exponential decay of normalized pressure P^{norm} over time t because of visco-elastic phenomena. The parameter $\Gamma_\infty = 1 - \Gamma_1 - \Gamma_2$ identifies the ratio between the pressure when visco-elastic phenomena are completed and the peak pressure at the beginning, while T_1 and T_2 are parameters related to structural relaxation times. Data from tests developed on each specimen were fitted by Equations (3) and (4) respectively.

The fitting of the models to experimental data is obtained with the same procedure adopted for mechanical tests and the multivariate ANOVA was applied to data from inflation and relaxation tests, distinguishing samples into two groups (proximal and distal).

Experimental results on the urethral structure are reported in Figure 11 by means of median curves and 50% probability scatter bands.

Also in this case, it evident a nonlinear stiffening during inflating and time dependent phenomena in the following step.
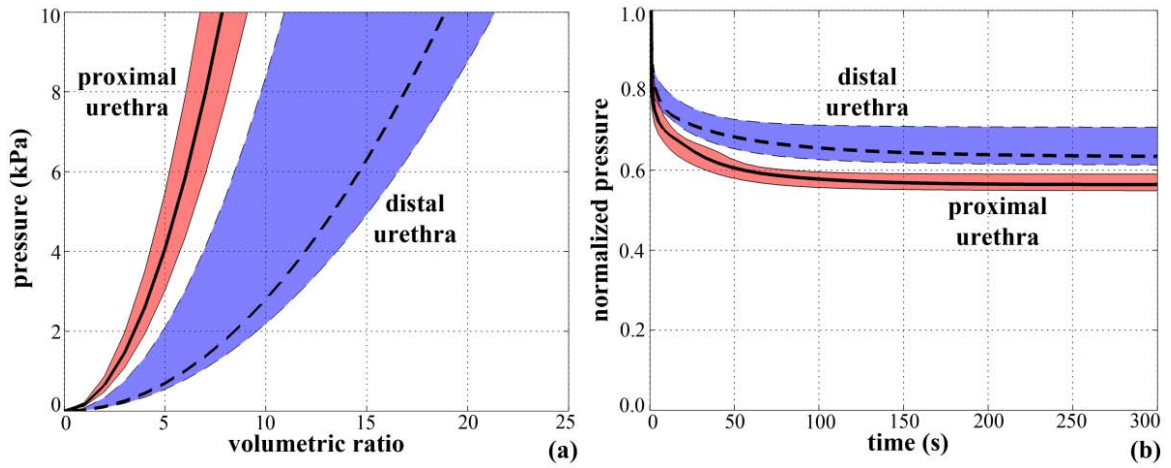
Figure 11 Results from mechanical tests performed at the structure level. Tests were performed on tubular specimens accounting for inflation (a) and stress drop (b) conditions. Median curves are reported together with 50% probability scatter bands. Data pertain to tests performed on samples from proximal (continuous lines and pink bands) and distal (dotted lines and blue bands) regions of the urethra.

Distributions of structural parameters were achieved by processing experimental data from the different samples and median curves (Table 2).

	K (kPa)	A	Γ_1	Γ_2	T_1 (s)	T_2 (s)
proximal region	1.92	0.18	0.25	0.18	0.42	24.05
distal region	0.33	0.18	0.20	0.16	0.72	29.94

Table 2 Identification of structural parameters by analysis of mechanical tests at structure level: structural elastic and viscous parameters from median curves.

The procedure may disrupt tissue continuity, with particular regard to collagen and muscular fibers, also modifying their rearrangement over time and viscoelastic phenomena. Probably for the same reason, the statistical analyses give different results when considering stress-relaxation tests and pressure-relaxation tests (proximal vs distal response).

The choice of the optimal number of viscous branches is based on the evaluation of the RSS (Residuals Sum of Squares, defined as $RSS = \sum_{i=1}^{n} \left(f_{exp,i} - f_{num,i} \right)^2$) for different numbers of viscous branches assumed. For experimental data on the relaxation of tissue samples, the fitting with two viscous branches gives an RSS value of the order of 10^{-2}.

Concerning the inflation results, the fitting with two viscous branches makes it possible to find a lower RSS value, of the order of 10^{-3}. Therefore, the choice of two viscous branches for the models is suitable for describing the viscoelastic response of tissue and structures. The evaluation of viscoelastic properties is extremely important for the description of the mechanical behavior of urethral tissues and structure. At present, in computational modeling for urinary incontinence research, urethral tissues have been frequently simplified as linear elastic materials.

For a more accurate mechanical evaluation, including an enhanced characterization of tissue anisotropy, biaxial tensile testing would be preferable, with load applied to a sample along two perpendicular axes, preferably corresponding to longitudinal and circumferential directions.

The compression behavior of urethra is also an aspect worth investigating.

CHAPTER 3

STRUCTURAL MODEL

The development of reliable computational models requires the thorough experimental characterization of the constituent tissues (Natali et al., 2009), through histological analysis and mechanical testing. Histological data processing allows for the definition of a virtual and a subsequent finite element model of a urethral section. The virtual solid model was defined through histological image processing and a specific hyperelastic formulation was developed to characterize the non-linear mechanical behavior. Constitutive parameters are preliminary identified by the inverse analysis of tensile tests on urethra tissue and then refined by numerical analysis of inflation tests on urethral duct (Gasser et al., 2006). To get closer to the real situation, in this work is presented an upgrade of the former two-dimensional model to a three-dimensional urethral duct model, evaluating the subsequent phases of micturition that determines the lumen opening and the occlusion by AUS.

The following analysis is conducted by Natali et al. (2016a).

Urethral lumen has a complex shape that assumes a variety of conformations as slit- and star-like profiles. The urethra is represented by three main regions, i.e. a pseudostratified columnar epithelium, a thin layer of dense connective tissue and a thick stratum of loose tissue including corpora spongiosa, connective septa and blood vessels (Pavlica et al., 2003). Specific image analysis routines are implemented in Matlab (The MathWorks Inc., Natick, MA, USA) aiming to geometrically characterize the conformation of urethra transversal section and to identify the different tissue layers.

A typical urethra section is assumed from a specific histological section, while geometrical dimensions are morphed considering average thickness values, as 0.06 mm, 0.14 mm and 5.13 mm for epithelium, dense connective tissue layer and loose tissue stratum, respectively.

The geometrical model of the urethral section is imported into the finite element preprocessing software Abaqus/CAE 6.14 (Dassault Systèmes Simulia Corp., Providence, RI).

3.1 2D-model

3.1.1 Finite element model definition

Six node triangular quadratic elements (CPS6 plane strain elements) and three node triangular linear elements (CPS3 plane strain elements) are adopted to mesh the dense connective tissue layer and the loose tissue stratum (Figure 12).
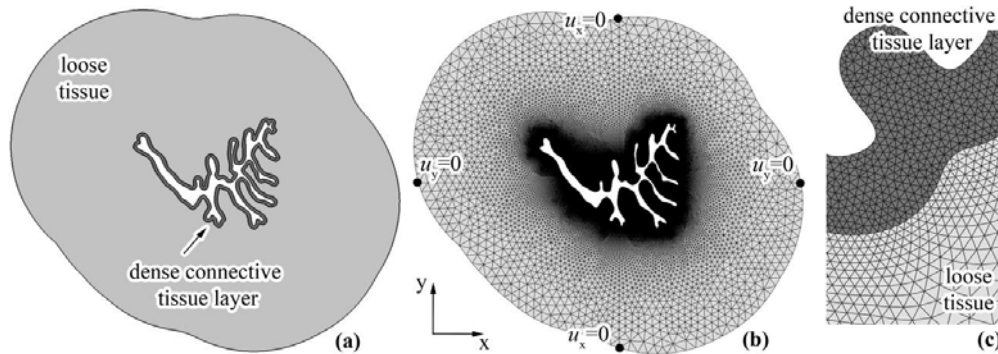
Figure 12 Urethra geometrical model (a); finite element model with boundary conditions for numerical analysis of structural inflation and lumen occlusion (b); detail of the finite element model showing the different discretization of loose and dense tissue layers (c).

Tie contact condition ensures the proper mechanical interaction at the interface between the two differently meshed regions for compatibility requirements. The mechanical contribution of the epithelial layer, due to its limited stiffness characteristics, is almost negligible. Anyway, it must be taken into account the interaction phenomena induced by compression loads, by means of a self-contact condition.

The typical nonlinear mechanical behavior of soft biological tissues suggests the assumption of an exponential pressure-overclosure relationship (Abaqus 6.14-1 Analysis User Manual, Dassault Systèmes Simulia Corp., Providence, RI).

Facing portions of lumen begin to interact and according to the results from experimental analysis on epithelial tissues, the contact pressure between lumen surfaces increase exponentially as the clearance continues to diminish; in detail, when clearance approaches zero, pressure is getting to 10 kPa (Raub et al., 2010; Chen et al., 2015).

Contact frictional properties ensure the transmission of shear loads between lumen surfaces, usually fully hydrated, with a 0.02 friction coefficient (Prinz et al., 2007).

Models are developed assuming incremental mesh refinement, defined through the

procedures of computational mechanics. To evaluate the influence of mesh conformation, numerical analyses simulating inflation tests are performed comparing the different models results.

In the final configuration of the model, mean element size within the dense connective tissue layer is 0.03 mm, while it ranges between 0.03 and 0.3 mm in the loose tissue stratum.

The model is composed by 31553 nodes (18142 and 13411 nodes, respectively, in dense connective layer and loose stratum) and 33695 elements (8034 and 25661 elements, respectively, in dense connective layer and loose stratum).

3.1.2 Constitutive analysis

The mechanical behavior of dense connective and loose tissue is defined by a specific hyperelastic formulation that proved its capability to interpret the typical features of soft tissue mechanics in previous investigations (Natali et al., 2009; Natali et al., 2010; Carniel et al., 2014).

The stress-strain relationship:

$$\mathbf{P} = -p\mathbf{F}^{-T} + C_1 \exp\left[\alpha_1\left(I_1 - 3\right)\right]\left(2\mathbf{F} - 2/3\,I_1\mathbf{F}^{-T}\right) \tag{1}$$

where $\mathbf{P}$ is the first Piola-Kirchhoff stress tensor, as a measure of nominal stress, $\mathbf{F}$ is the deformation gradient, p is a Lagrange multiplier that specifies hydrostatic pressure and ensures the incompressibility of the material, I_1 is the first invariant of the right Cauchy-Green strain tensor $\mathbf{C} = \mathbf{F}^T\mathbf{F}$. The constitutive parameter C_1 is related to tissue shear stiffness in the unstrained configuration, while the non-linearity parameter α_1 specifies tissue stiffening with stretch.

Constitutive parameters are identified by the inverse analysis of tensile tests performed on horse urethra (Natali et al., 2016b).

From the general model (Equation 1), in the case of uni-axial tensile loading, according to the specific boundary conditions, the following relationships between stress and stretch components are computed:

$$P_{cc} = 2C_1 \exp\left[\alpha_1\left(\lambda_c^{\,2} + 2\lambda_c^{\,-1} - 3\right)\right]\left(\lambda_c - \lambda_c^{\,-2}\right) \tag{2}$$

where λ_c and P_{cc} are stretch and nominal stress, respectively, along circumferential direction.

Different sets of parameters are identified analyzing the statistical distribution of experimental results, as median, 25th and 75th percentiles. With regard to experimental results, stretch is computed as the ratio between the gauge-length of the tissue specimen in deformed and undeformed configurations, nominal stress is evaluated as the ratio between tensile force and specimen mean cross-section area in the undeformed configuration.

The minimization of discrepancy between experimental data and model results (Natali et al., 2009) lead to the following parameters: C_1 = 1.09 [0.95, 1.37] kPa, α_1 = 1.26 [1.07, 1.40]. Such parameters describe the mechanical behavior of a homogenized urethral structure. Nevertheless, the multi-layered configuration leads to a non-homogeneous stress and strain distribution.

Figure 13 shows a tensile test on a circumferential urethra sample, replicated by computational modeling. Finite element analysis investigates all the different steps of the experimental procedure, including urethra ring opening for the preparation of the sample (Figure 13b), straightening as during sample gripping (Figure 13c) and tissues stretching through tensile testing (Figure 13d).
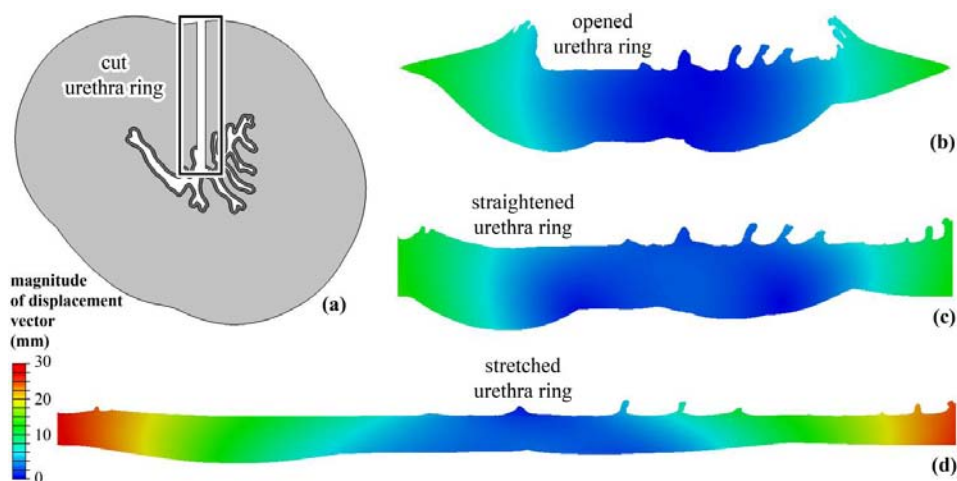
Figure 13 Tensile tests on urethra samples. Mimicking the experimental procedure, the finite element model of the cut urethra samples (a) undergoes the opening (b) and straightening (c) up to large tensile stretching (d).

Different sets of parameters must be identified for the different tissues.

To overcome the problem of the separation of different tissue that could induce relevant damage, the interpretation of stiffness characteristics is performed by the support of numerical model simulation. This consideration can be referred to the coupling of dense and loose tissue with regard to the evaluation of the parameters C_1 and α_1. A numerical analysis of tensile tests is developed considering different values of a multiplier k, ranging between 1 and 1000 (Figure 14), that represent the ratio of C_1 values attributed to the different components. The large range of k values makes it possible to evaluate a complete set of conformations of urethra tissues: $k=1$ specifies a homogenous structure, while $k=1000$ describe a thin and highly stiff layer surrounded by a thick and tenuous stratum.
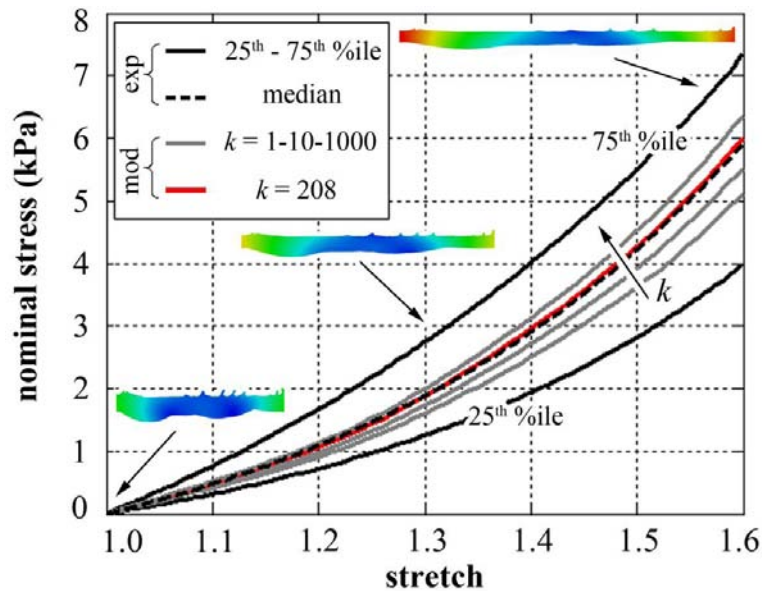
Figure 14 Comparison of experimental and computational results from tensile tests on urethra circumferential samples. Median, 25th and 75th percentiles experimental curves are reported. Computational results are defined depending on different sets of constitutive parameters according to the values of multiplier k.

Additional investigations are developed with regard to experimental results from inflation tests. A homogeneous hydrostatic pressure field is applied to the intraluminal border of the urethra model. Pressure value is progressively increased to simulate the experimental progressive inflation.

Null displacement conditions are imposed on four diametrically opposite nodes along single directions, on the outer boundary of the model (Figure 12b), in order to provide minimal constraints and to satisfactorily interpret the actual constraint of the sample

during experimental testing. Different analyses are performed considering the different values of the multiplier k (Figure 15).
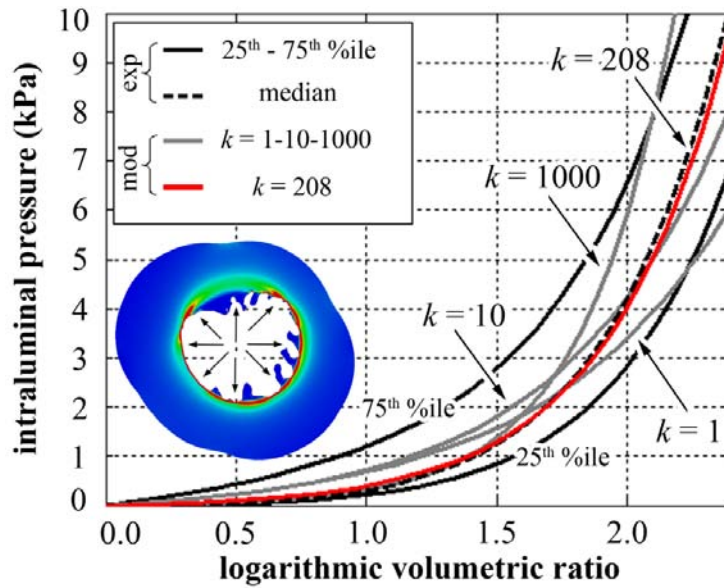
Figure 15 Comparison of experimental and computational results from inflation tests on urethra tubular samples. Median, 25th and 75th percentiles experimental curves are reported. Computational results are defined depending on different sets of constitutive parameters according to the values of multiplier k. The logarithmic volumetric ratio is defined as the logarithm of the ratio between the volume of the urethra lumen, when mechanical action is applied and the final volume of the lumen.

The multiplier value k=208 entails the minimal overall discrepancy between computational and experimental median results. Parameters $C_1 = 34.89$ kPa, $\alpha_1 = 1.26$, and $C_1 = 0.17$ kPa, $\alpha_1 = 1.26$ are finally assumed to specify the median behavior of dense connective tissue layer and loose tissue stratum, respectively.

While the specific value of k modestly influences the tensile behavior of the urethra samples (Figure 14), the effect on the inflation tests shows different trends and larger intensity variation (Figure 15). Low k values entail an almost homogenous distribution of stiffness along the urethra thickness. On the contrary, high values of k better describe the configuration of the urethra, as an inner thin and stiff layer surrounded by a thick and compliant stratum. The trend of intraluminal pressure with lumen volume significantly varies with the multiplier k, in accordance with the stiffness contribution of the dense connective tissue layer that progressively increases with the distension of the lumen.

3.1.3 Numerical analysis

With the aim to mimic the action of artificial sphincters, a homogeneous pressure field is applied all around the external boundary of the urethral model.

Numerical analyses are performed by a two steps procedure. During the first step, the urethra is progressively inflated up to the intraluminal pressure target that ranges between 0 and 10 kPa. During the second step, the occluding pressure is increased up to 10 kPa, according to the configuration of commercial devices (Griffiths, 1971; Aagaard et al., 2012).

The tissues mechanical functionality is evaluated by the numerical analysis of inflation tests. Figures 16 and 17 show the contours of radial displacement and stress fields, respectively, for different values of intraluminal pressure.
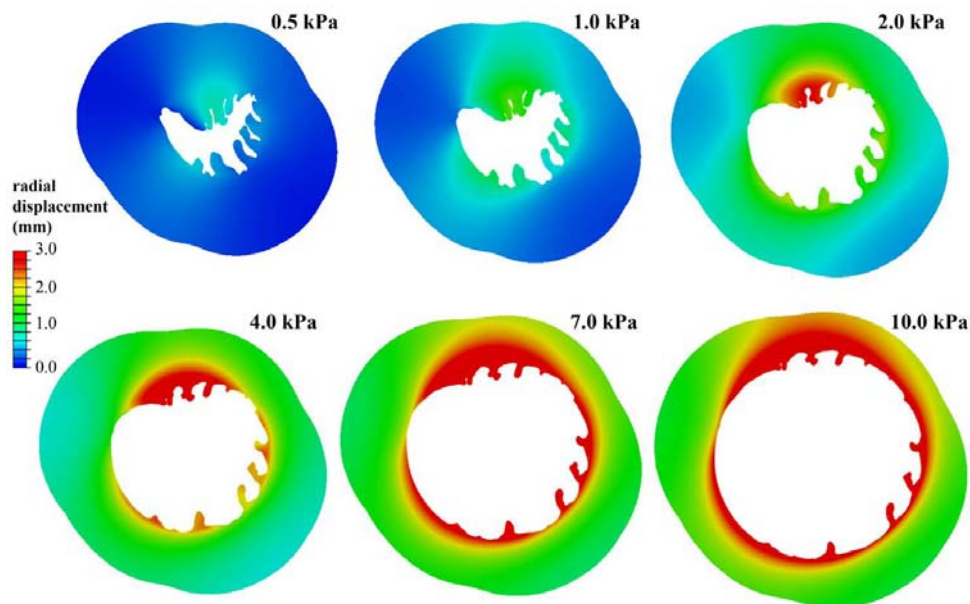
Figure 16 Numerical analysis of structural inflation tests. Contours of radial displacement field at different intraluminal pressure conditions.
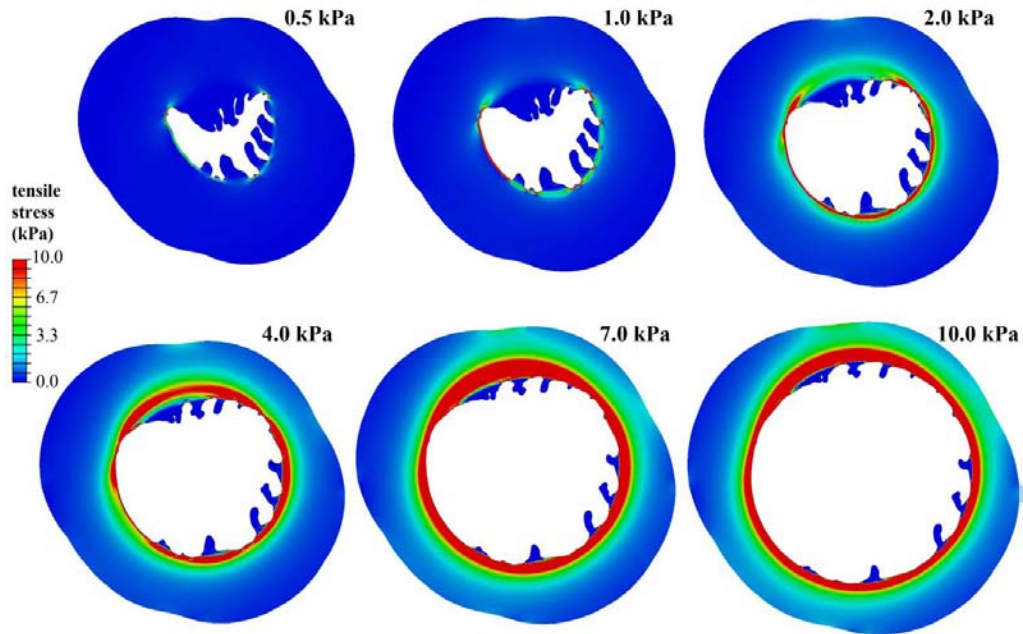
Figure 17 Numerical analysis of structural inflation tests. Contours of tensile stress field, as the maximum principal value of the Cauchy stress tensor, at different intraluminal pressure conditions.

In Figure 17 is reported the stress distribution for different values of intraluminal pressure depending on urine flow.

Figure 18 shows results from numerical analyses that took into account the combination of different values of intraluminal and external occluding pressures. The different curves specify the structural behavior of the urethra, as the trend of occluding pressure with lumen volume variation. Each curve pertains to a specific value of the intraluminal pressure under different compression up to occlusion and subsequent compression induced. The data are reported with regard to the volume variation depending on the load induced.
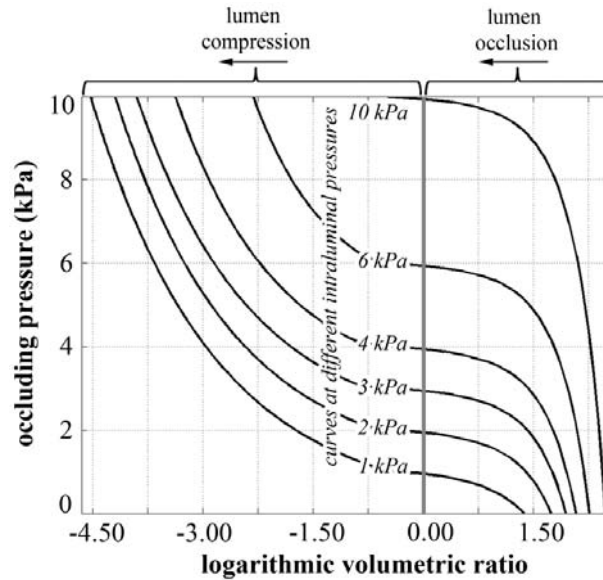
Figure 18 Results from numerical analysis of lumen occlusion. Each curve describes the structural behavior of the urethra at a specific value of intraluminal pressure and for increasing occluding pressure conditions.

Occlusion occurs when external and intraluminal pressures almost equalize and subsequently urethral epithelial tissues undergo compression phenomena. Occluding actions determine substantial compressive strains within dense connective tissue and loose tissue.

Figure 19 shows how tissue behaves during occlusion. The compressive strain field is reported for both loose tissue and dense connective tissue layer for different values of the occluding pressure conditions, while intraluminal pressure is 1 kPa.
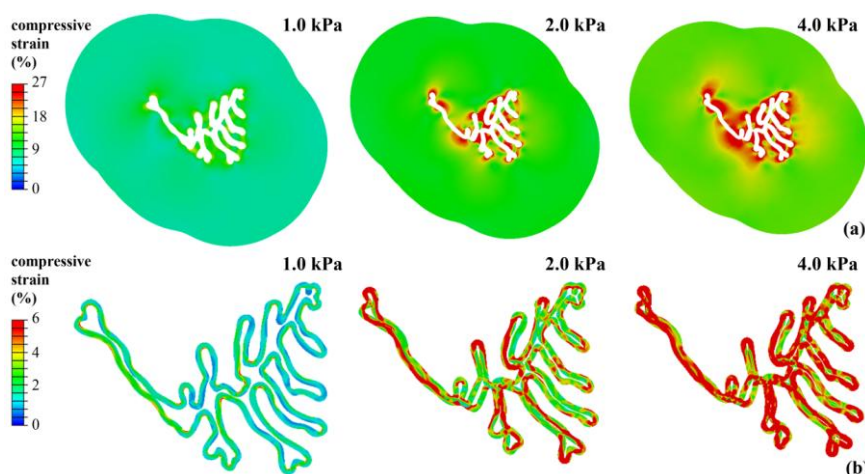
Figure 19 Numerical analysis of lumen occlusion. Contours of compressive strain field, as the minimum principal value of the logarithmic strain tensor, into loose tissue (a) and dense connective layer (b), assuming an intraluminal pressure of 1 kPa.

3.2 3D-models

Considering the 2D-model, an agile computational procedure is conducted analyzing 3D-models of urethral duct with length of 0.3 mm and 3 mm, said Model A and Model B respectively.

The procedures to realize these 3D-models are similar to those 2D-models. In Model A the lumen volume is calculated with the support of Matlab (The MathWorks Inc., Natick, MA, USA). It is also achieved Model B to verify that the Matlab subroutine worked also with multiple nodes along the thickness.

In these models is investigated the relationship between lumen volume and external pressure. Because of their scarce thickness, the results obtained by these models are similar to those with 2D analysis. To obtain a more realistic configuration of the urethral duct and a representation of the phases of the urethral occlusion through artificial sphincters, models with lengths of 10 mm and 20 mm are considered, said Model C and Model D respectively.

Different lengths of the tract and conformations of the cuff are regarded, mimicking different loading conditions in terms of force intensity, distribution and consequent deformation caused in soft tissues. The action induced in the healthy urethra is investigated, as basis for an evaluation of the efficacy and reliability of the sphincter devices.

3.2.1 Finite element model definition

Considering the small tract of urethral duct under investigation, the structure and the dimensions of the cross section are taken as to be uniform along the length of the model. Boundary conditions along specific transversal directions are imposed on the outer surface, in order to provide minimal constraints and to interpret the mechanical environment of the urethral duct after AUS placement. Null displacement conditions are expected at the midpoint of the pressure field on the transversal section.

The general settings of a model definition, used for all configurations, are here reported. To mesh the dense connective tissue layer and the loose tissue stratum eight node hexahedral elements with reduced integration are adopted. The enhanced hourglass control formulation is adopted to consistently prevent mesh instability.

The mechanical behavior of dense and loose tissues is described by a hyperelastic constitutive formulation, considering different parameters for the different layers. The adopted strain energy function is reported below:

$$W(\mathbf{C}) = -p(J-1) + C_1\left\{\exp\left[\alpha_1(I_1-3)\right]-1\right\} \tag{1}$$

where $\mathbf{C}$ is the right Cauchy-Green strain tensor, J is the deformation Jacobian, as $J = \sqrt{\det(\mathbf{C})}$, I_1 is the first invariant of C, as $I_1 = \text{tr}(\mathbf{C})$, while p is a Lagrange multiplier that specifies hydrostatic pressure and ensures the incompressibility of the material. The parameter C_1 is related to tissue shear stiffness in the unstrained configuration, while the non-linearity parameter α_1 specifies tissue stiffening with stretch. Parameters identification is performed by analyzing experimental results, as reported by Natali et al. (2016a), and leads to the following values: $C_1 = 5.13\,\text{kPa}$, $\alpha_1 = 1.26$ and $C_1 = 0.17\,\text{kPa}$, $\alpha_1 = 1.26$ for dense and loose tissues, respectively.

The local interaction response on the facing portions of lumen surfaces must be associated with a self-contact condition strategy. The tissues mechanical behavior entails the assumption of an exponential pressure-overclosure relationship. The contact pressure increases exponentially up to 10 kPa. Contact frictional properties ensure the transmission of shear actions between lumen surfaces and it is assumed as 0.02 (Prinz et al., 2007).

Incremental mesh refinement technique is adopted between 0.04 and 0.4; result sensitivity is associated with the size of elements.

3.2.2 Numerical analysis

General settings are also used for numerical analysis that is here reported.
Numerical analyses are performed by a two steps procedure. During the first step, the urethra is progressive inflated up to the target intraluminal pressure. During the second step, the occluding pressure is increased up to 10 kPa.
The sphincter pressure field determines lumen occlusion. During the process, large deformation phenomena develop and complex contact interactions occur between different portions of the lumen surface. Despite lumen occlusion can be approximated

as a quasi-static process, an efficient numerical interpretation of the problem can be achieved by adopting explicit solution algorithms (Abaqus Explicit 6.14-1, Dassault Systèmes Simulia Corp., Providence, RI). The explicit solution method is a true dynamic procedure that is based upon the implementation of an explicit integration algorithm. The equations of motion for the body are integrated using the explicit central-difference integration scheme that is conditionally stable, in direct proportion to element dimension and material density and inversely to material stiffness. The specific configuration of the developed computational model leads to extremely small stable time increments, as low as 10^{-8} s, causing the high computational effort in solving the corresponding quasi-static occlusion process, which requires a time period ranging between 0.1 and 1 s. Elements of the dense connective tissue layers determine the small value of the time increment, because of their small size and relatively high stiffness. Aiming at reducing the computational effort, mass scaling technique can be adopted. Considering the small thickness of the dense connective tissue layer, mass scaling of such layer does not significantly modify the mass of the system and, consequently, does not introduce relevant fictitious inertial contributions. Semi-automatic mass scaling procedure was adopted, setting the stable increment time at 10^{-6} s. Both nodal accelerations and model total kinetic energy have been monitored during the analysis.

3.2.3 Model A

Model A is realized to investigate the behavior of the 3D minimal model, starting from 2D model. In this regard 3D elements are used to create an extrusion from 2D model. Considering the configuration lengths 0.3 mm, the model is composed by 36400 nodes (6892 and 31084 nodes, respectively, in dense connective layer and loose stratum and 1576 nodes in common) and 17755 element (2653 and 15102 elements, respectively, in dense connective layer and loose stratum). Along longitudinal direction is set 1 element 0.3 mm long (Figure 20).
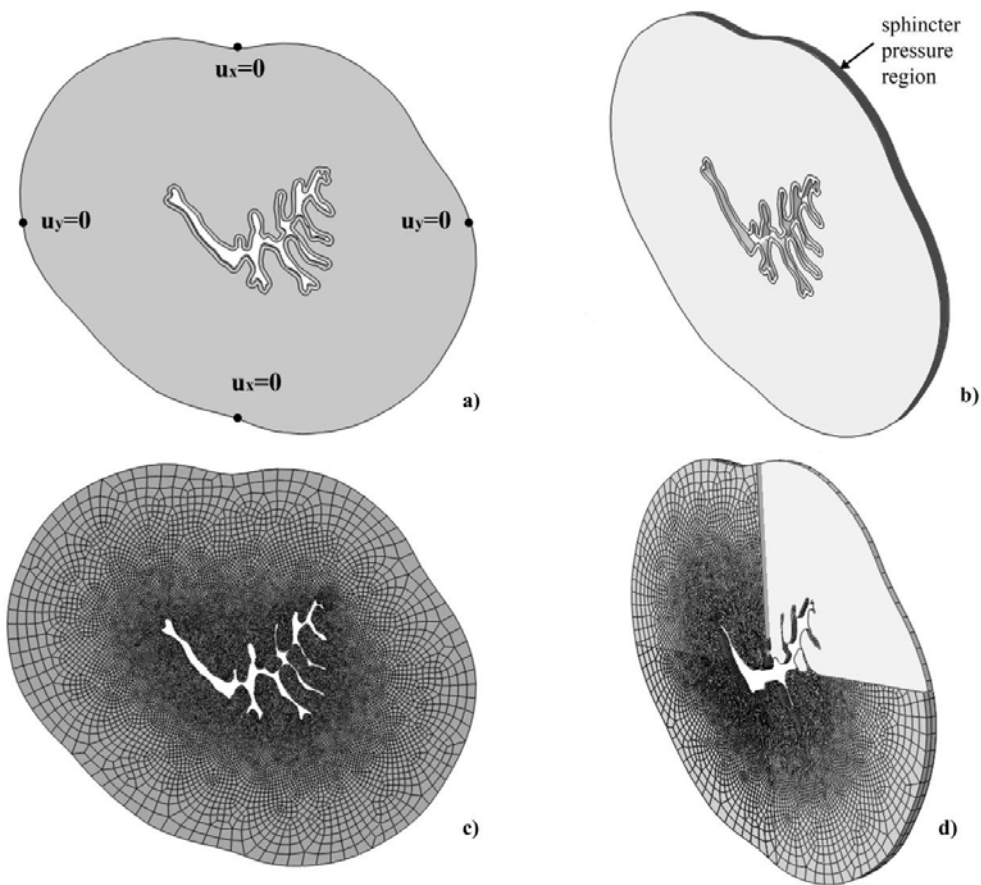
Figure 20 Model of the urethral duct. Geometrical model of the urethra transversal section (a). Three dimensional solid model of the urethral duct showing the assumed boundary (a) and loading (b) conditions. Finite element discretization: transversal section (c); three dimensional representation of urethral duct with spongy region and dense connective tissue layer (d).

To compare with the 2D-model, a configuration is realized without external pressure and with internal pressure that assumes the following values: 0.1 kPa, 1 kPa and 10 kPa (Figure 21).
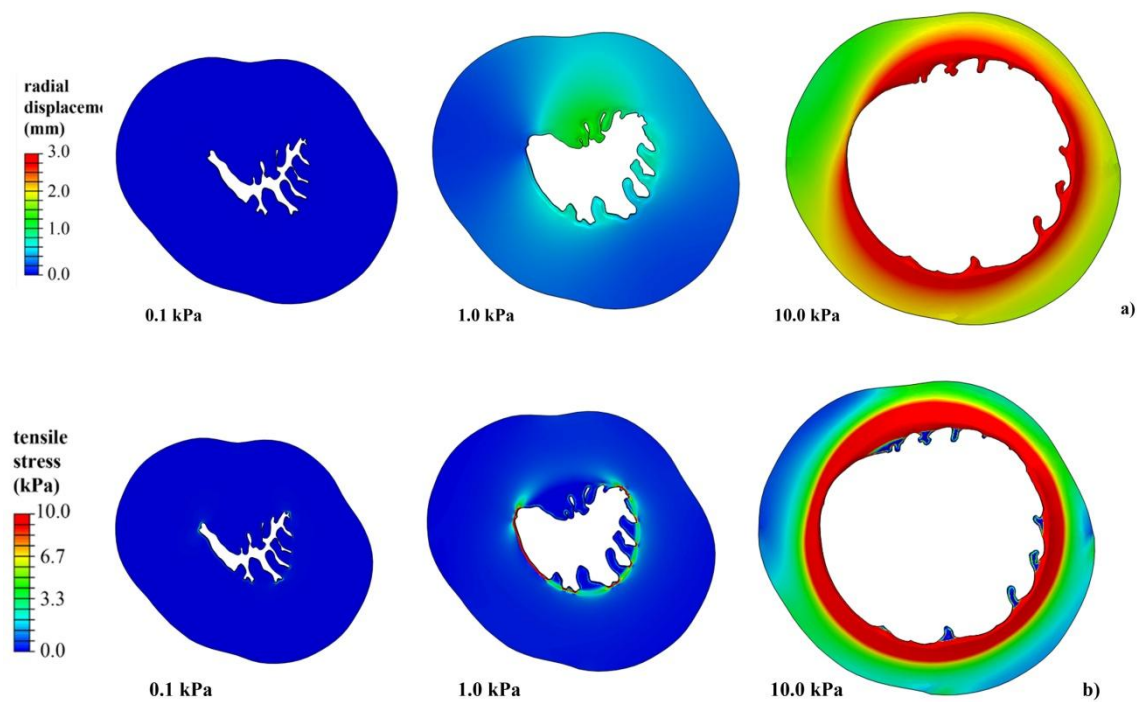
Figure 21 Numerical analysis of structural inflation tests. Contours of radial displacement field (a) and contours of tensile stress field, as the maximum principal value of the Cauchy stress tensor (b), at different intraluminal pressure conditions.

The model is too thin to appreciate the 3D conformation and the results obtained does not show a consistent difference in 2D model.

Moreover, another configuration is realized with the same configuration of the model.

Pressure field is distributed uniformly and symmetrically along the length of the urethral duct; the external pressure values 10 kPa while intraluminal pressure is realized with fluid cavity and takes the following values: 0.1 kPa and 1 kPa.

So, during the inflation test simulation, the urethra is progressively inflated up to 0.1 kPa or 1 kPa and then the occlusion pressure is increased up to 10 kPa (Figures 22 and 23).
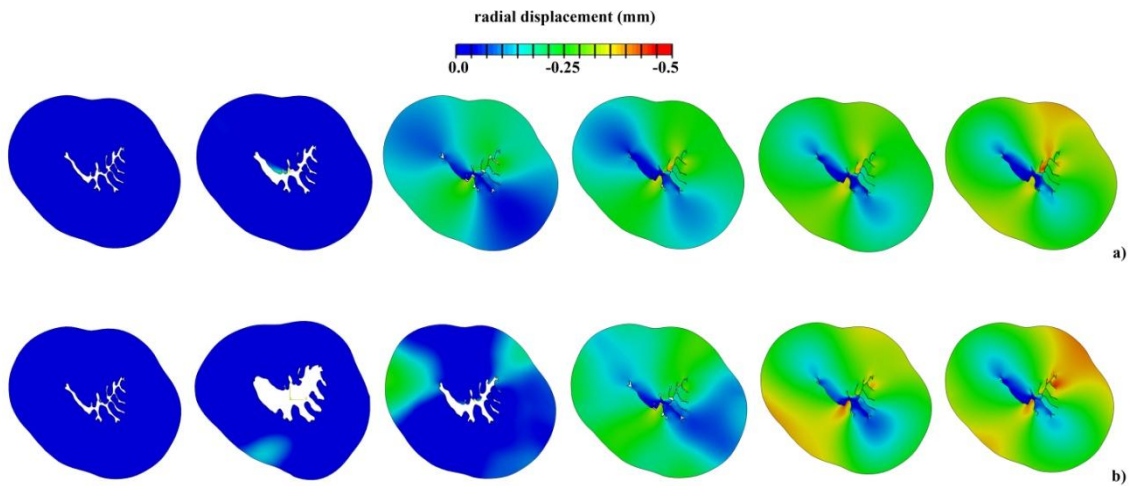
Figure 22 Contours of radial displacement field at intraluminal pressure of 0.1 kPa a)
and of 1 kPa b).
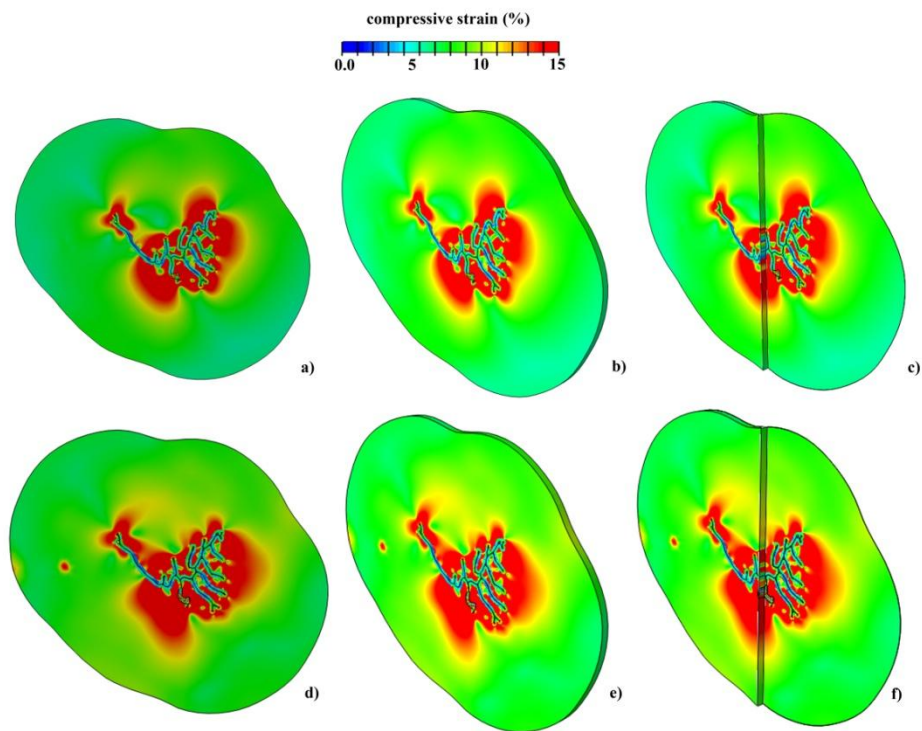
Figure 23 Contours of compressive strain field, as the minimum principal value of the logarithmic strain tensor at intraluminal pressure of 0.1 kPa a), b), c) and of 1 kPa d), e), f).

The internal pressure is imposed from the start of the analysis, with values of 0.1 kPa or 1 kPa while the external pressure is set to 0.05 s with values of 10 kPa. Thus in the first phase, the duct opens until it reaches the maximum opening at 0.05 s and then occludes till the complete closing. The development of the volume and the relationship between

volume and external pressure are considered.

Considering different values of internal pressure, in the inflation phase, when the duct is getting larger, the volume increases up to 1.2 mm^3 and 6.3 mm^3 in case of internal pressure of 0.1 kPa and 1 kPa respectively and then, in the occlusion phase, the volume decrease down to zero (Figure 24).
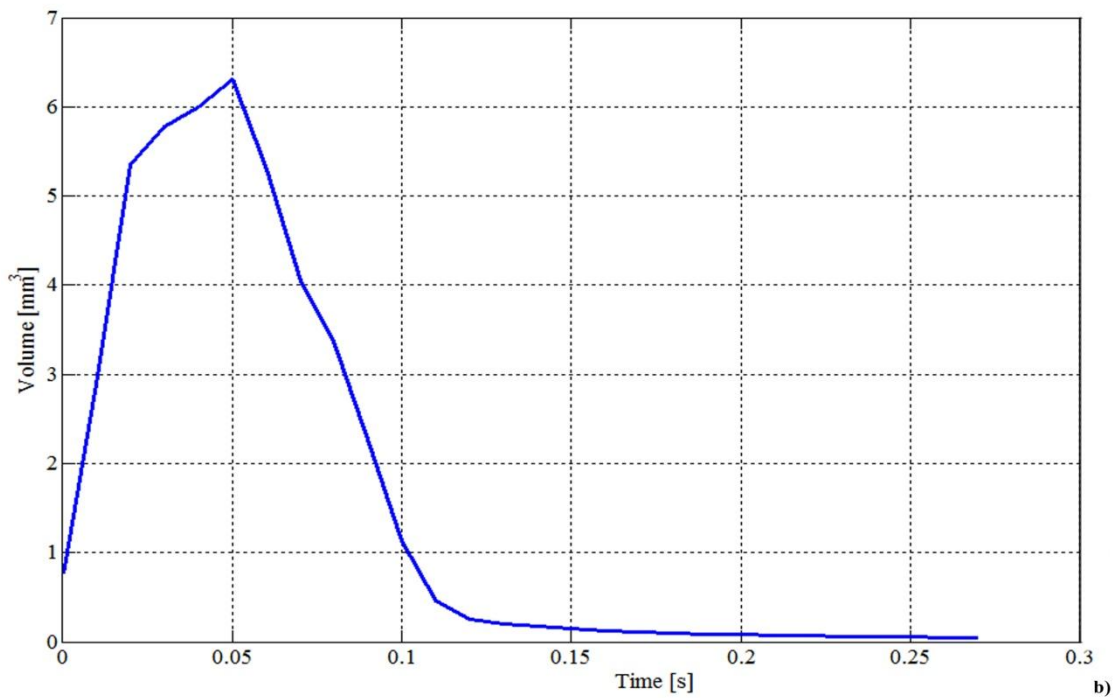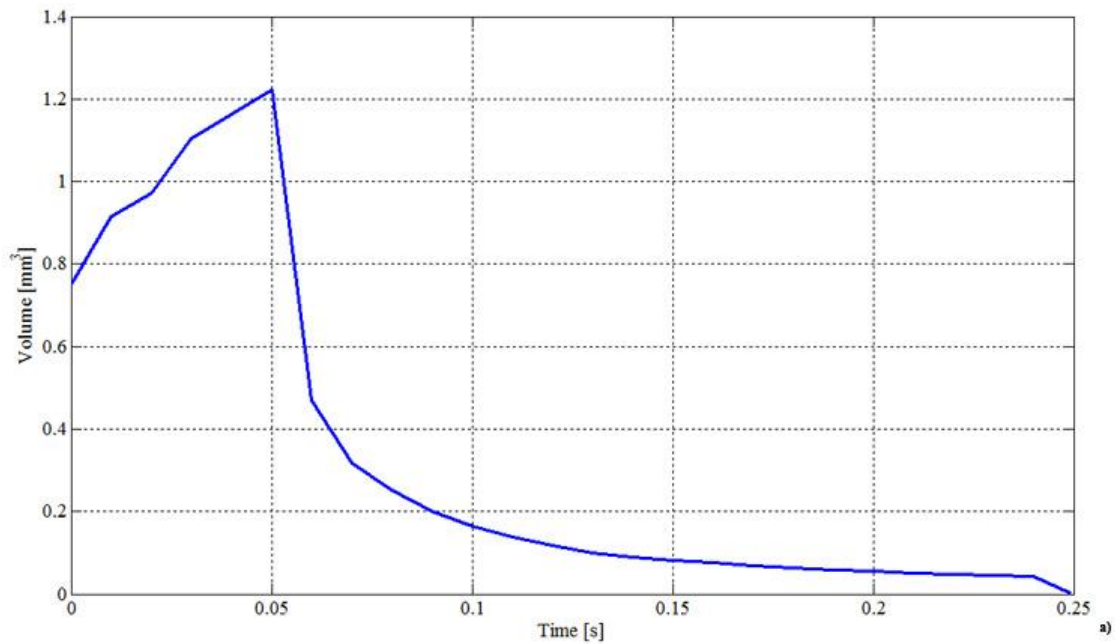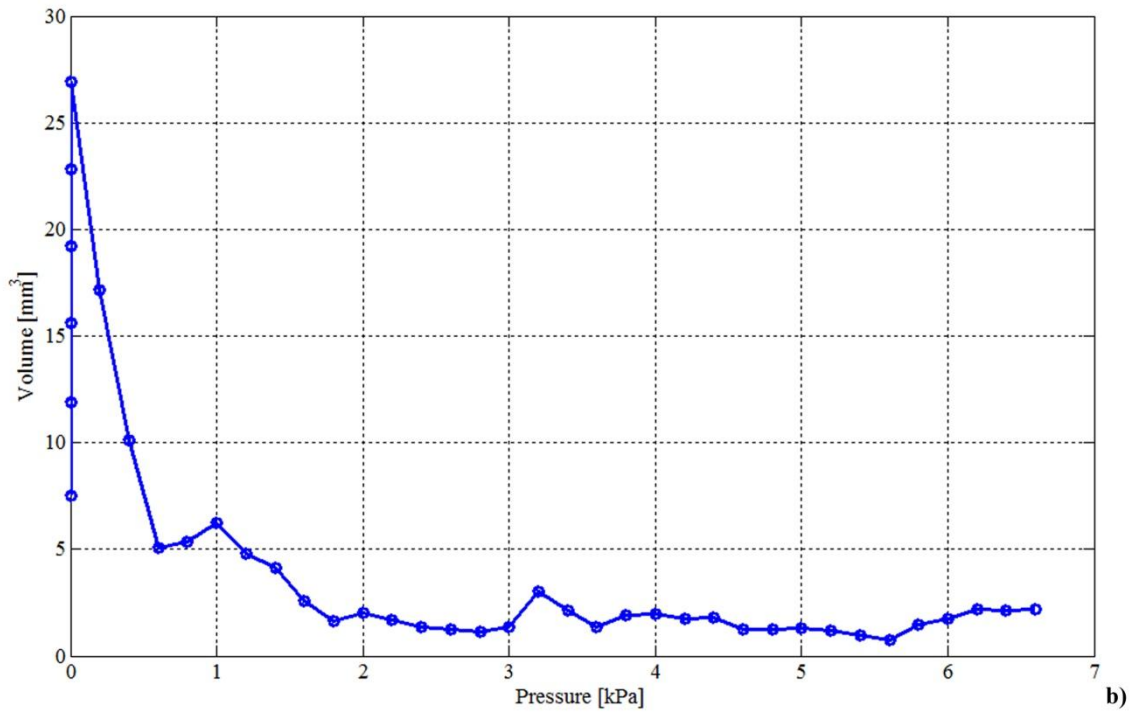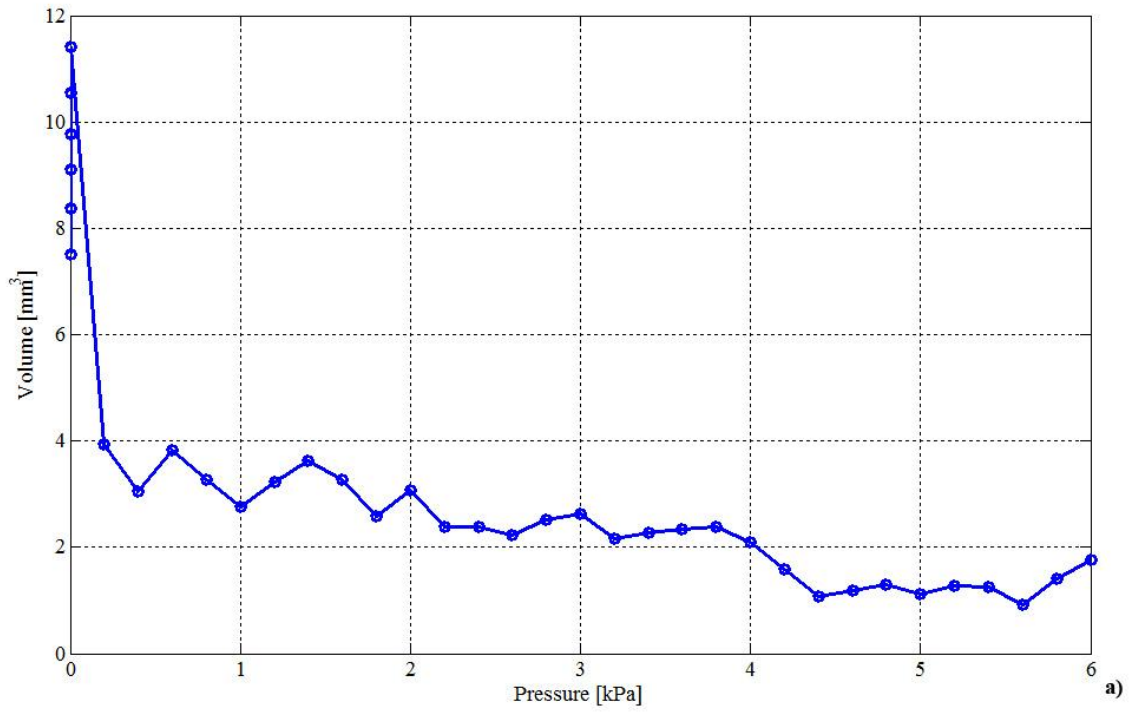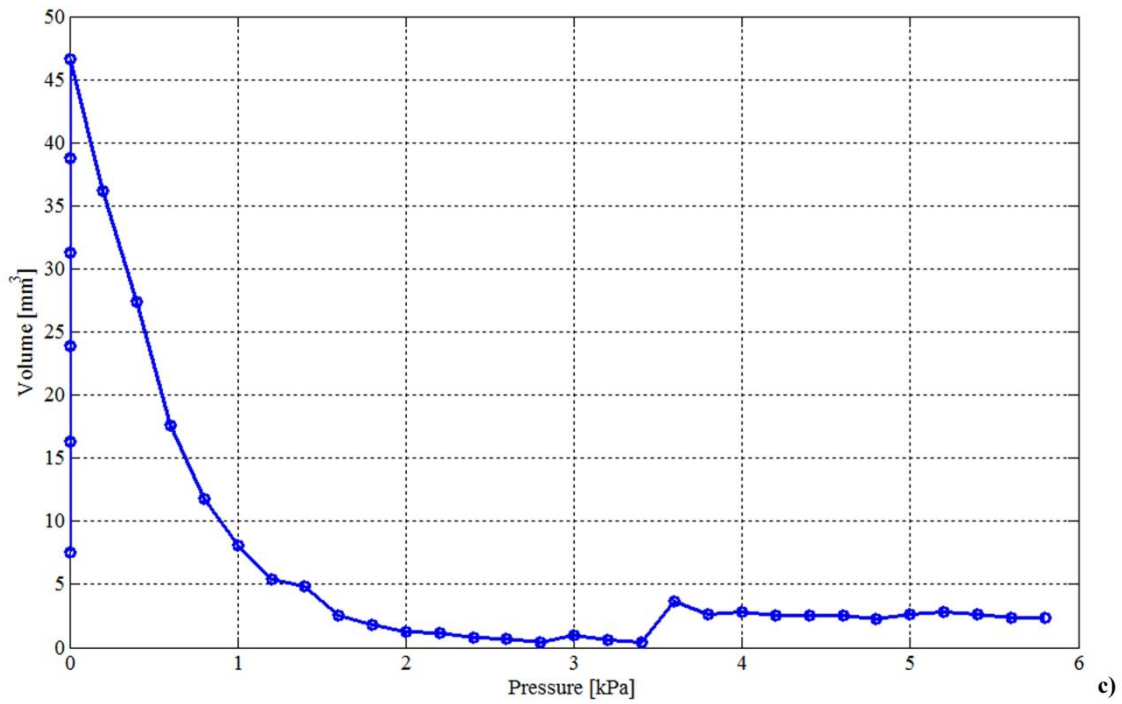

Figure 24 Graphic volume-time. Intraluminal pressure values 0.1 kPa in (a) and 1 kPa in (b).

The volume is calculated with a specific routine implemented in Matlab (The MathWorks Inc., Natick, MA, USA). The Matlab program calculates the volume in the various time instants. Starting from the coordinates of the nodes, is calculated the area of every sections created with mesh action. Computed all areas, the volume is calculated using the formula of the pyramid trunk.

The external pressure occludes more slowly the structure with a greater internal pressure. In fact, in the first case there is an immediate occlusion while in second one the occlusion is slower, as shown in Figure 24.

The relationships between volume and external pressure for different values of intraluminal pressure are reported in Figure 25.
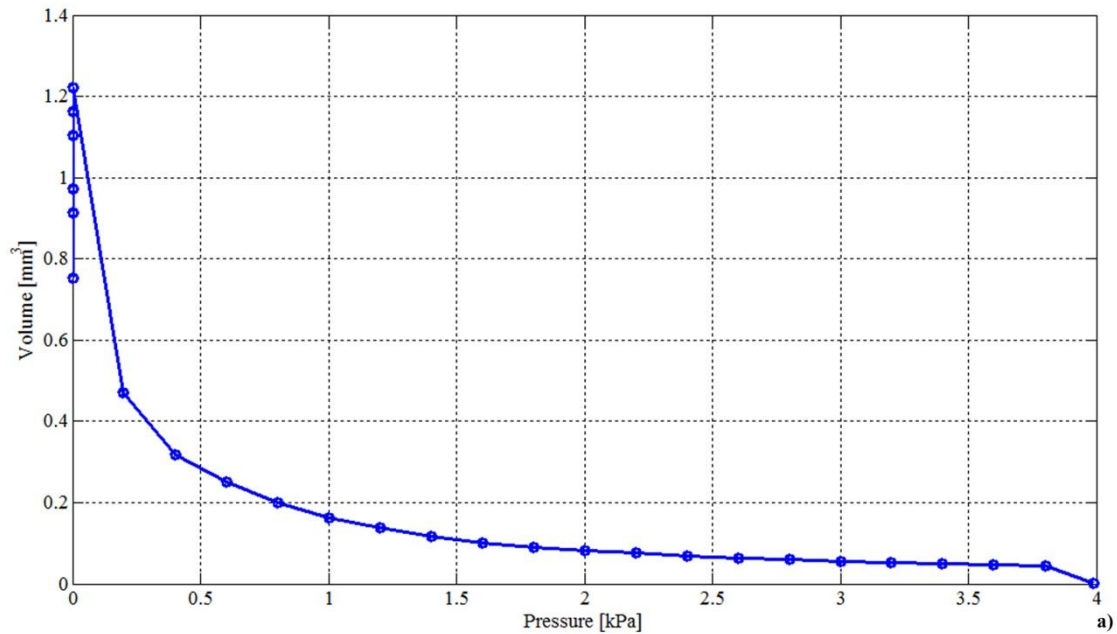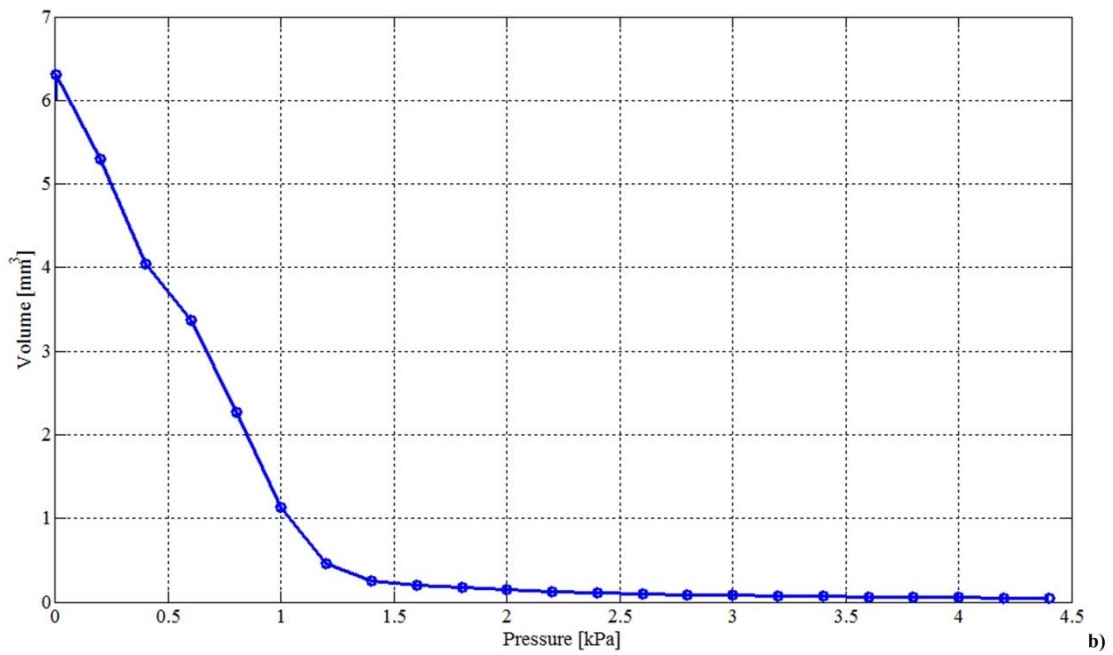
Figure 25 Graphic volume-external pressure.

Intraluminal pressure values 0.1 kPa in (a) and 1 kPa in (b).

The graphic volume-time presents a pattern which tends to zero in the occlusion phase, to demonstrate that the complete occlusion is realized.

Increasing the external pressure, the volume decreases to zero.

3.2.4 Model B

Model B is realized to test the Matlab program in a longer model with more elements along the longitudinal direction.

Considering the configuration lengths of 3 mm, the model is composed by 72800 nodes (13784 and 62168 nodes, respectively, in dense connective layer and loose stratum and 3152 nodes in common) and 53265 element (7959 and 45306 elements, respectively, in dense connective layer and loose stratum). Along longitudinal direction are set 3 elements 1 mm long (Figure 26).
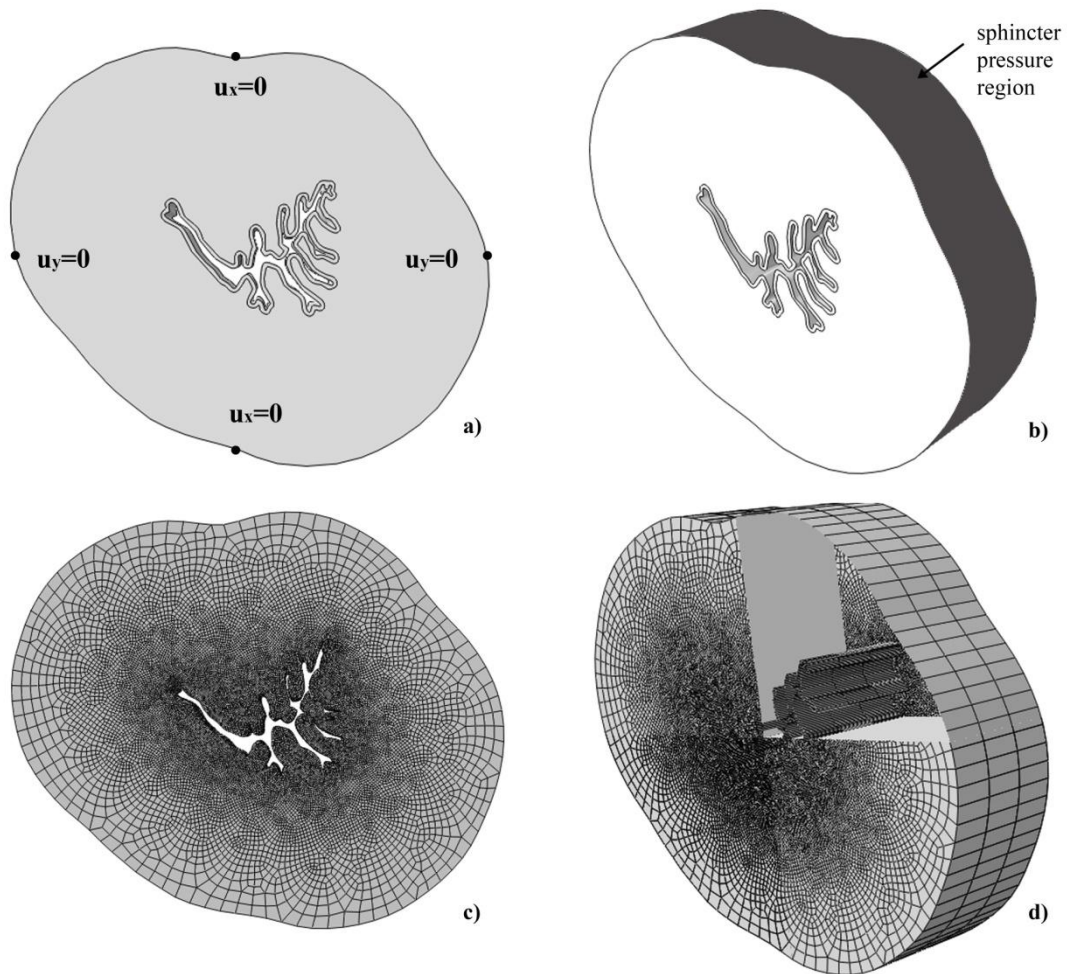

Figure 26 Model of the urethral duct. Geometrical model of the urethra transversal section (a). Three dimensional solid model of the urethral duct showing the assumed boundary (a) and loading (b) conditions. Finite element discretization: transversal section (c); three dimensional representation of urethral duct with spongy region and dense connective tissue layer (d).

Pressure field is distributed uniformly and symmetrically along the length of the urethral duct; the external pressure values 10 kPa while intraluminal pressure is realized

with fluid cavity with different values, 0.1 kPa, 0.5 kPa and 1 kPa.

So, during the inflation test simulation, the urethra is progressive inflated up to 0.1 kPa, 0.5 kPa or 1 kPa and then the occlusion pressure is increased up to 10 kPa (Figures 27, 28 and 29).
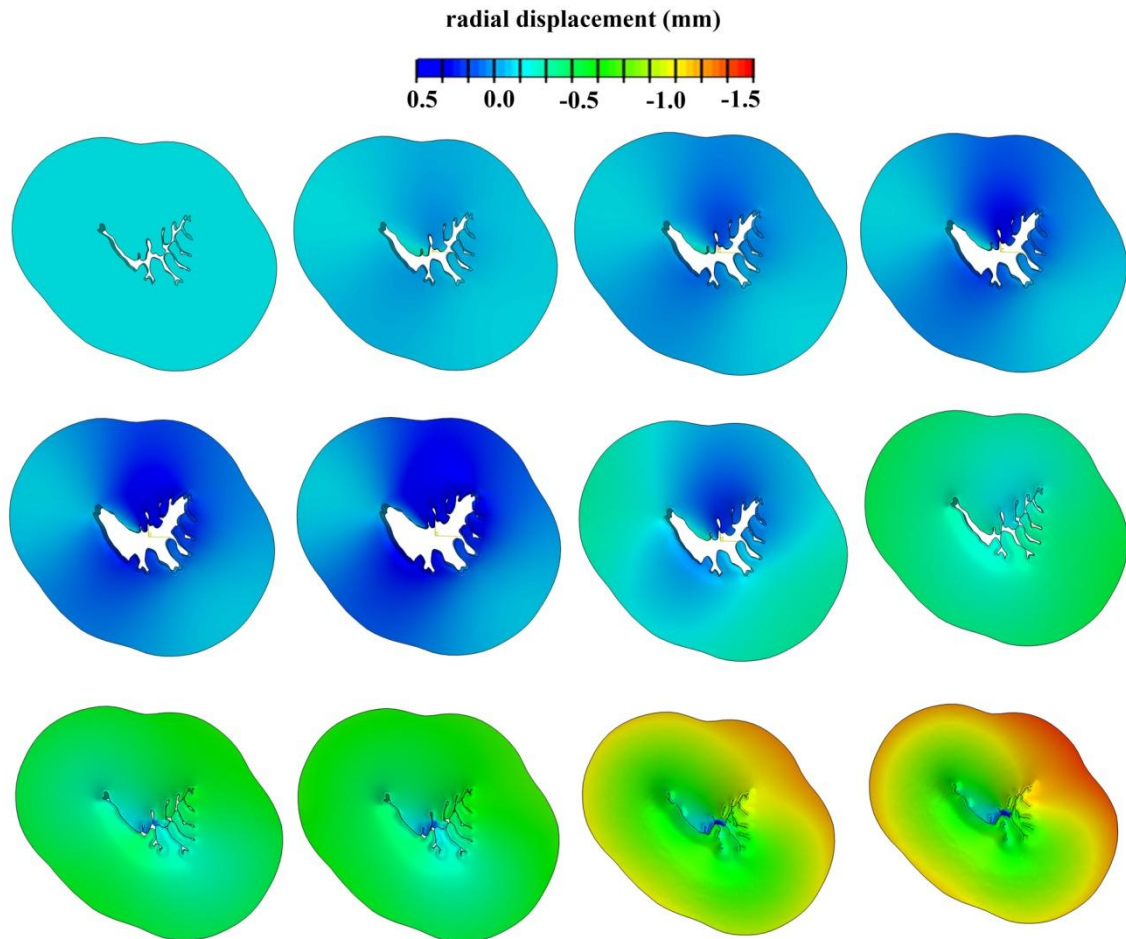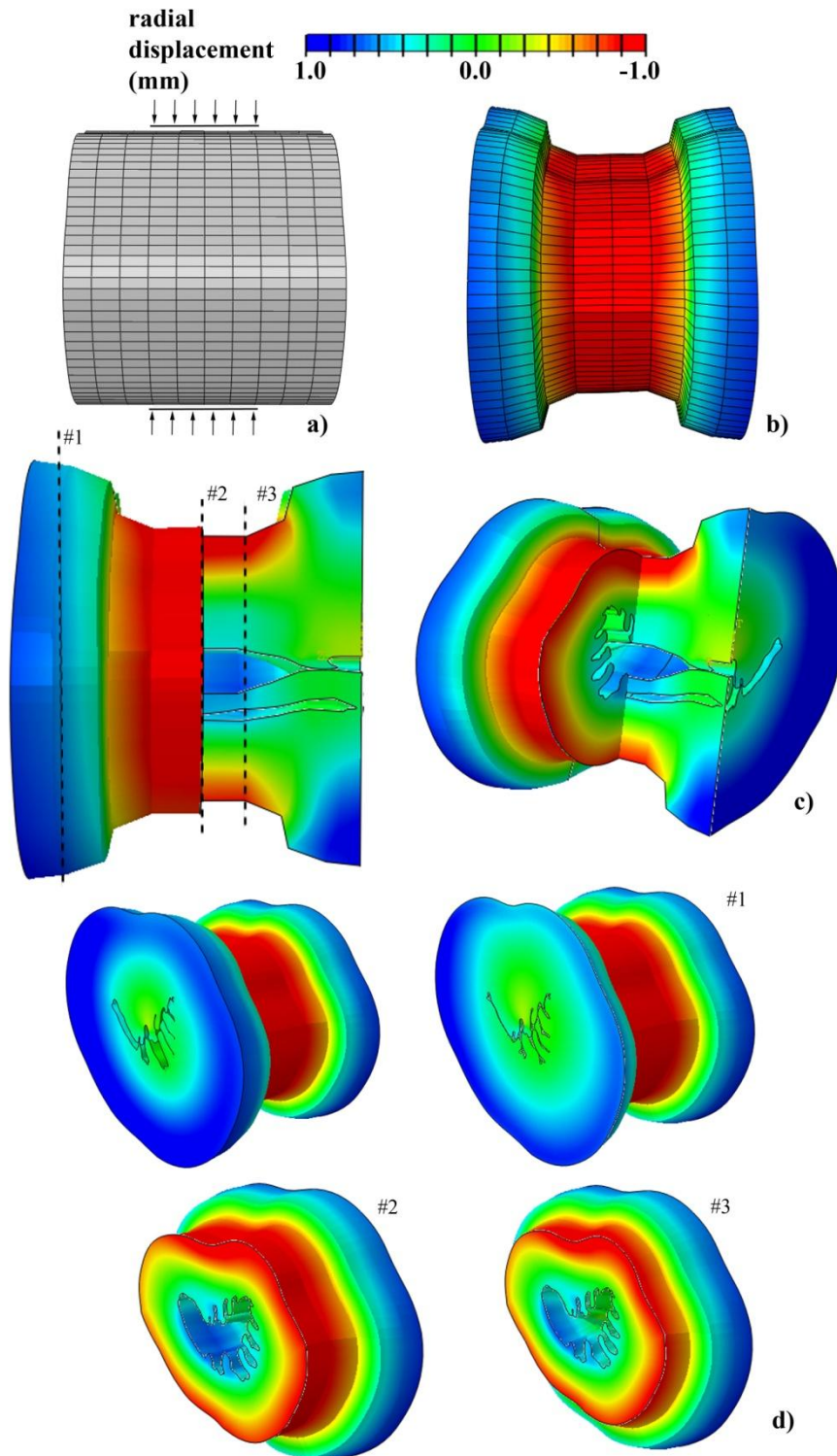

Figure 27 Contours of radial displacement field at intraluminal pressure of 0.1 kPa.
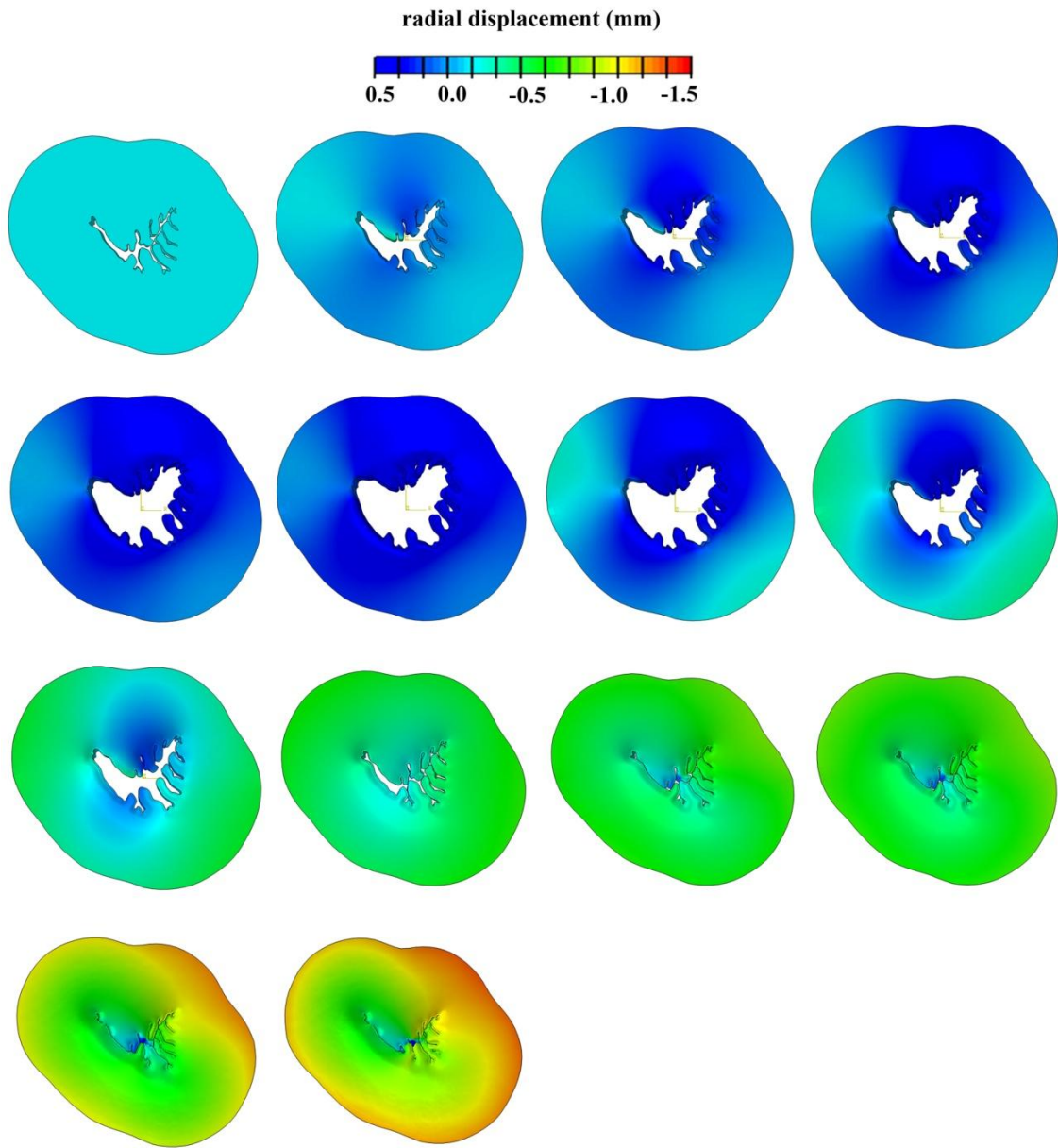
Figure 28 Contours of radial displacement field at intraluminal pressure of 0.5 kPa.
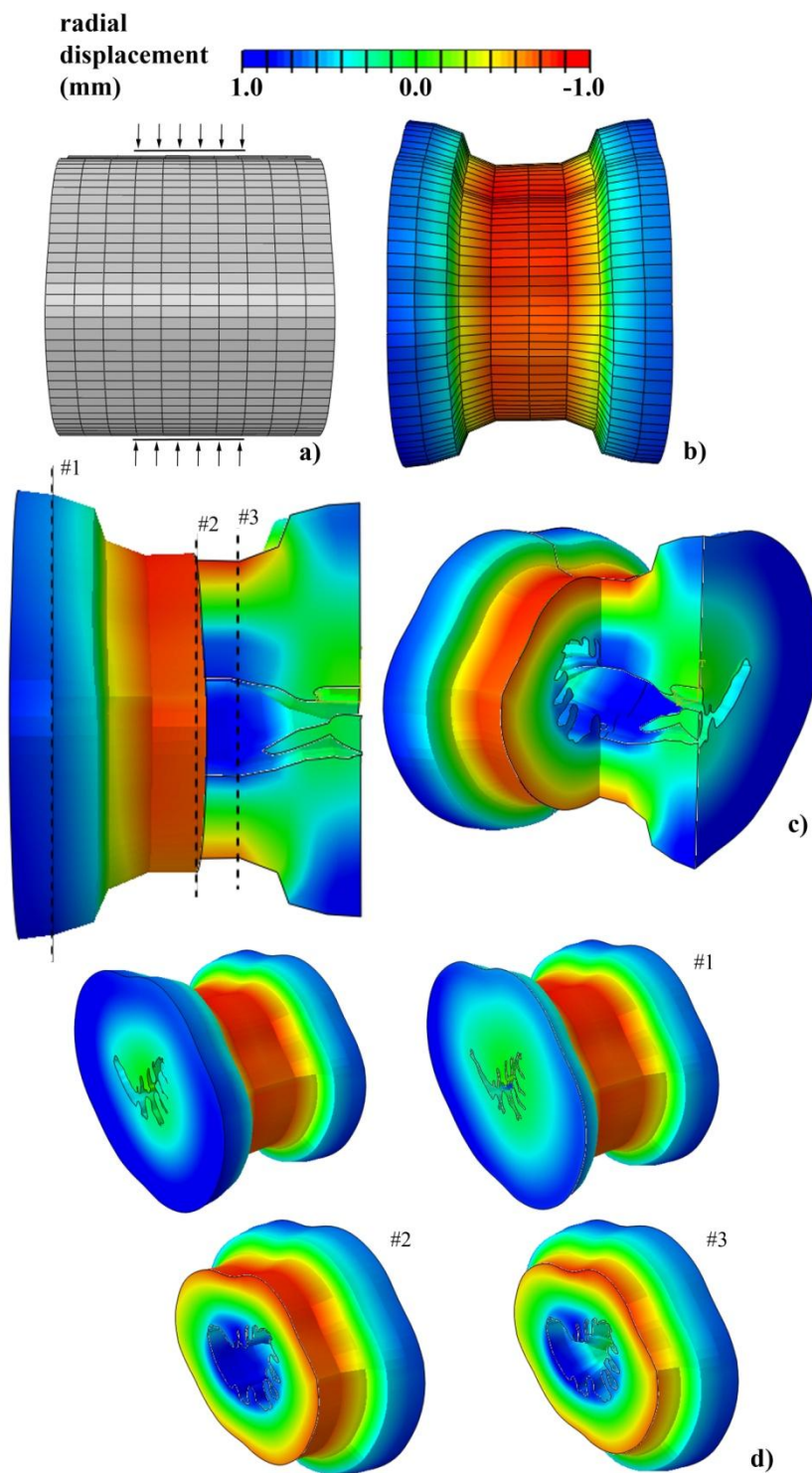
radial displacement (mm)

0.5   0.0   -0.5   -1.0   -1.5
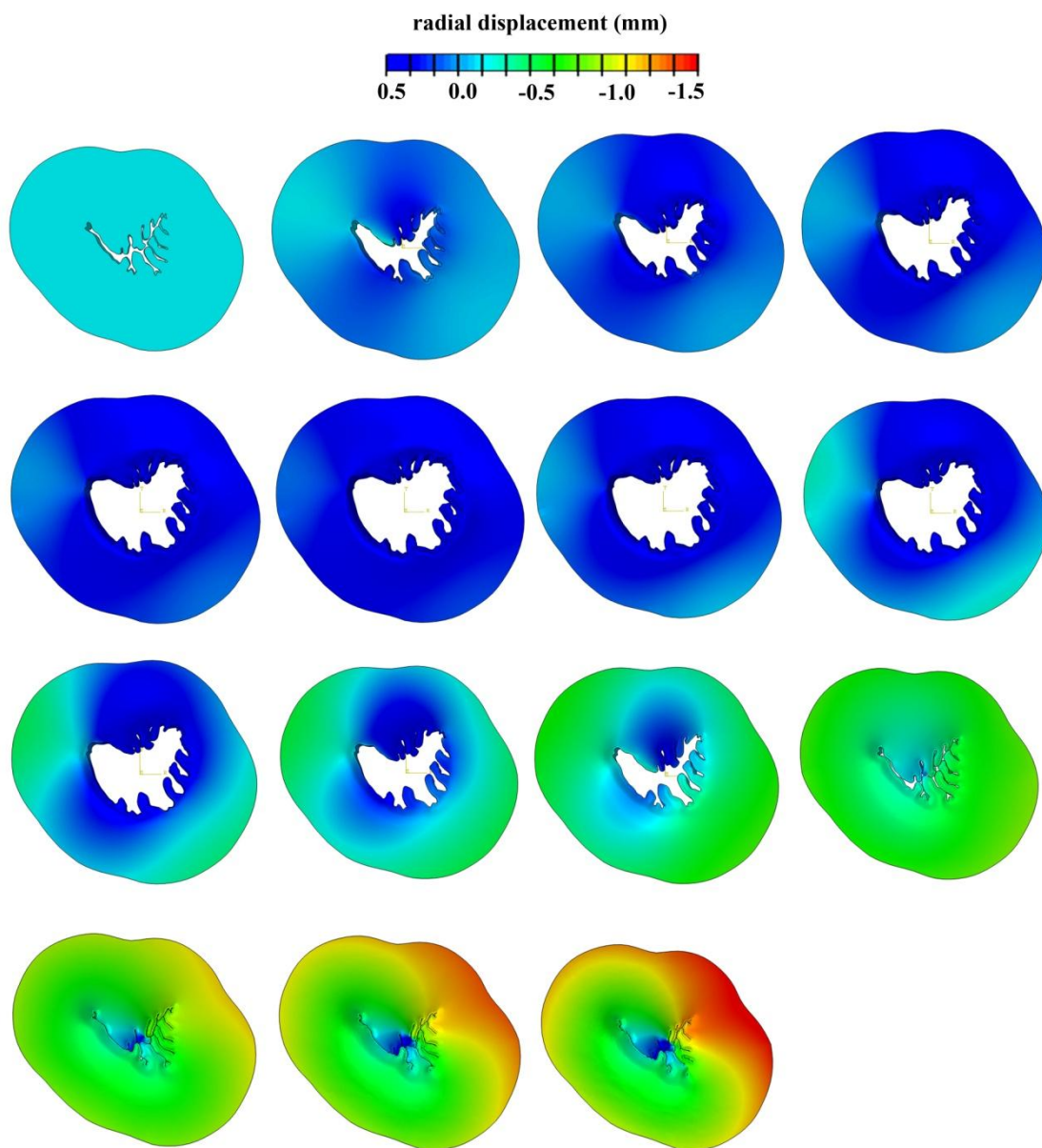
Figure 29 Contours of radial displacement field at intraluminal pressure of 1 kPa.

Figure 30 shows compressive strain field, as the minimum principal value of the logarithmic strain tensor at different intraluminal pressure of 0.1 kPa, 0.5 kPa and 1 kPa.
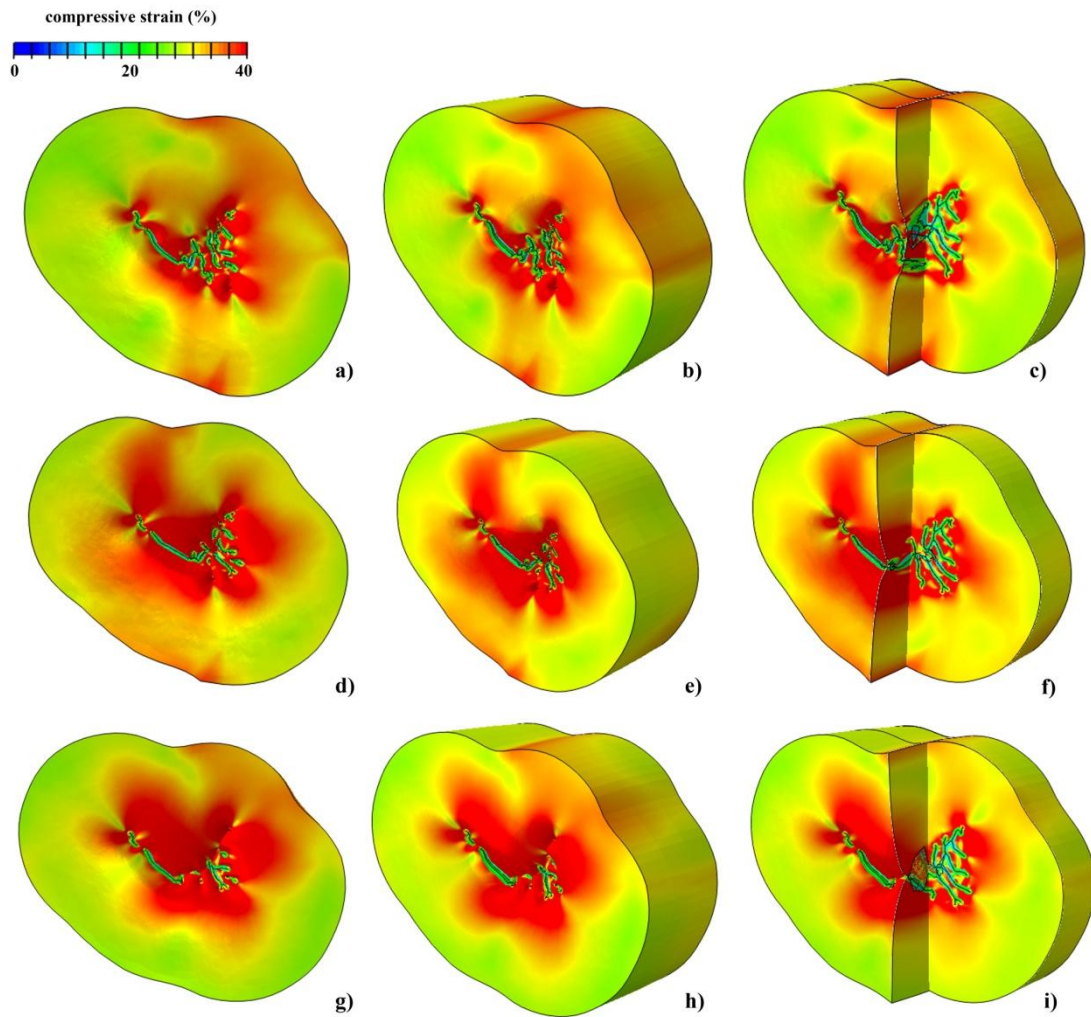
Figure 30 Contours of compressive strain field, as the minimum principal value of the logarithmic strain tensor at intraluminal pressure of 0.1 kPa a), b), c), of 0.5 kPa d), e), f) and of 1 kPa g), h), i).

Considering different values of internal pressure, when the duct getting larger, in the initial phase, the volume increases up to 12 mm^3, 27 mm^3 and 47 mm^3 in case of internal pressure of 0.1 kPa, 0.5 kPa and 1 kPa respectively and then, in the occlusion phase, the volume decrease down to zero (Figure 31).

a)

b)
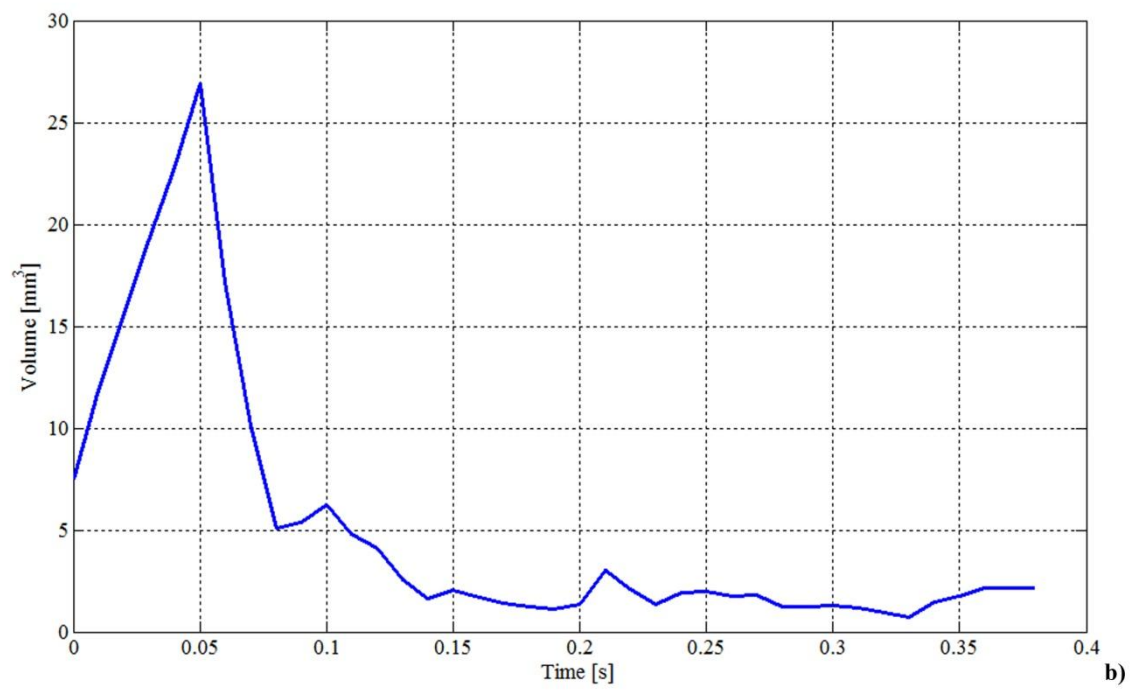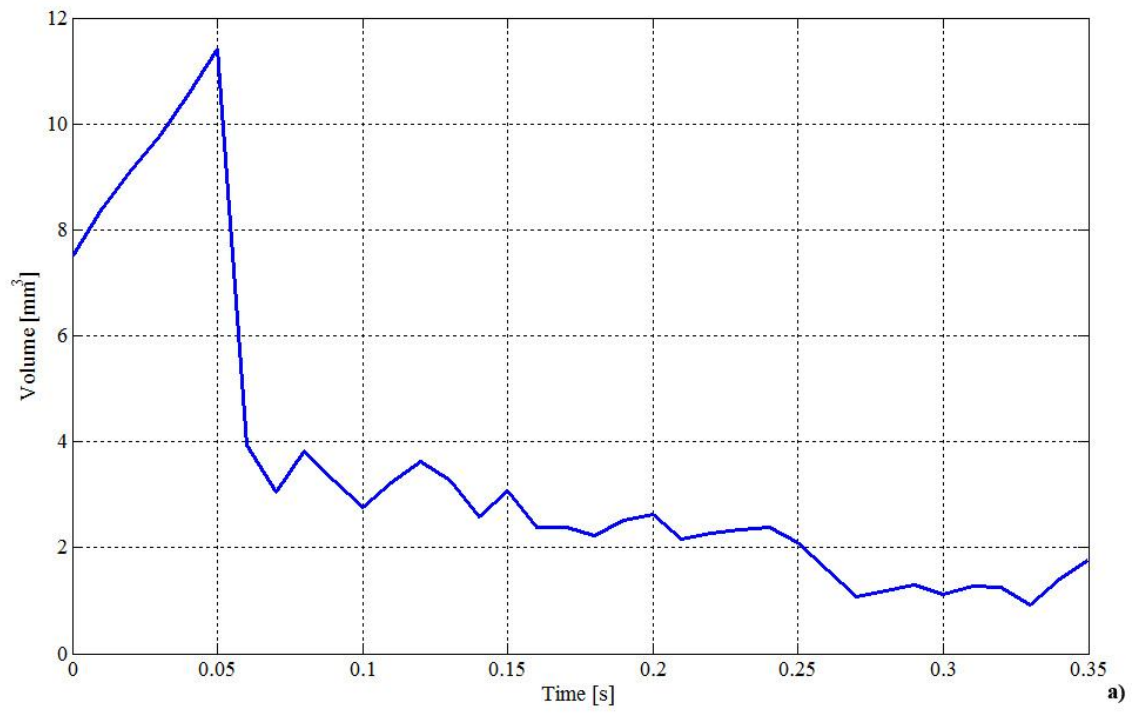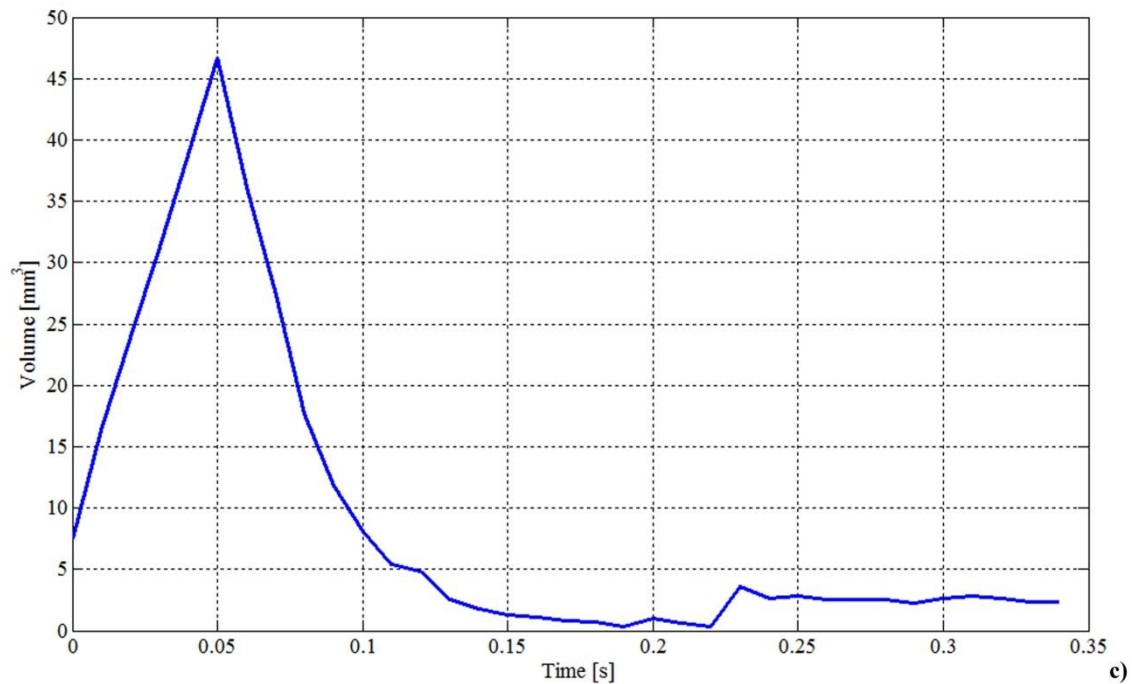
Figure 31 Graphic volume-time.

Intraluminal pressure values 0.1 kPa in (a), 0.5 kPa in (b) and 1 kPa in (c).

The volume is calculated with a specific routine implemented in Matlab (The MathWorks Inc., Natick, MA, USA). The Matlab program calculates the volume in the various time instants. Starting from the coordinates of the nodes, is calculated the area of every sections created with mesh action. Computed all areas, the volume is calculated using the formula of the pyramid trunk.

The external pressure occludes more slowly the structure with a greater internal pressure. In fact, in the first case there is an immediate occlusion while in second one the occlusion is slower, as shown in Figure 31.

The relationships between volume and external pressure for different values of intraluminal pressure are reported in Figure 32.

a)

b)

Figure 32 Graphic volume-external pressure.

Intraluminal pressure values 0.1 kPa in (a), 0.5 kPa in (b) and 1 kPa in (c).

The graphic volume-time presents a pattern which tends to zero in the occlusion phase, to demonstrate that the complete occlusion is realized.

Increasing the external pressure, the volume decreases to zero.

3.3 Realistic models

To realize models that are able to mimic the action of the artificial sphincter, models with length of 10 mm and 20 mm are considered. In these models are used different loading conformations, in particular different position of loading and force intensity.

3.3.1 Model C

Considering the configuration lengths 10 mm, the model is composed by 136686 nodes (36443 and 108911 nodes, respectively, in dense connective layer and loose stratum and 8668 nodes in common) and 119810 element (25200 and 94610 elements, respectively, in dense connective layer and loose stratum). 10 elements measuring 1mm are set along longitudinal direction (Figure 33).
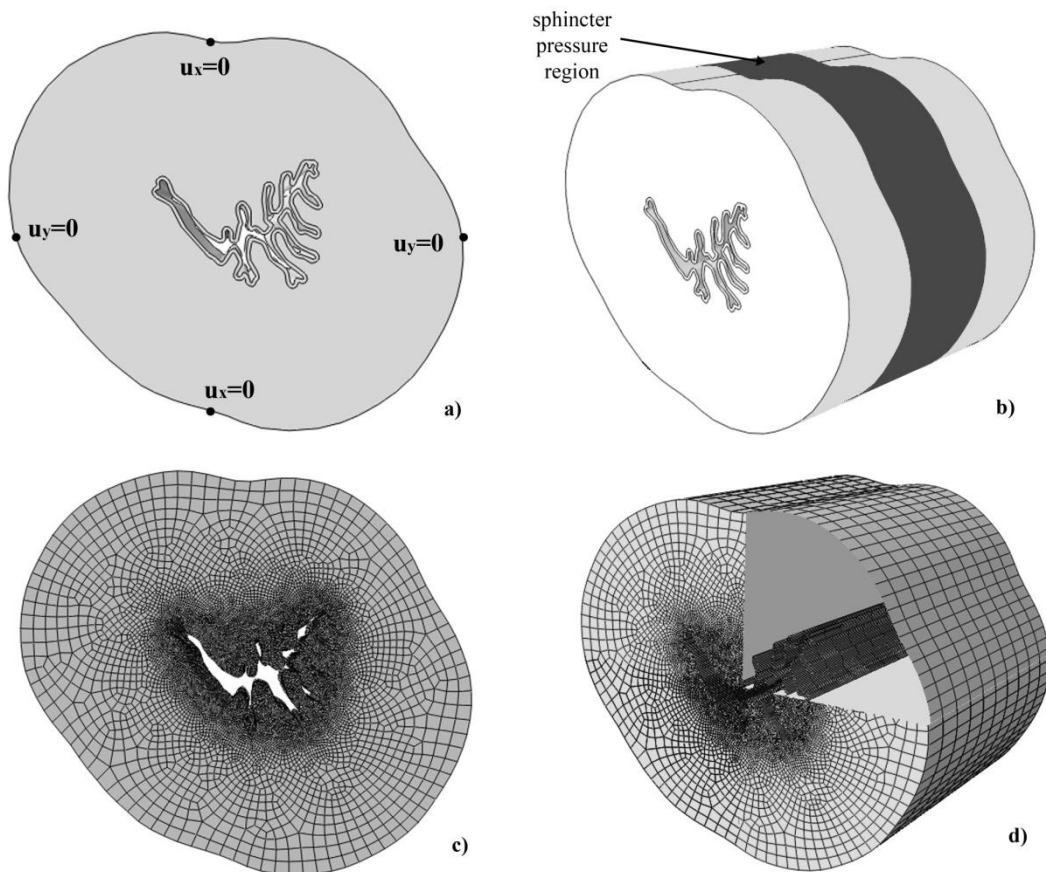
Figure 33 Model of the urethral duct. Geometrical model of the urethra transversal section (a). Three dimensional solid model of the urethral duct showing the assumed boundary (a) and loading (b) conditions. Finite element discretization: transversal section (c); three dimensional representation of urethral duct with spongy region and dense connective tissue layer (d).

Pressure field is distributed uniformly and symmetrically along the length of the urethral duct; the external pressure values 10 kPa on the 4 mm in the central portion while intraluminal pressure is realized with fluid cavity and takes the following values: 0.1 kPa, 0.5 kPa and 1 kPa. So, during the inflation test simulation, the urethra is progressive inflated up 0.1 kPa, 0.5 kPa or 1 kPa and then the occlusion pressure is increased up to 10 kPa (Figure 34, 35 and 36).
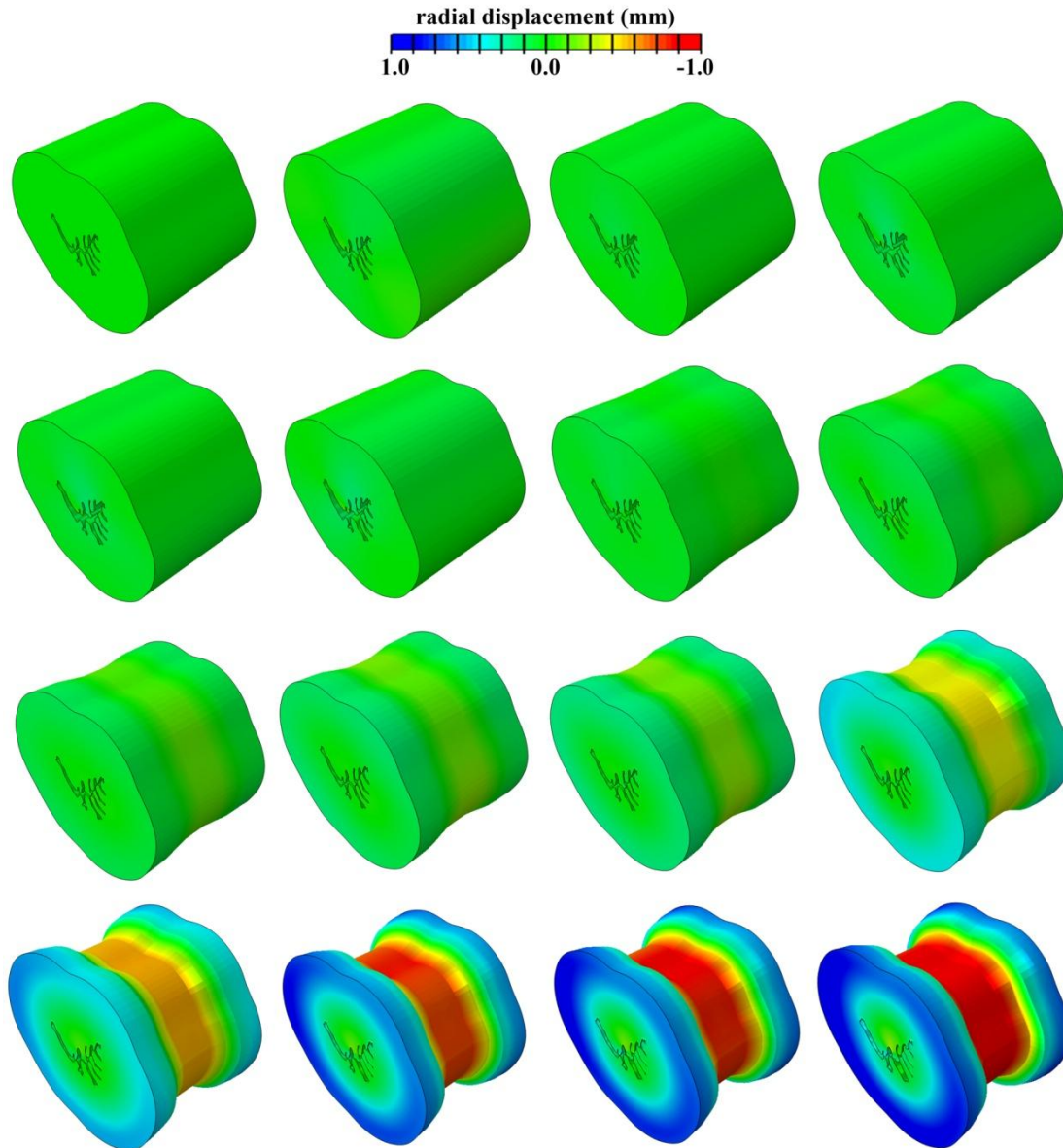
Figure 34 Contours of radial displacement field at intraluminal pressure of 0.1 kPa.
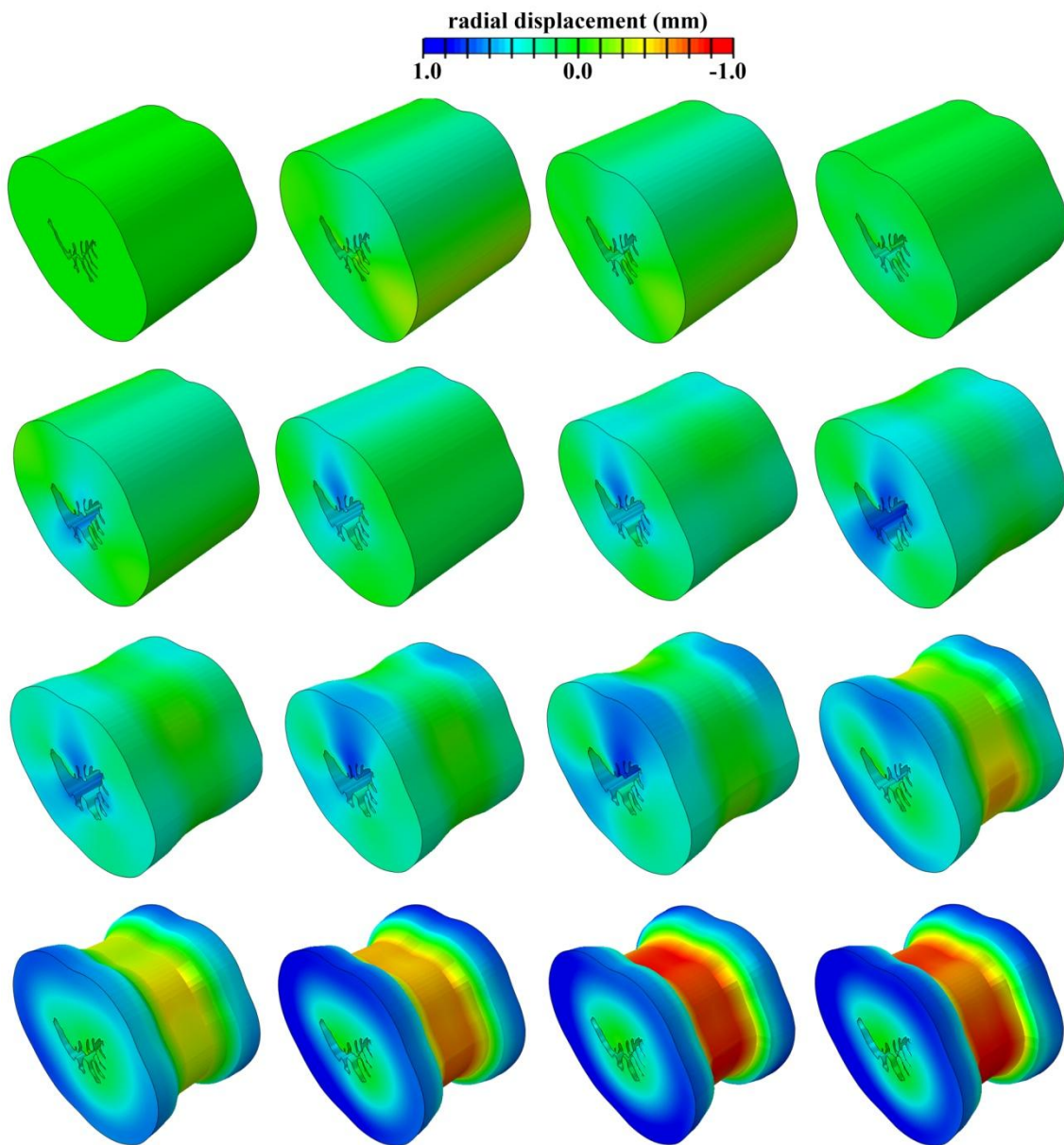
Figure 35 Contours of radial displacement field at intraluminal pressure of 0.5 kPa.
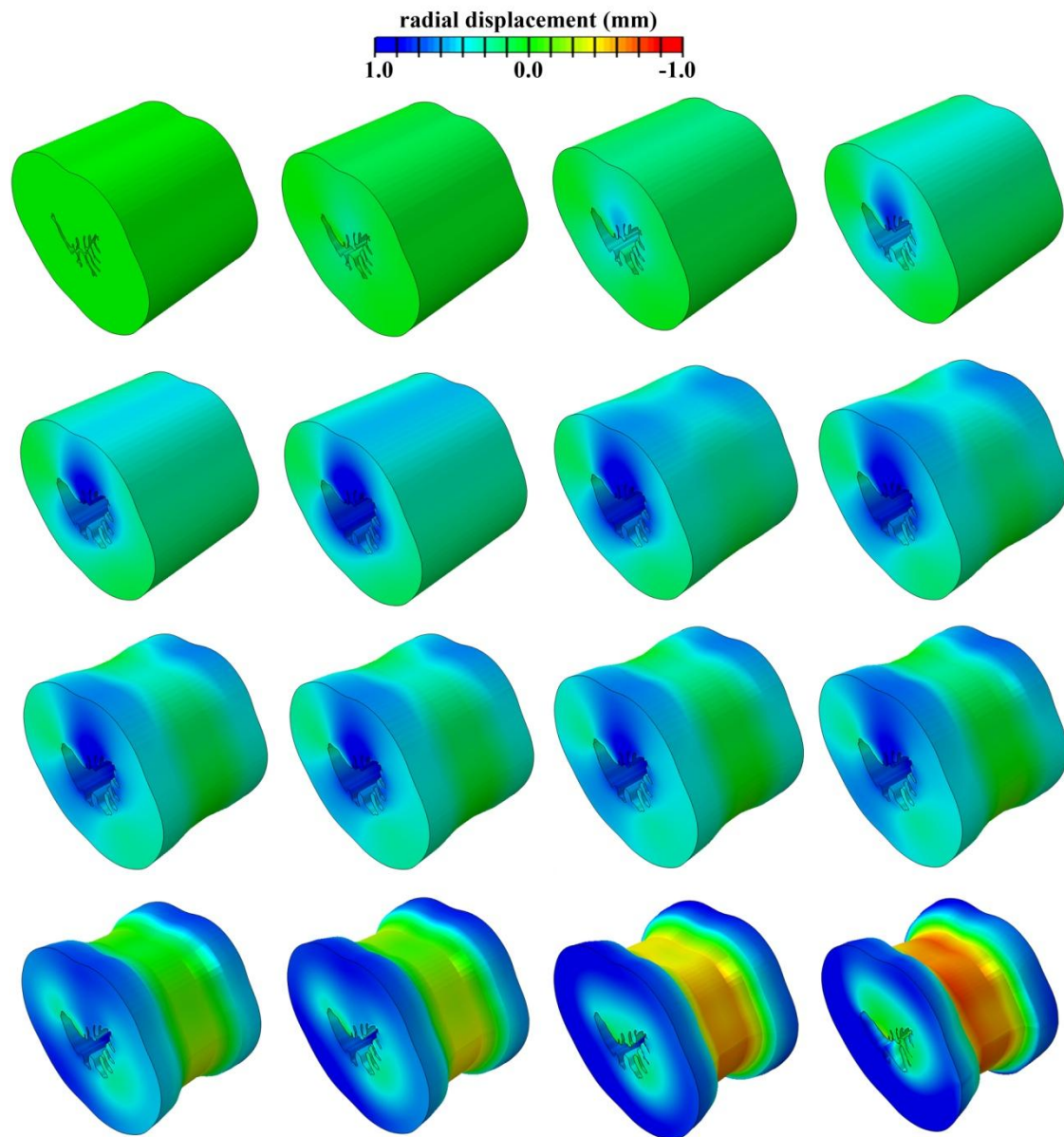
Figure 36 Contours of radial displacement field at intraluminal pressure of 1 kPa.

Results achieved about the behavior of the structure under different intraluminal pressures are reported in the following figures.

Figures 37, 38 and 39 show behaviors about radial displacement field respect three different pressures, as 0.1 kPa, 0.5 kPa and 1 kPa respectively.

Figure 37 Numerical analysis of urethra occlusion by a pressure of 0.1 kPa on the central portion: radial displacement field. Contours are reported on the undeformed (a) and deformed (b) 3D model, on longitudinal section (c) and subsequent transversal sections #1, #2 and #3 (d).

Figure 38 Numerical analysis of urethra occlusion by a pressure of 0.5 kPa on the central portion: radial displacement field. Contours are reported on the undeformed (a) and deformed (b) 3D model, on longitudinal section (c) and subsequent transversal sections #1, #2 and #3 (d).
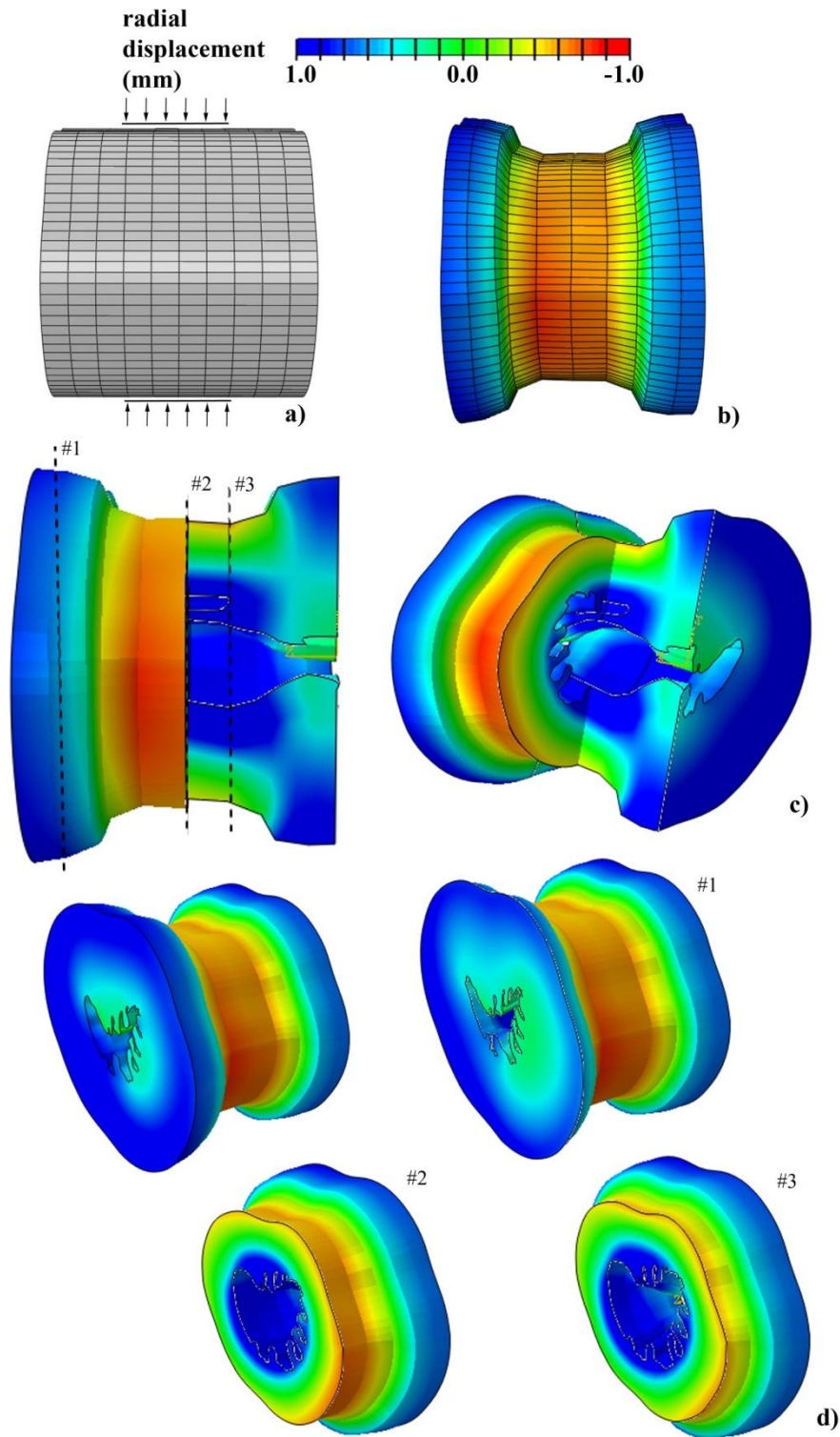
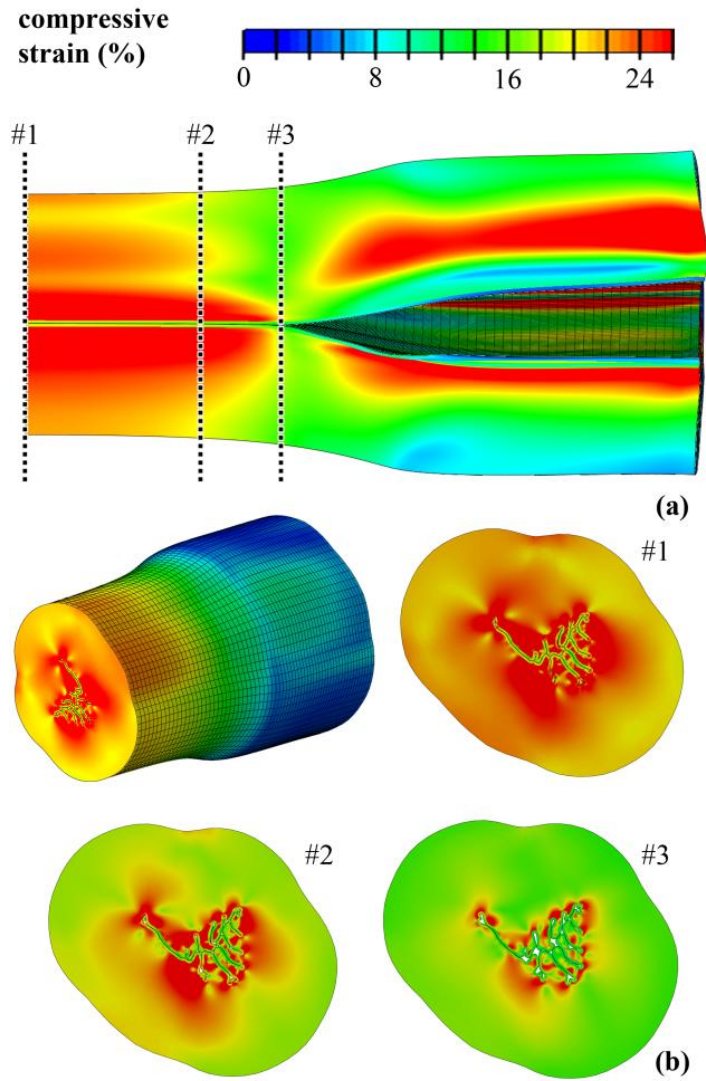**Figure 39** Numerical analysis of urethra occlusion by a pressure of 1 kPa on the central portion: radial displacement field. Contours are reported on the undeformed (a) and deformed (b) 3D model, on longitudinal section (c) and subsequent transversal sections #1, #2 and #3 (d).

Figures 40, 41 and 42 show behaviors about compressive strain field respect three different pressures, as 0.1 kPa, 0.5 kPa and 1 kPa respectively.
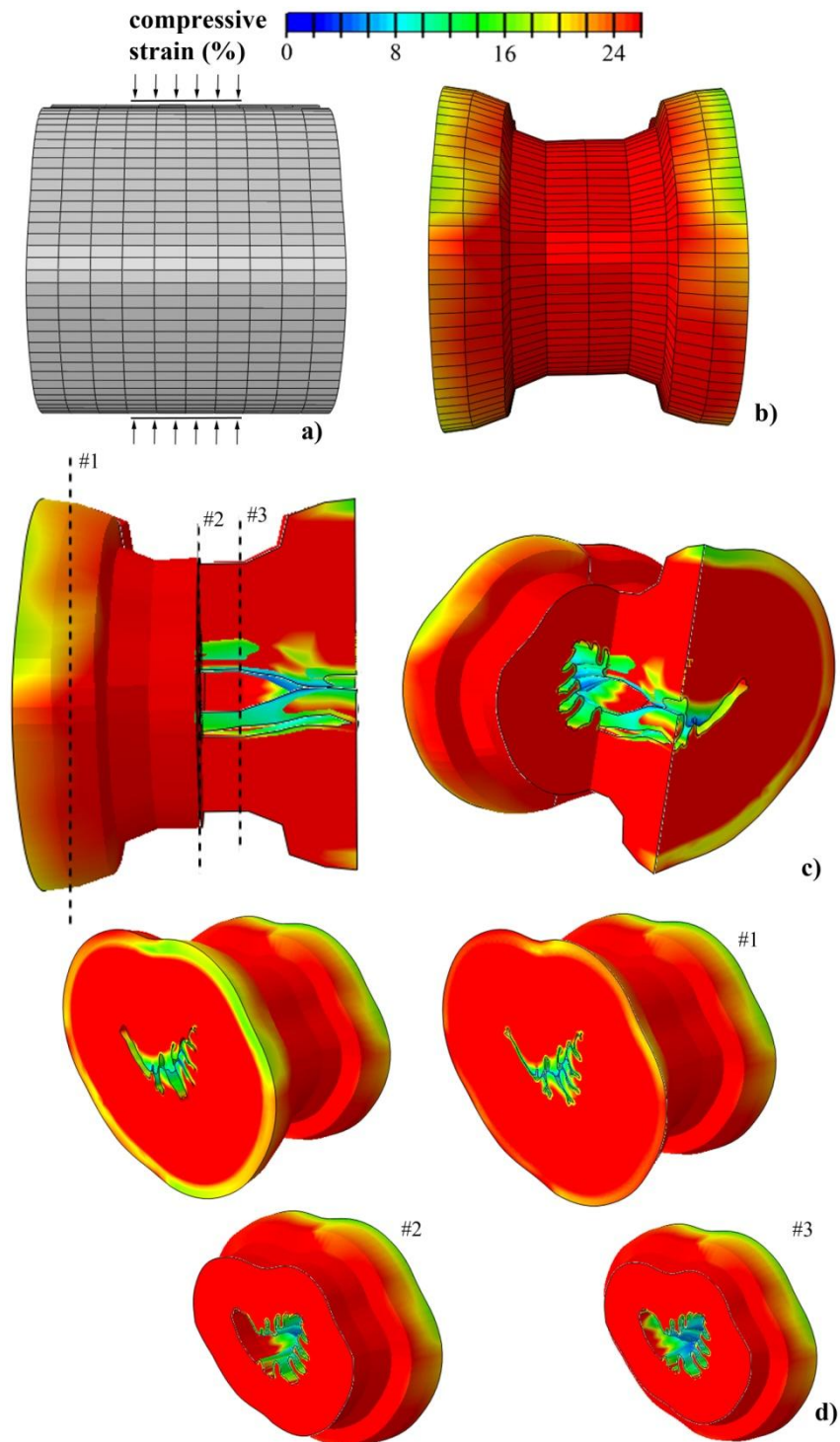
Figure 40 Numerical analysis of urethra occlusion by a pressure of 0.1 kPa on the central portion: compressive strain field. Contours are reported on the undeformed (a) and deformed (b) 3D model, on longitudinal section (c) and subsequent transversal sections #1, #2 and #3 (d).
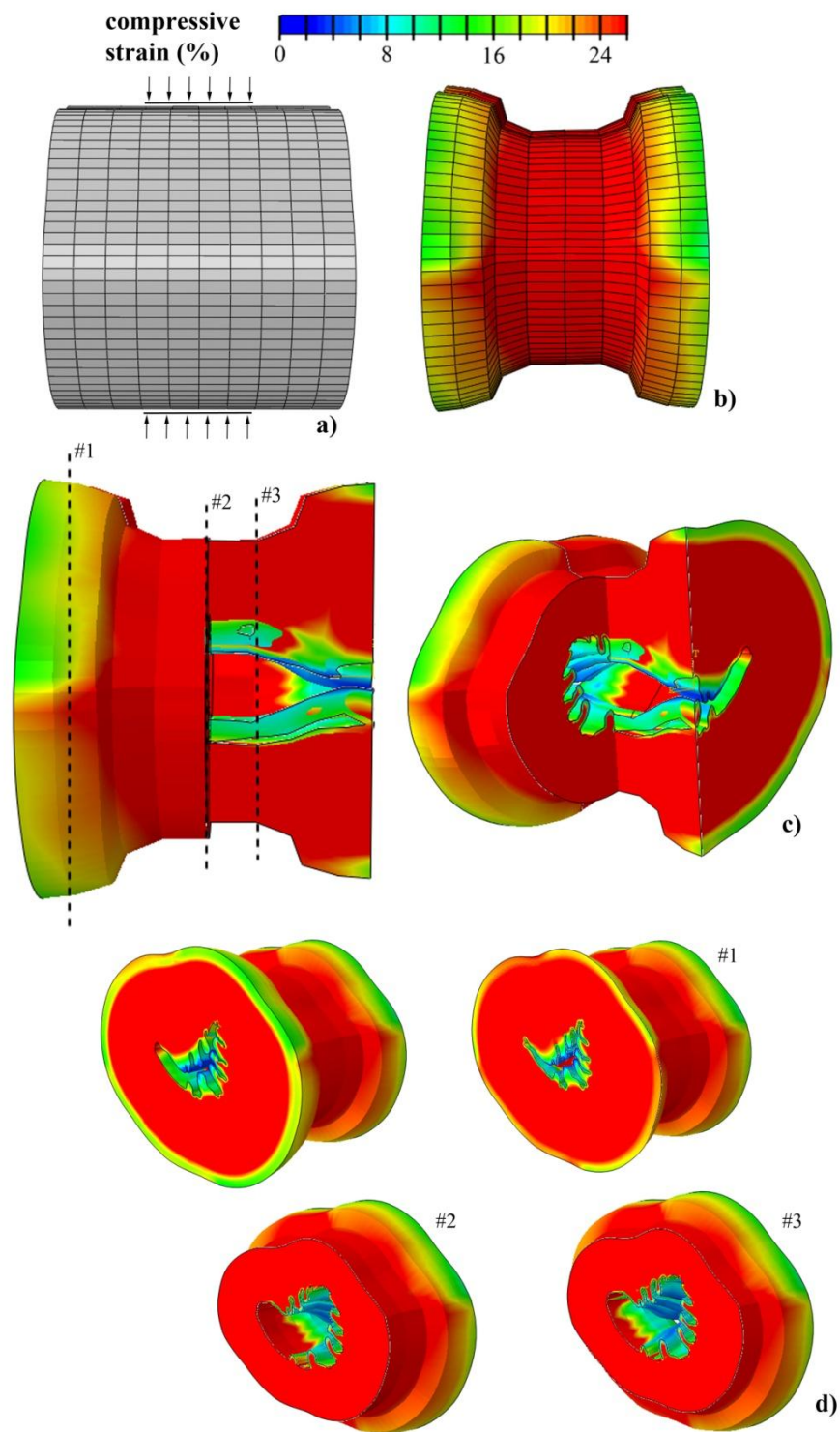
Figure 41 Numerical analysis of urethra occlusion by a pressure of 0.5 kPa on the central portion: compressive strain field. Contours are reported on the undeformed (a) and deformed (b) 3D model, on longitudinal section (c) and subsequent transversal sections #1, #2 and #3 (d).
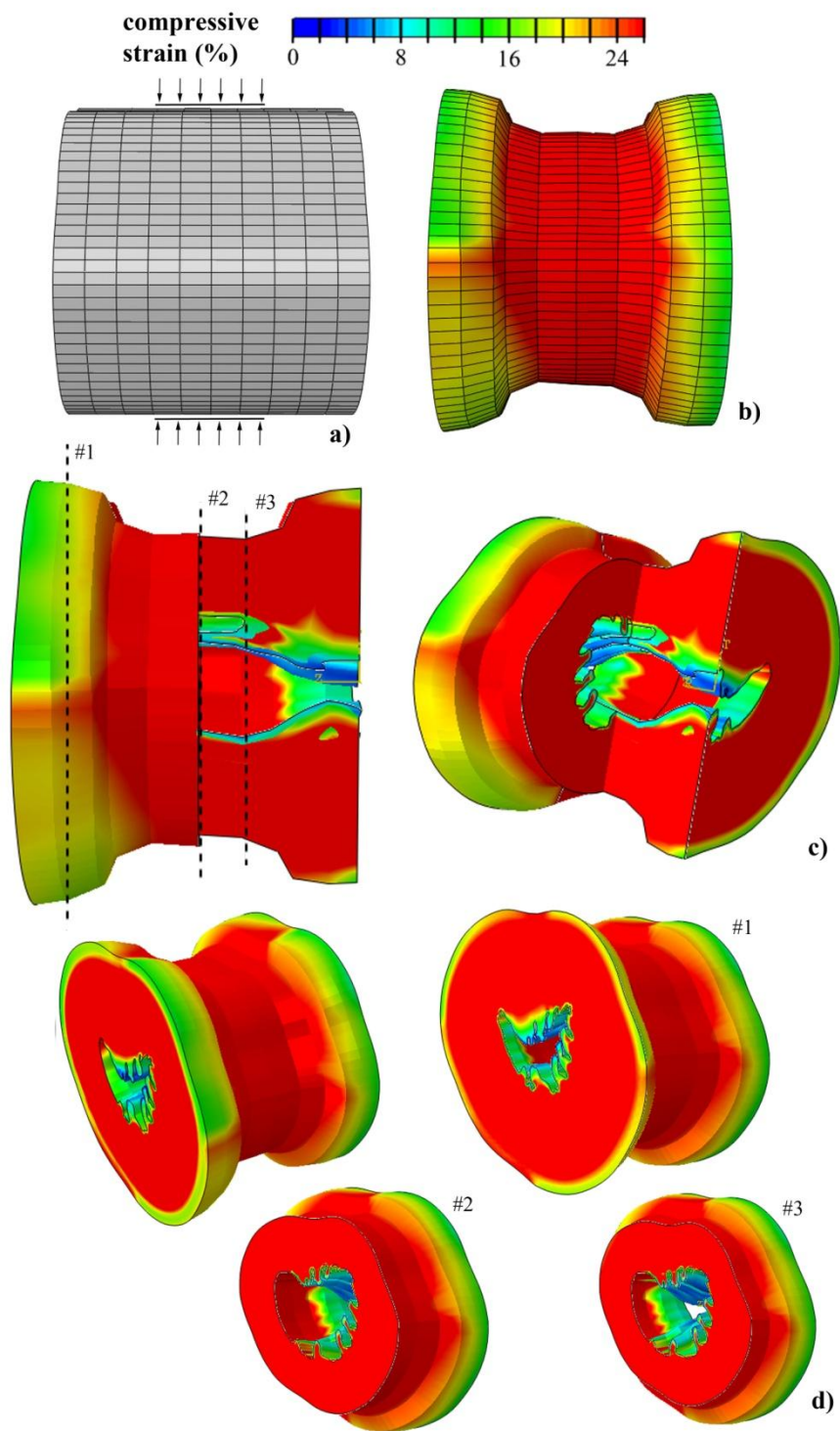
Figure 42 Numerical analysis of urethra occlusion by a pressure of 1 kPa on the central portion: compressive strain field. Contours are reported on the undeformed (a) and deformed (b) 3D model, on longitudinal section (c) and subsequent transversal sections #1, #2 and #3 (d).

3.3.2 Model D

Considering the configuration lengths 20 mm, the model is composed by 896444 nodes and 854049 elements. In particular, 67 elements measuring 0.3mm are set along longitudinal direction (Figure 43).
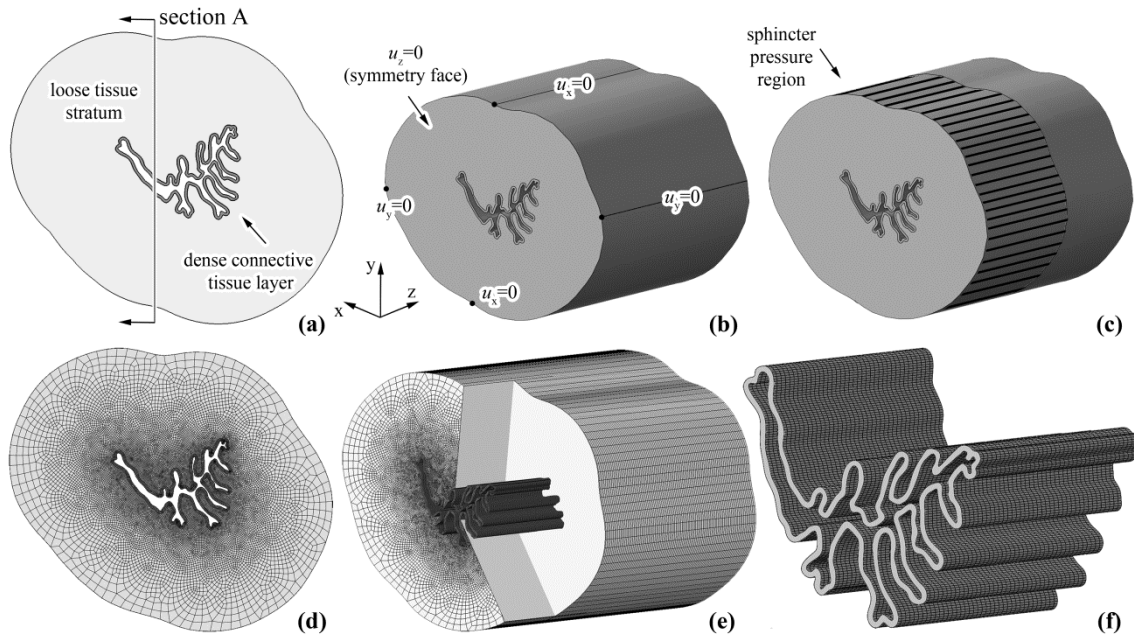
Figure 43 Model of the urethral duct. Geometrical model of the urethra transversal section and identification of constituent tissues (a). Three dimensional solid model of the urethral duct showing the assumed boundary (b) and loading (c) conditions. Finite element discretization: transversal section (d); three dimensional representation of urethral duct with spongy region and dense connective tissue layer (e); detail of the dense connective tissue layer (f).

Pressure field is distributed uniformly and parabolically and symmetrically along the length of the urethral duct; the external pressure values 10 kPa on 10 mm of the total length while intraluminal pressure values 1 kPa. So, during the inflation test simulation, the urethra is progressively inflated up to 1 kPa and then the occlusion pressure is increased up to 10 kPa.

Figures 44 and 45 show behavior about radial displacement field with constant and parabolic external pressure respectively.
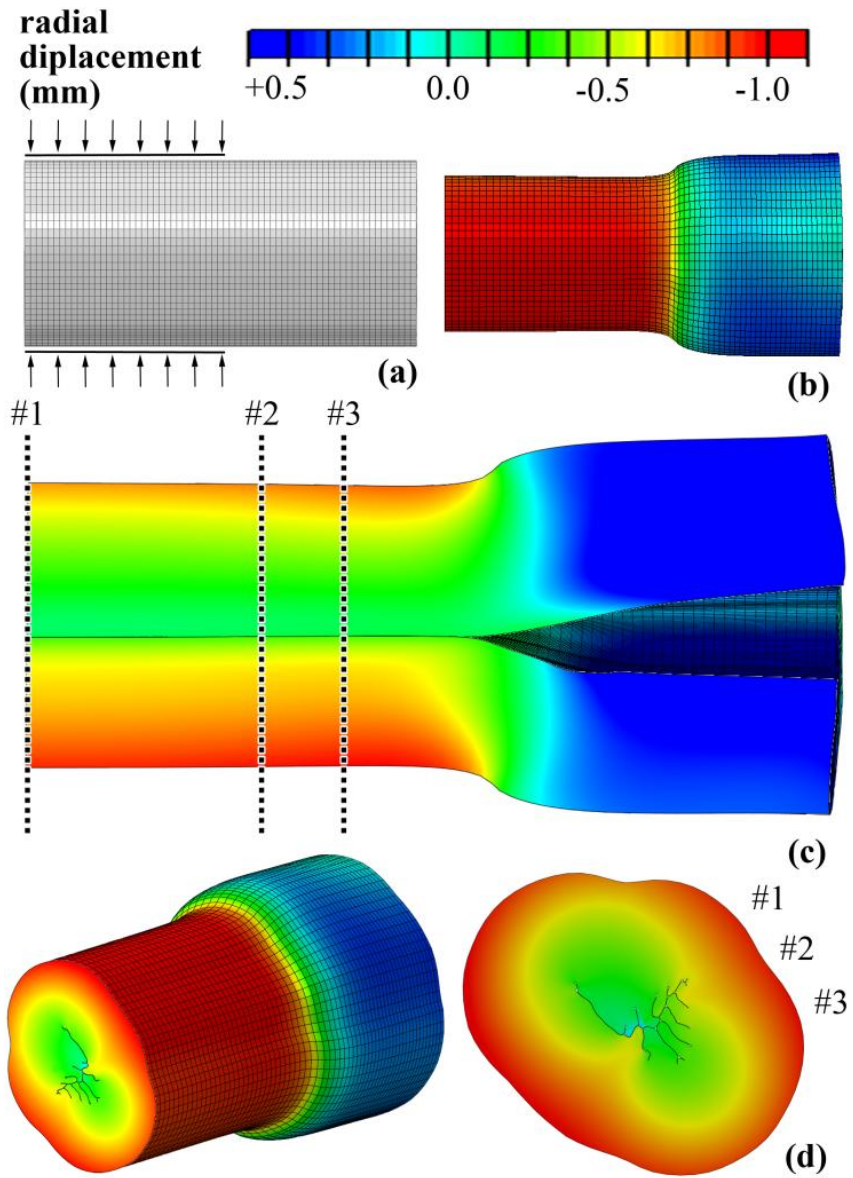
Figure 44 Numerical analysis of urethra occlusion by constant pressure cuff: radial displacement field. Contours are reported on the undeformed (a) and deformed (b) three-dimensional model, on longitudinal section A shown in Figure 43a (c) and subsequent transversal sections #1, #2 and #3 (d).
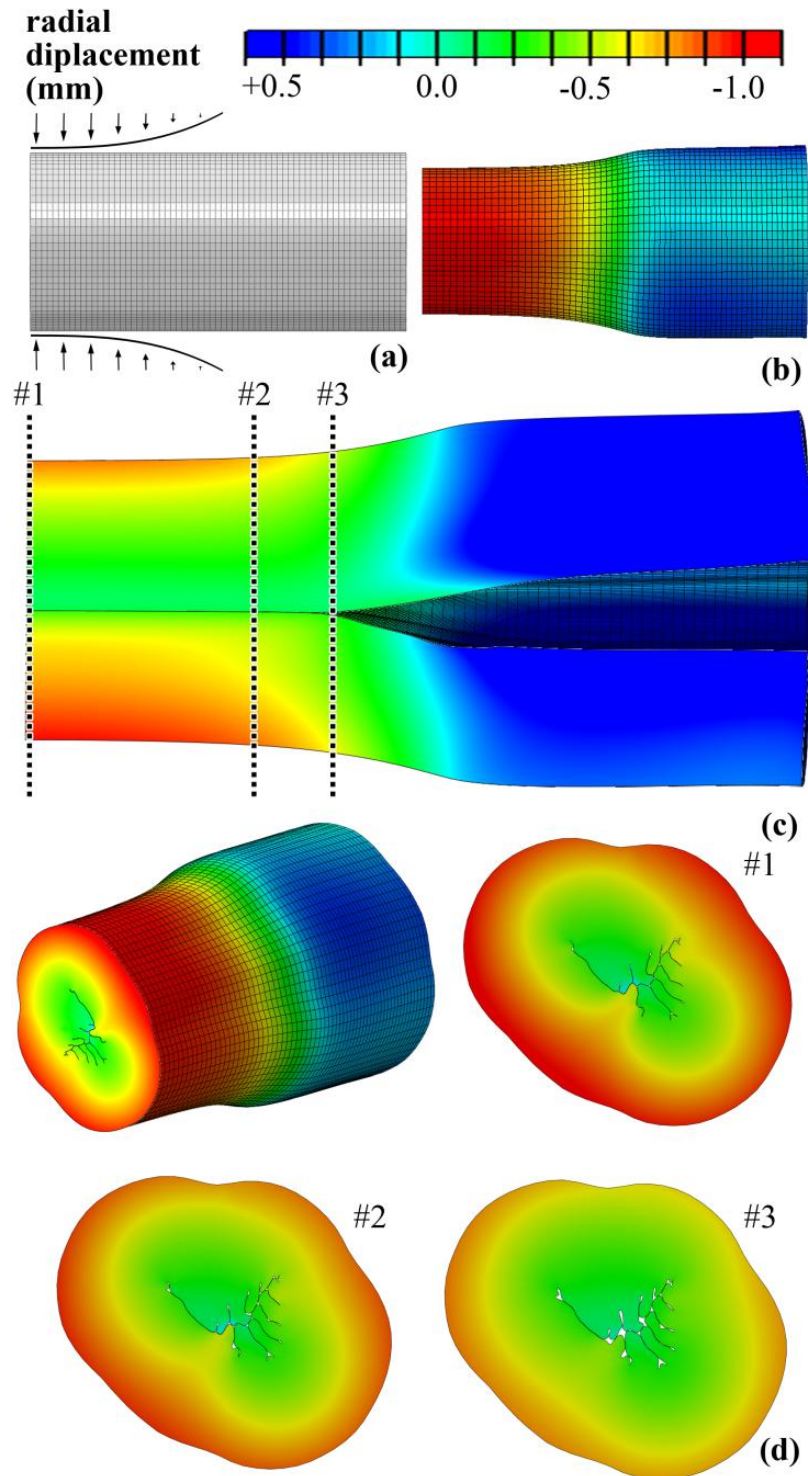
Figure 45 Numerical analysis of urethra occlusion by parabolic pressure cuff: radial displacement field. Contours are reported on the undeformed (a) and deformed (b) three-dimensional model, on longitudinal section A shown in Figure 43a (c) and subsequent transversal sections #1, #2 and #3 (d) showing the different configurations.

Figures 46 and 47 show behavior about compressive strain field (as the minimum eigenvalue of the logarithmic strain tensor) with constant and parabolic external pressure respectively.
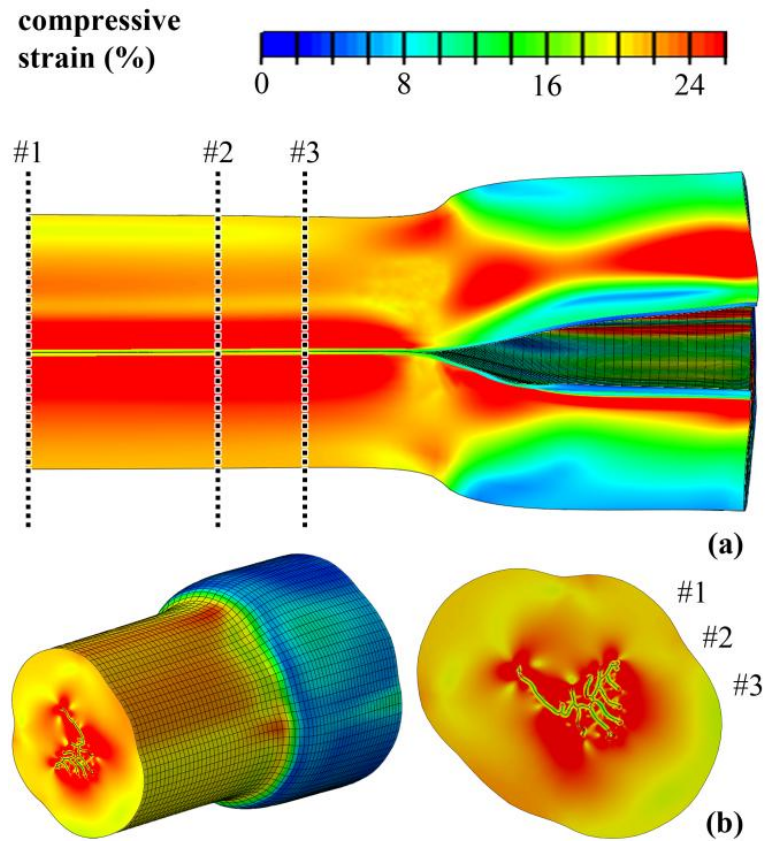
Figure 46 Numerical analysis of urethra occlusion by constant pressure cuff: compressive strain field. Contours are reported on longitudinal section A shown in Figure 43a (a) and subsequent transversal sections #1, #2 and #3 (b).

Figure 47 Numerical analysis of urethra occlusion by parabolic pressure cuff: compressive strain field. Contours are reported on longitudinal section A shown in Figure 43a (a) and subsequent transversal sections #1, #2 and #3 (b), showing the different configurations.

The compressive stress field (as the minimum eigenvalue of the Cauchy stress tensor) induced by the cuff action is reported in Figure 48, again with differentiation by the loading schemes.
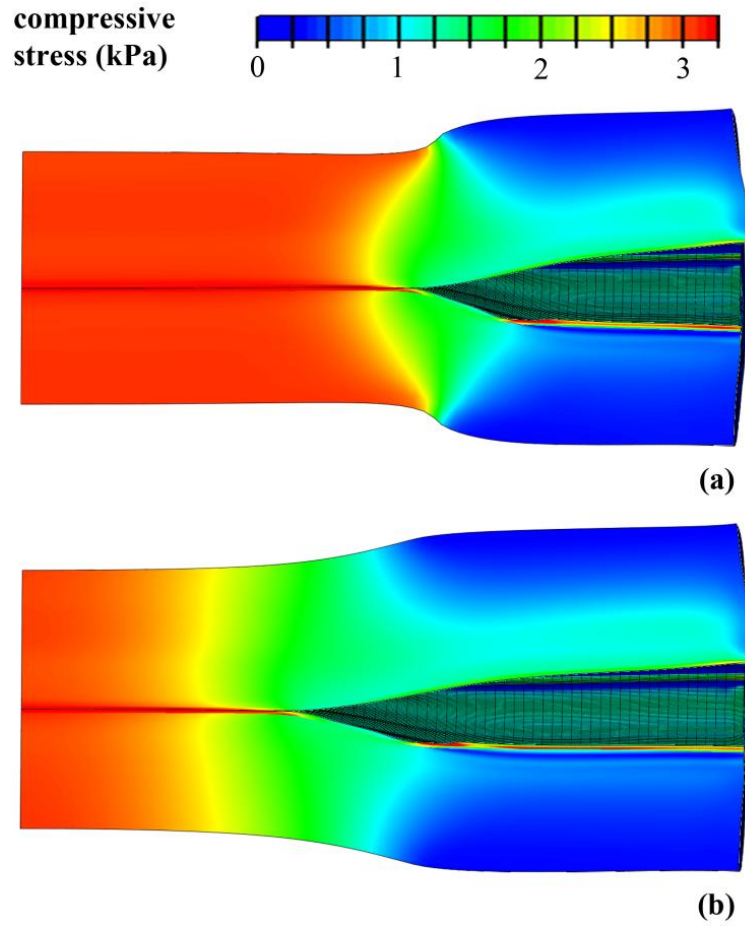
Figure 48 Numerical analysis of urethra occlusion: compressive stress field corresponding constant (a) and parabolic (b) pressure scheme.

Moreover, considering this model, the tissue behavior is investigates. Regarding compressive strain distribution, Figure 49 shows the difference between dense connective tissue layer and loose tissue stratum in according to different type of load, constant or parabolic.
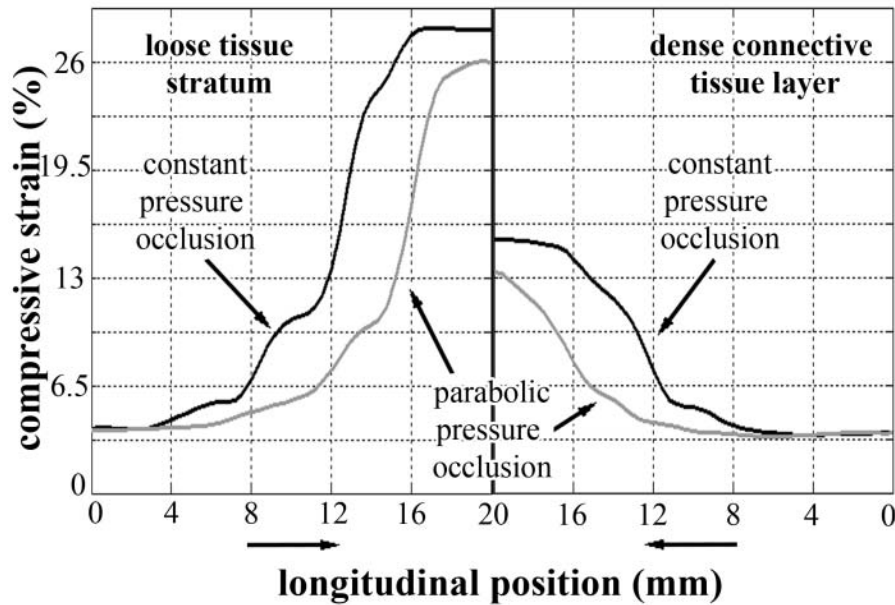
Figure 49 Compressive strain distribution along the urethral duct. Results are reported for both the loose tissue stratum (left side of the graph) and the dense connective tissue layer (right side of the graph) and for both constant (black lines) and parabolic (gray lines) occluding scheme. Data are reported with regard to the half symmetric portion 20 mm long.

Similarly, Figure 50 considers compressive stress distribution.
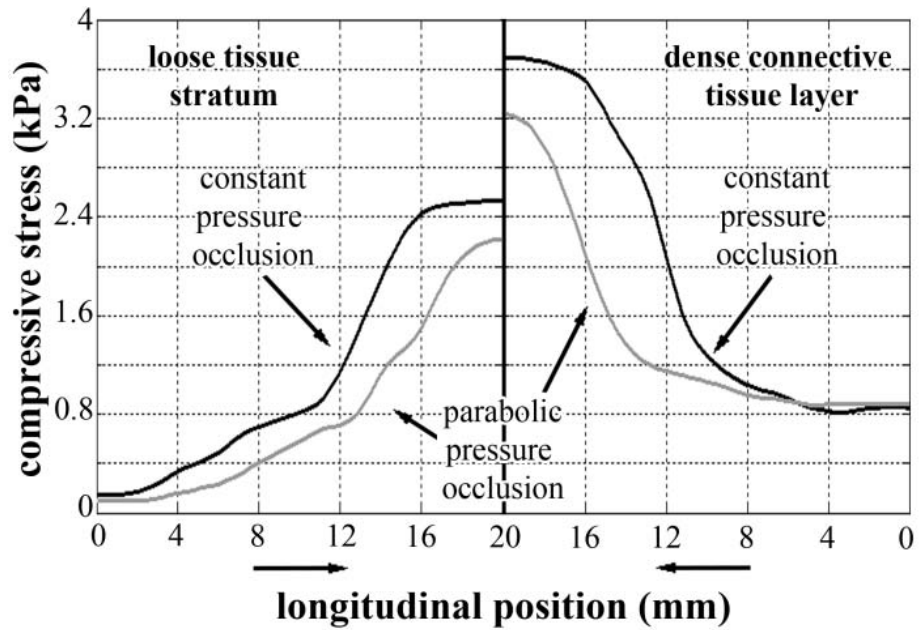
Figure 50 Compressive stress distribution along the urethral duct. Results are reported for both the loose tissue stratum (left side of the graph) and the dense connective tissue layer (right side of the graph) and for both constant (black lines) and parabolic (gray lines) occluding scheme. Data are reported with regard to the half symmetric portion 20 mm long.

For Model C and Model D, a heavy computational procedure is developed by means of analyses that operate within an explicit finite element formulation. For the high computational weight, the calculation of the volume is being processed.

CHAPTER 4

CFD MODEL

To have a more complete view about the mechanism of urination and occlusion, the conditions of urine flow in the urethral duct are analyzed. So, different conformations of urethral duct are considered in addiction on intraluminal pressure during the action of urination.

A 2D structural model is realized with the aim to investigate the behavior of urethral tissue subjected to an internal pressure up to 8 kPa, equivalent to about 80 cmH$_2$O.

The simplified geometrical model of the urethral section is imported into the finite element preprocessing software Abaqus/CAE 6.14 (Dassault Systèmes Simulia Corp., Providence, RI).

To mimic the shape of the urethra is realized an ellipse; internal horizontal and vertical diameters are 7.2 mm and 0.2 mm respectively, while external horizontal and vertical diameters are 12 mm and 7.8 mm respectively (Figure 51a).

The mechanical behavior of the specific tissue is represented by isotropic hyperelastic material, imposed as Ogden strain energy potential and with Poisson's ratio of 0.5.

Three node triangular linear elements (CPS3 plane stress elements) are adopted to mesh the urethral tissue (Figure 51b).
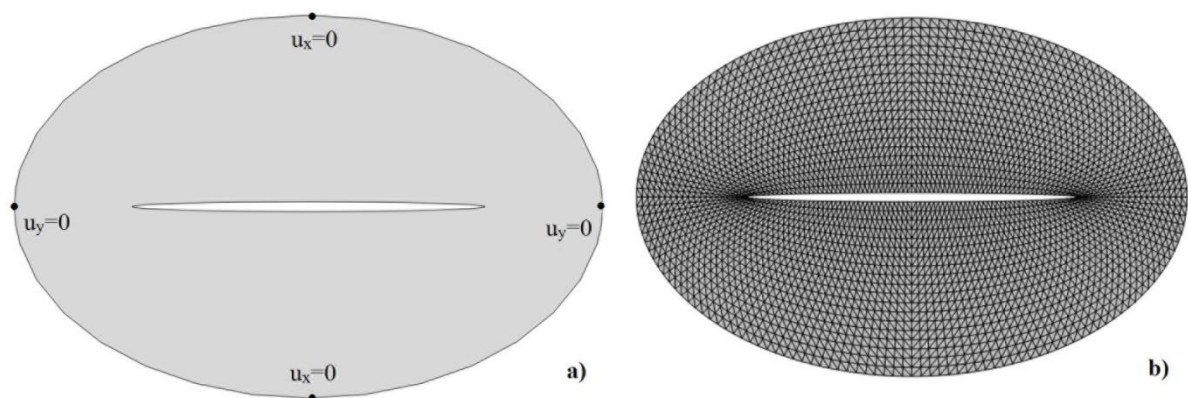
Figure 51 Model of a section of urethral duct. Geometrical model of the urethra transversal (a).

Two dimensional model showing the assumed boundary conditions.

Finite element discretization, transversal section (b).

The model is composed by 3120 nodes and 5928 elements, with dimension of 0.2.

Null displacement conditions are imposed on four diametrically opposite nodes along single directions, on the outer boundary of the model (Figure 51b), in order to provide minimal constraints.

In this model is considered the dilation of the duct in addition to internal pressure; in particular, the following values of internal pressure are considered: 0.085 kPa, 0.18 kPa, 0.49 kPa, 0.89 kPa, 1.3 kPa, 1.7 kPa and 2.1 kPa, that correspond respectively to 0.85 cmH_2O, 1.8 cmH_2O, 4.9 cmH_2O, 8.9 cmH_2O, 13 cmH_2O, 17 cmH_2O and 21 cmH_2O (Figure 52).
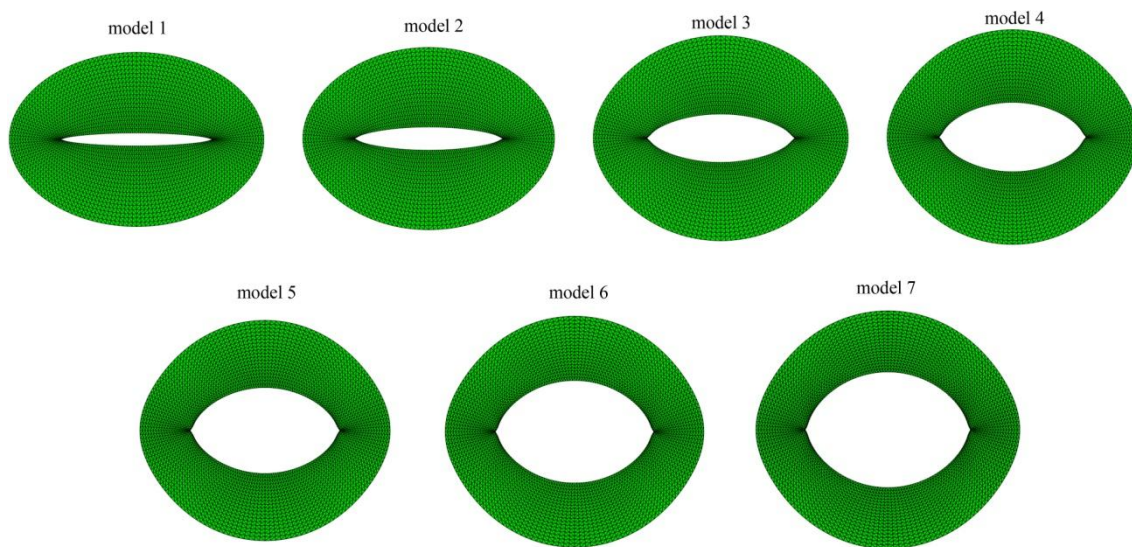
Figure 52 Different seven models showing different intraluminal pressure. Model 1 is realized with internal pressure of 0.085 kPa, model 2 with 0.18 kPa, model 3 with 0.49 kPa, model 4 with 0.89 kPa, model 5 with 1.3 kPa, model 6 with 1.7 kPa and model 7 with 2.1 kPa.

Considering different configurations of mechanical model, for every internal pressure value is realized a fluid model (CFD model) which is the corresponding flow of urine into the urethral duct (Figure 53).
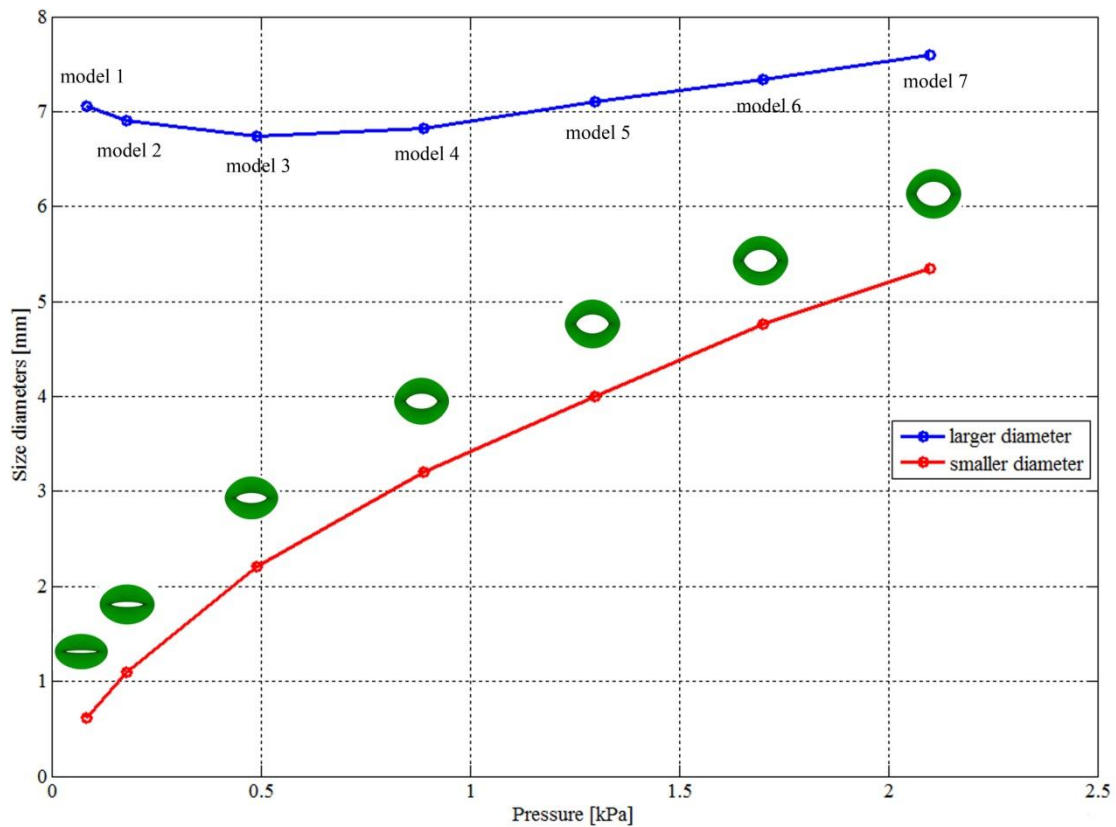
Figure 53 Different size diameters with corresponding pressure and ellipse.

The general settings of these models are here reported.

The model consists in an elliptical tube with two handles (infrapubic and prepubic angles) that represents urine flow.

To achieve a plausible model, urine properties are set as reality, density at 1.03 g/cm^3 and viscosity at 8.016 Pa·s.

The geometrical model of the urine flow is imported into the finite element preprocessing software Abaqus/CAE 6.14 (Dassault Systèmes Simulia Corp., Providence, RI).

To mesh the flow, tetrahedral elements with uniform dimensions are adopted, excluding the first model where hexahedral elements are used; denser mesh at the top and the bottom surfaces and larger mesh on the wall.

As boundary condition, on the wall is imposed fluid wall condition; on the top surface is imposed different values of pressure depending on geometrical dimensions while on the bottom surface zero pressure is imposed (Figure 54).
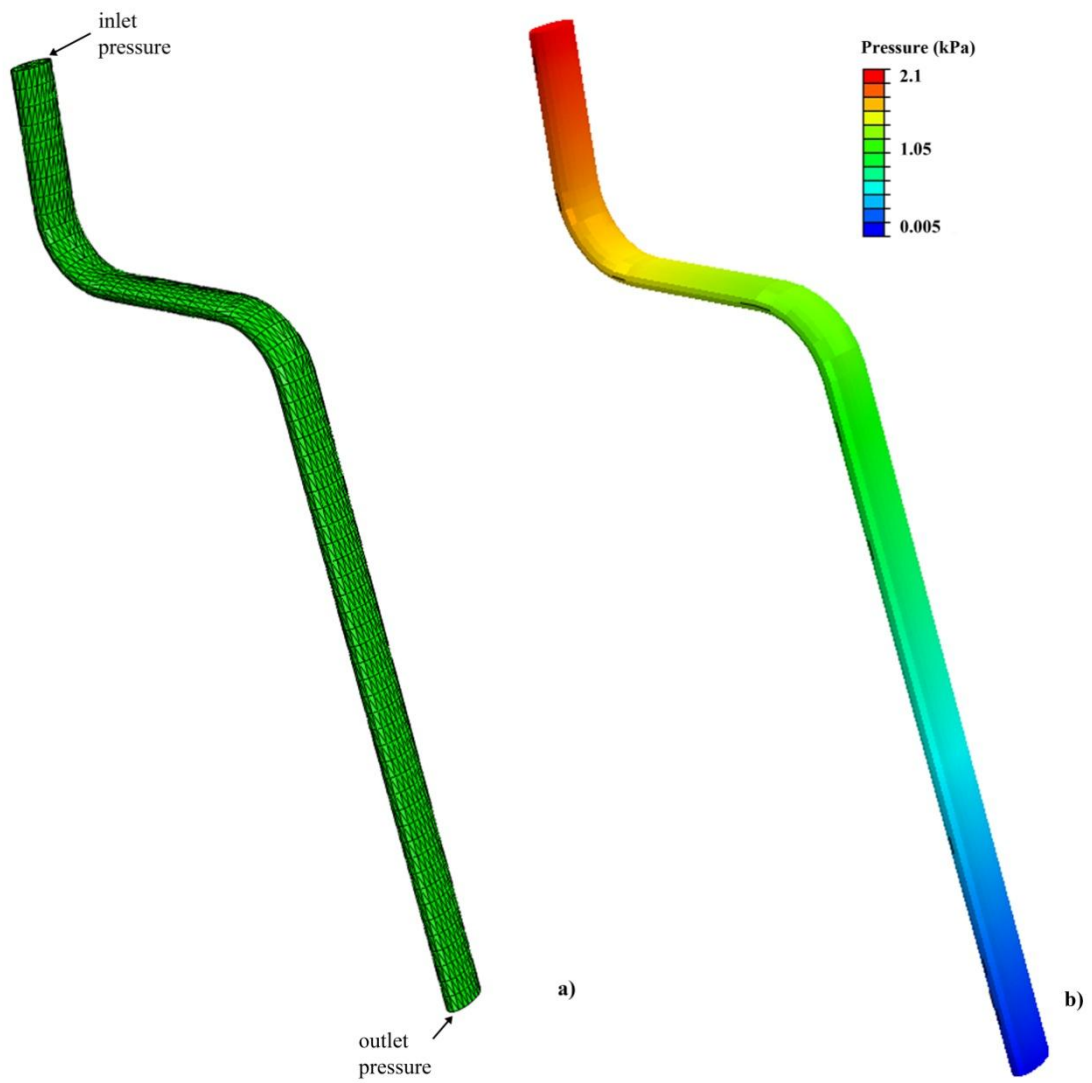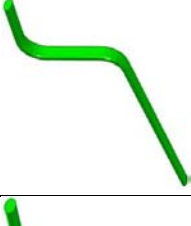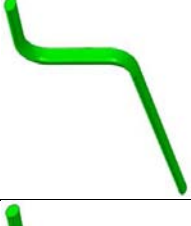
Figure 54 Geometrical model of the urine flow a). In the figure are represented inlet pressure and outlet pressure. In figure b) is shown pressure distribution.

Flow velocity in the elliptic tube shows a parabolic trend as shown in Figure 55.
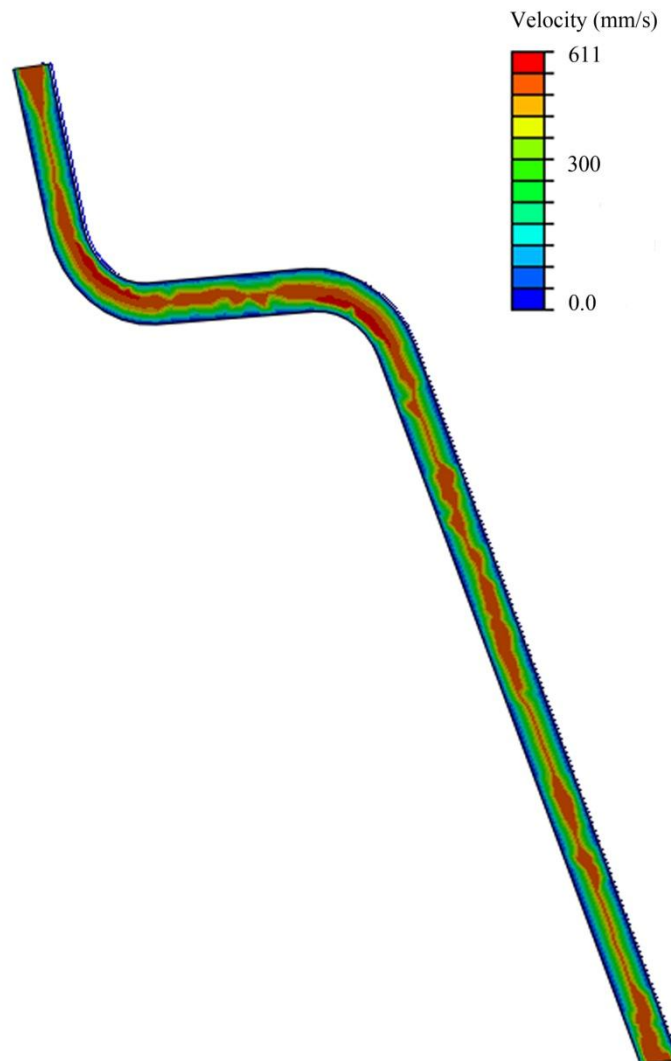
Figure 55 Distribution of flow velocity along the tube.

In the following there is a summary table of the CFD models with corresponding values of pressure, area and number of elements (Table 3).

	Pressure (kPa)	Area (mm^2)	Number of elements
	0.085	3.381	48208
	0.18	5.958	64210
	0.49	11.693	16687
	0.89	17.132	5962
	1.3	22.294	15566
	1.7	27.426	8259
	2.1	31.918	7830

Table 3 Summary of CFD models and corresponding values of pressure, area and number of elements.

4.1 Model 1

The smallest configuration considered represents the initial situation of mechanical model that is the case with minimal inlet pressure as 0.085 kPa. The dimensions of the diameters of this configuration are 7.06 mm and 0.61 mm, horizontal and vertical size respectively.

The model is composed by 13860 hexahedral elements and 20584 nodes; eight nodes are used to mesh this model, with size of 0.2 at the top and bottom surfaces and a size 2 along the wall (Figure 56).
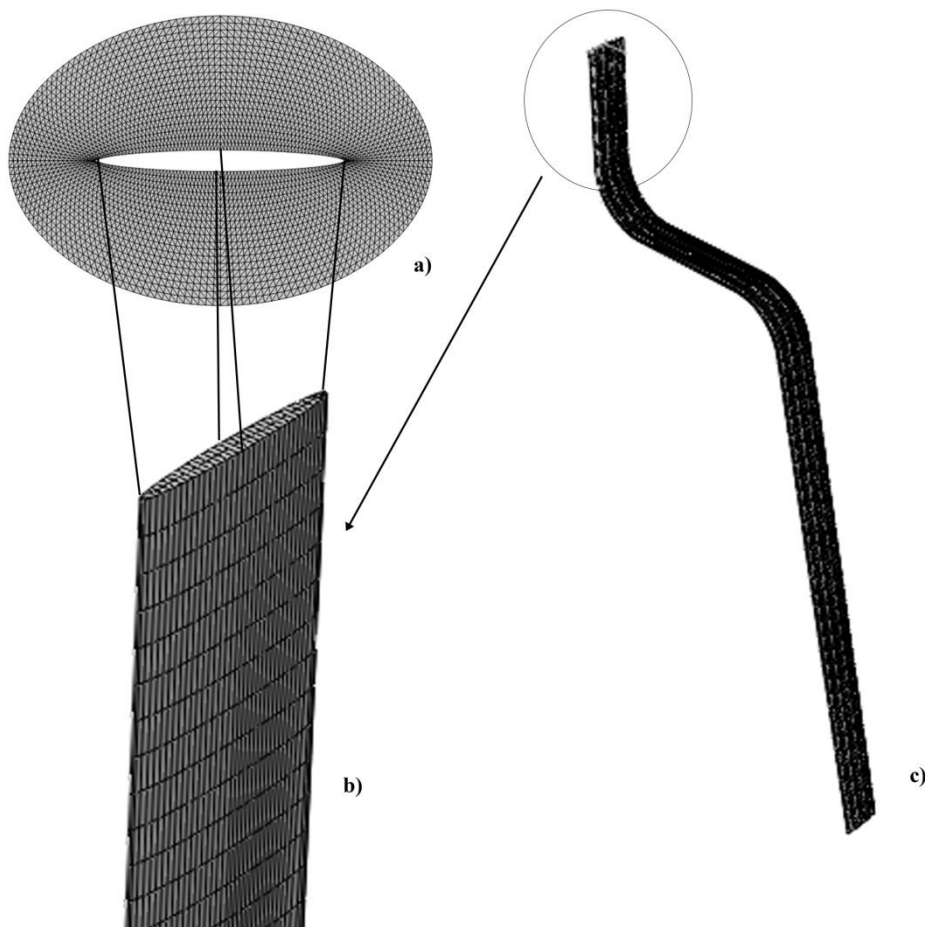
Figure 56 Geometrical section of urethral duct (a). Enlargement of corresponding urine flow (b). Complete corresponding urine flow (c).

Flow velocity in the elliptic tube shows a parabolic trend, so urine flow is calculated with the elliptic paraboloid formulation. The inlet pressure increas in the initial phase and reaches the final value at different times: 0.05 s, 0.1 s and 0.2 s of 0.5 s.

From the analysis results that outlet pressure reaches the same value in all three cases (Figure 57). So, the value reached is independent from the pressure imposition time.
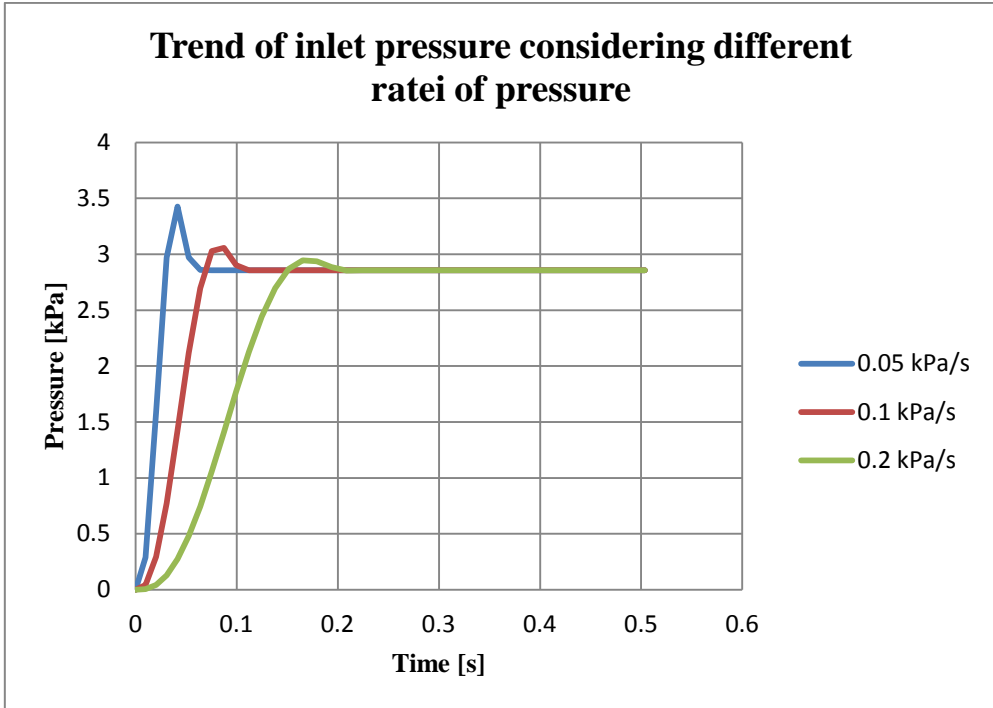
Figure 57 Trend of inlet pressure considering different ratei of pressure, 0.05 kPa/s, 0.1 kPa/s and 0.2 kPa/s.

Considering kinetic energy, it shows in fact that the value reached in all three cases is the same (Figure 58).
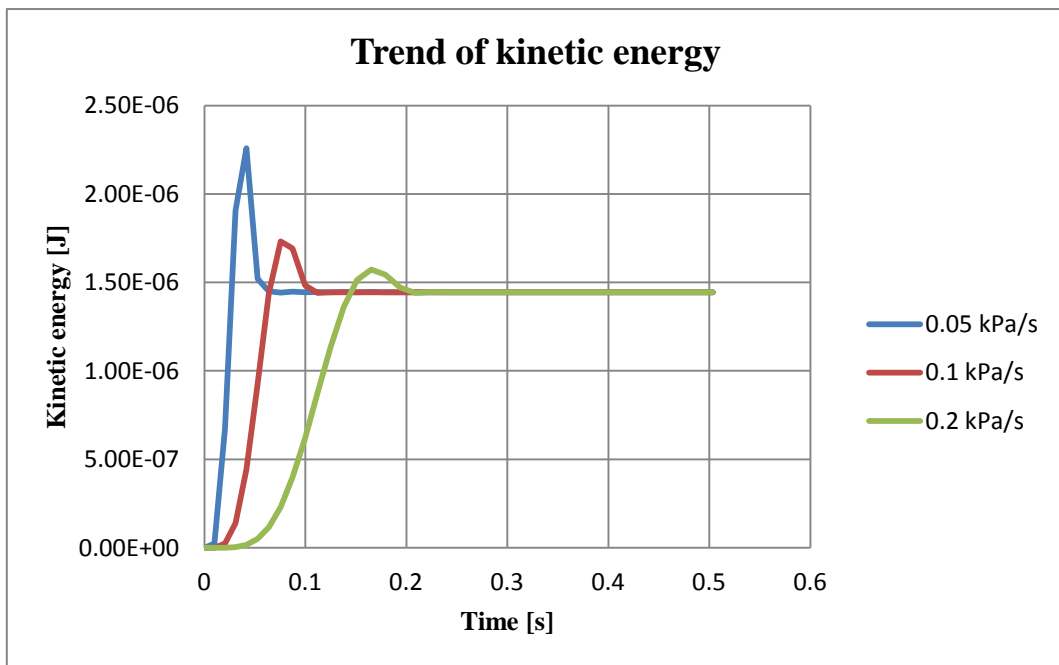
Figure 58 Trend of kinetic energy.

To adapt this model to reality the development of urine flow in time is also calculated (Figure 59).
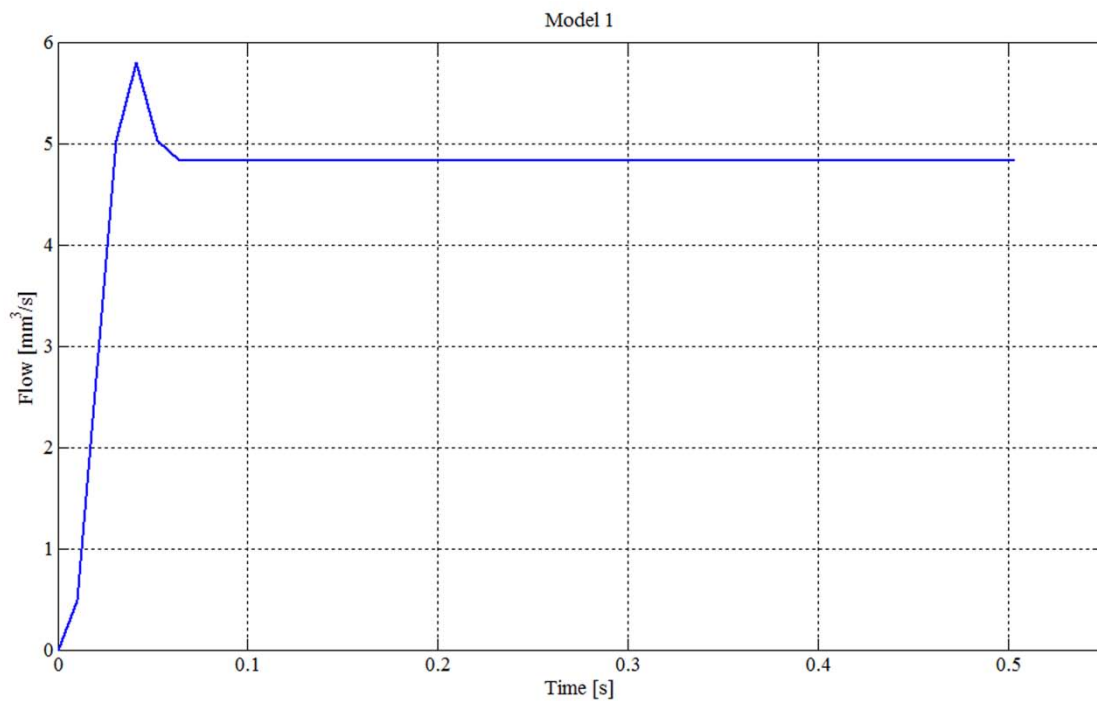
Figure 59 Graphic urine flow-time.

In the first phase urine flow shows a high increase up to stabilization value that results in 4.834 mm^3/s that corresponds about to 0.005 cm^3/s.

4.2 Model 2

The second configuration considered represents the case with inlet pressure at 0.18 kPa. The dimensions of the diameters of this configuration are 6.9 mm and 1.1 mm, horizontal and vertical size respectively.

The model is composed by 64210 elements and 16214 nodes; four nodes are used to mesh this model, with size of 0.2 at the top and bottom surfaces and size 1 along the wall (Figure 60).
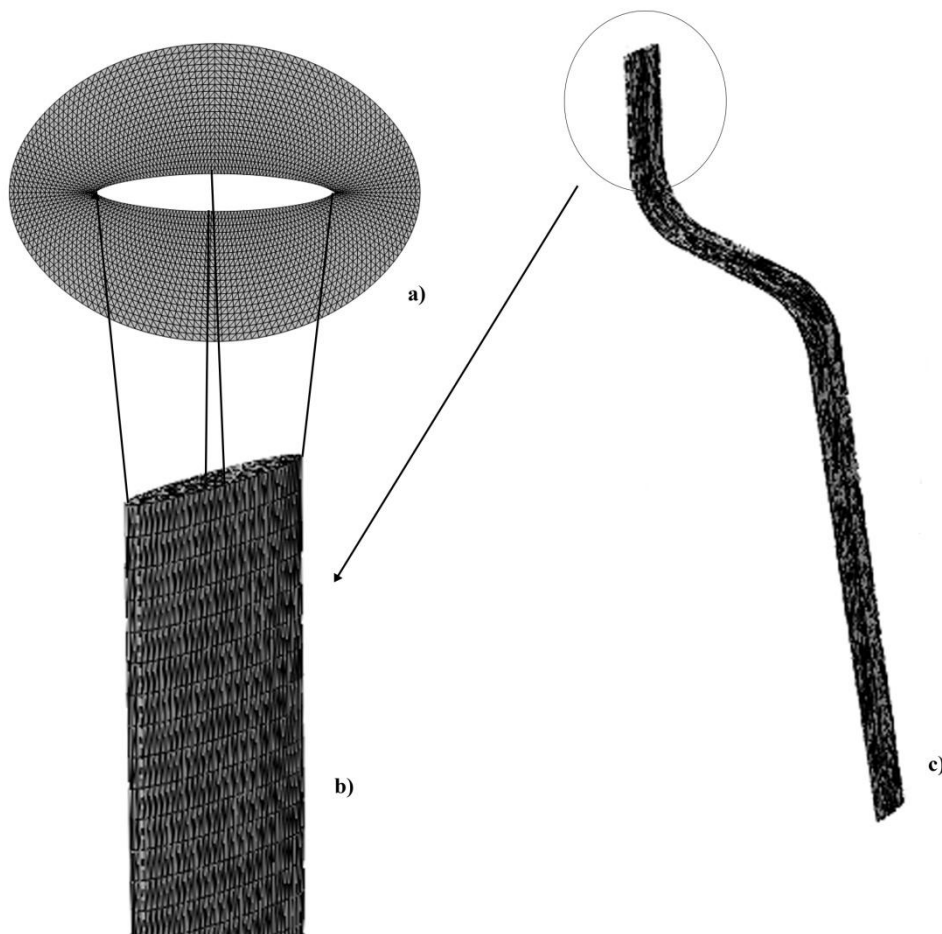
Figure 60 Geometrical section of urethral duct (a). Enlargement of corresponding urine flow (b). Complete corresponding urine flow (c).

Flow velocity in the elliptic tube shows a parabolic trend, so urine flow is calculated with the elliptic paraboloid formulation. The inlet pressure increas in the initial phase and reaches the final value at different times: 0.05 s, 0.1 s and 0.2 s of 0.5 s.

From the analysis results that outlet pressure reaches the same value in all three cases (Figure 61). So, the value reached is independent from the pressure imposition time.
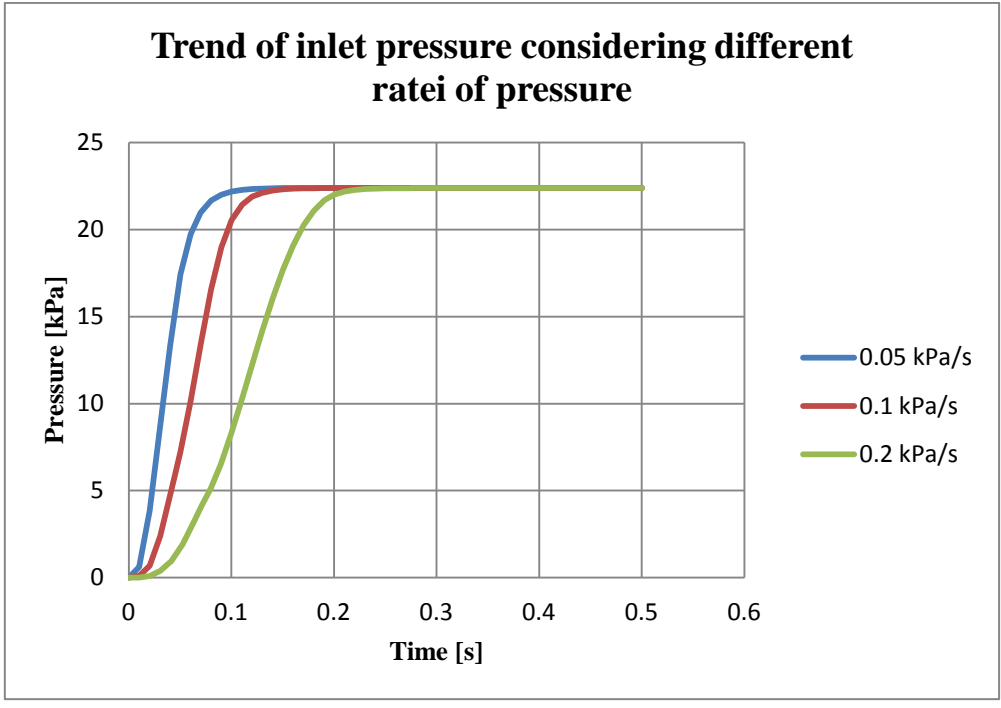
Figure 61 Trend of inlet pressure considering different ratei of pressure, 0.05 kPa/s, 0.1 kPa/s and 0.2 kPa/s.

Considering kinetic energy, it shows in fact that the value reached in all three cases is the same (Figure 62).
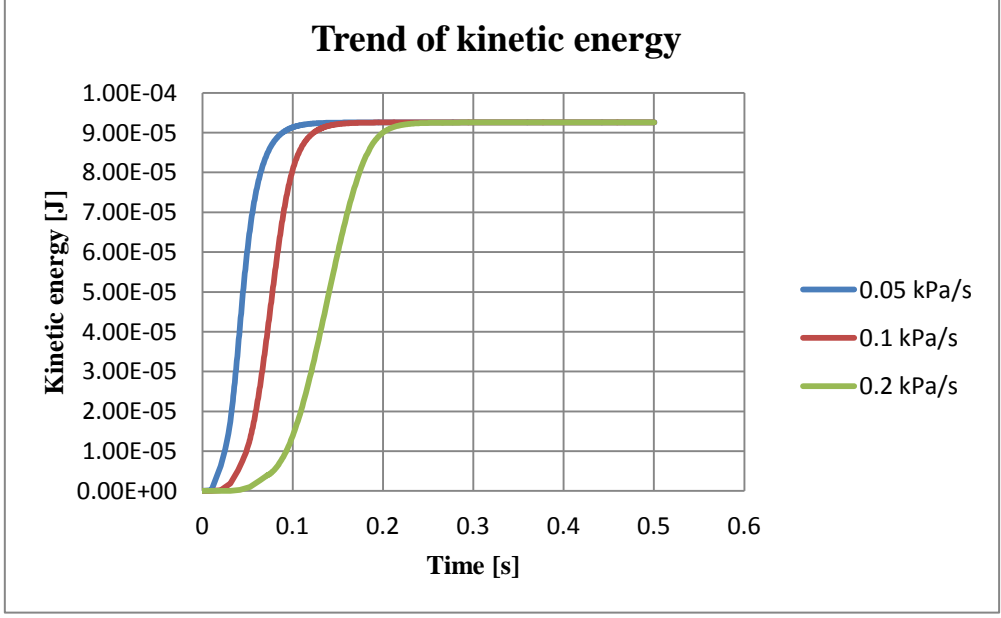
Figure 62 Trend of kinetic energy.

To adapt this model to reality the development of urine flow in time is also calculated (Figure 63).
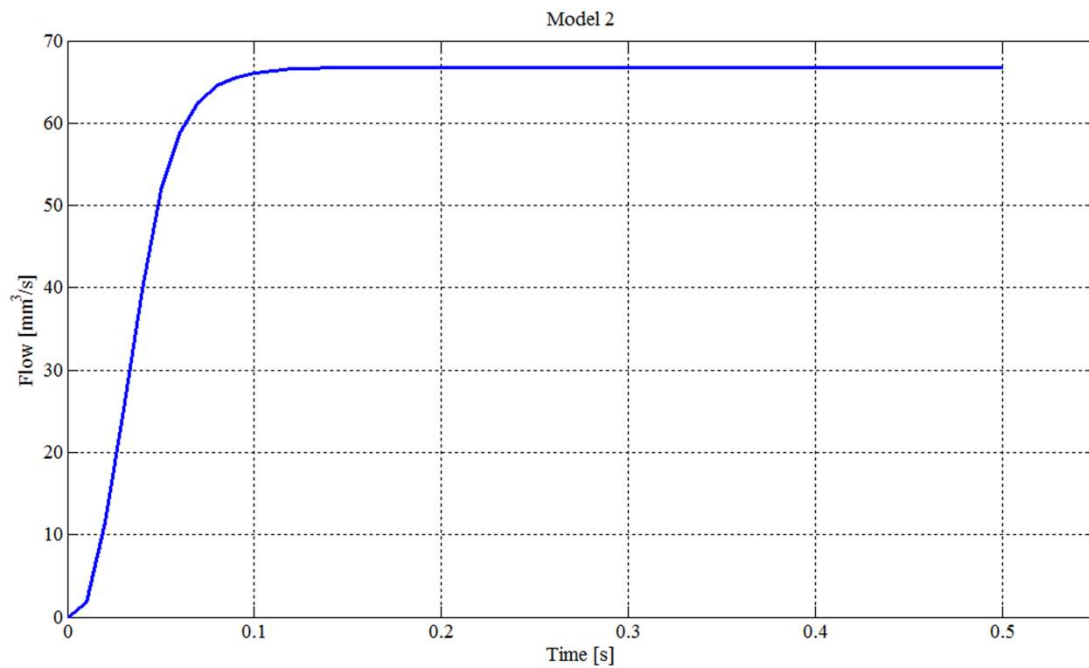
Figure 63 Graphic urine flow-time.

In the first phase urine flow shows a high increase up to stabilization value that results in 66.73 mm^3/s that corresponds to about 0.067 cm^3/s.

4.3 Model 3

The third configuration considered represents the case with inlet pressure at 0.49 kPa. The dimensions of the diameters in this configuration are 6.74 mm and 2.21 mm, horizontal and vertical size respectively.

The model is composed by 16687 elements and 4398 nodes; four nodes are used to mesh this model, with size 0.4 at the top and bottom surfaces and size 2 along the wall (Figure 64).
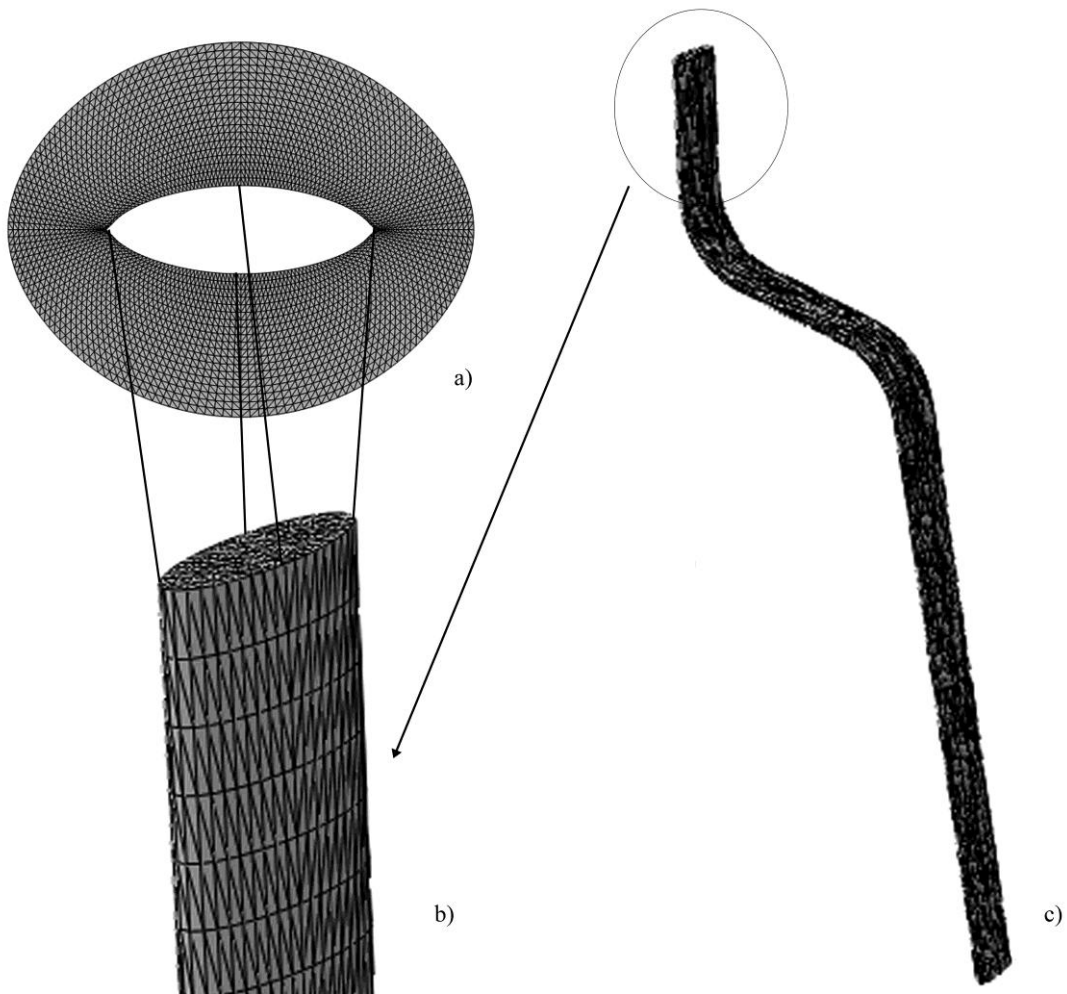
Figure 64 Geometrical section of urethral duct (a). Enlargement of corresponding urine flow (b). Complete corresponding urine flow (c).

Flow velocity in the elliptic tube shows a parabolic trend, so urine flow is calculated with the elliptic paraboloid formulation. The inlet pressure increas in the initial phase and reaches the final value at different times: 0.05 s, 0.1 s and 0.2 s of 0.5 s.

From the analysis results that outlet pressure reaches the same value in all three cases (Figure 65). So, the value reached is independent from the pressure imposition time.
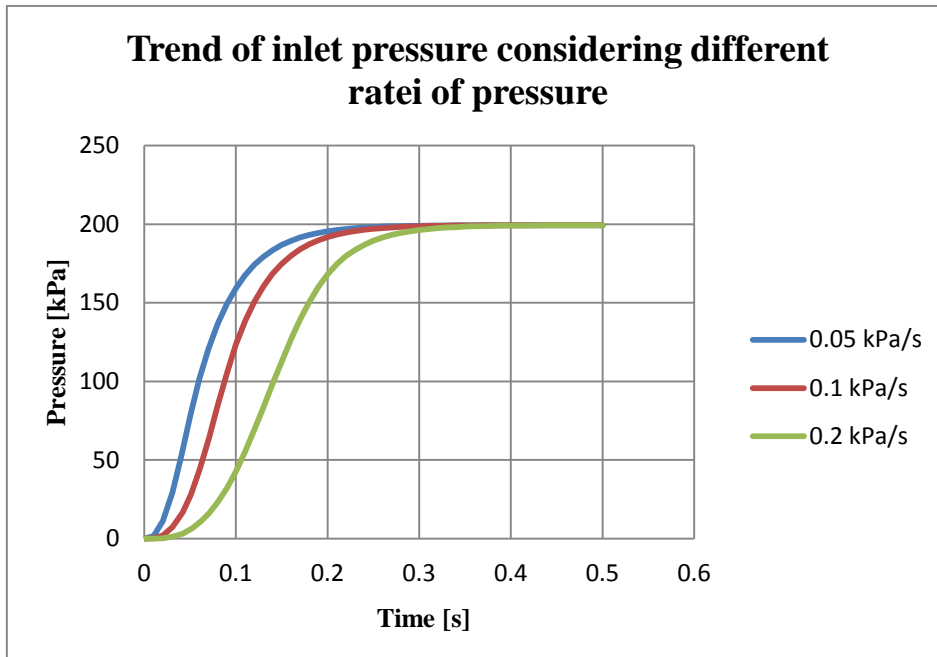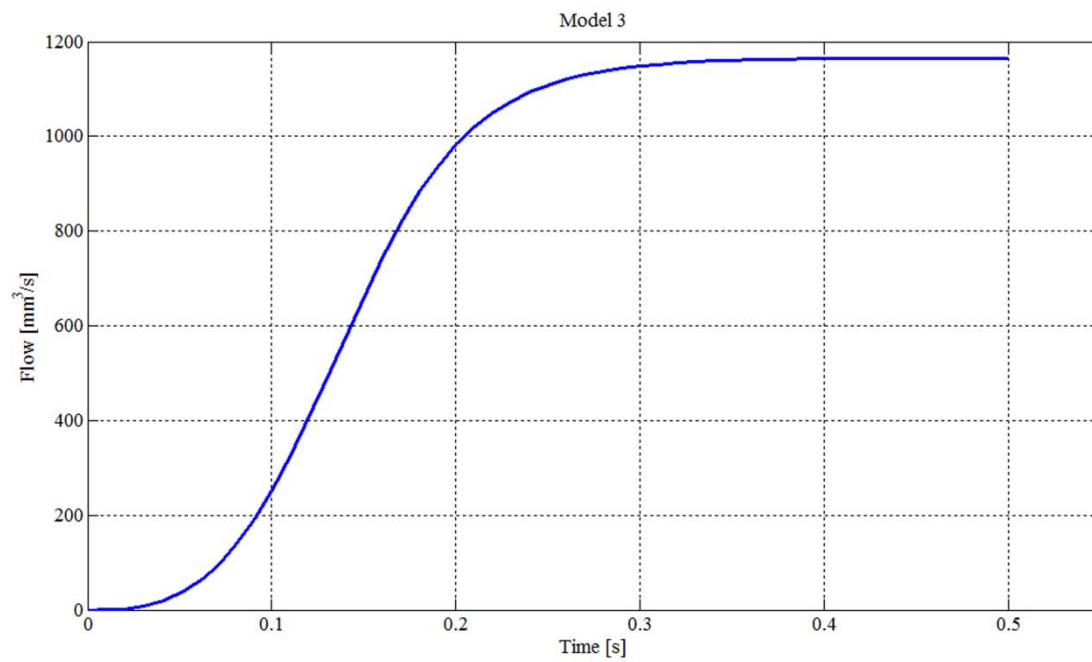
Figure 65 Trend of inlet pressure considering different ratei of pressure, 0.05 kPa/s, 0.1 kPa/s
and 0.2 kPa/s.

Considering kinetic energy, it shows in fact that the value reached in all three cases is
the same (Figure 66).
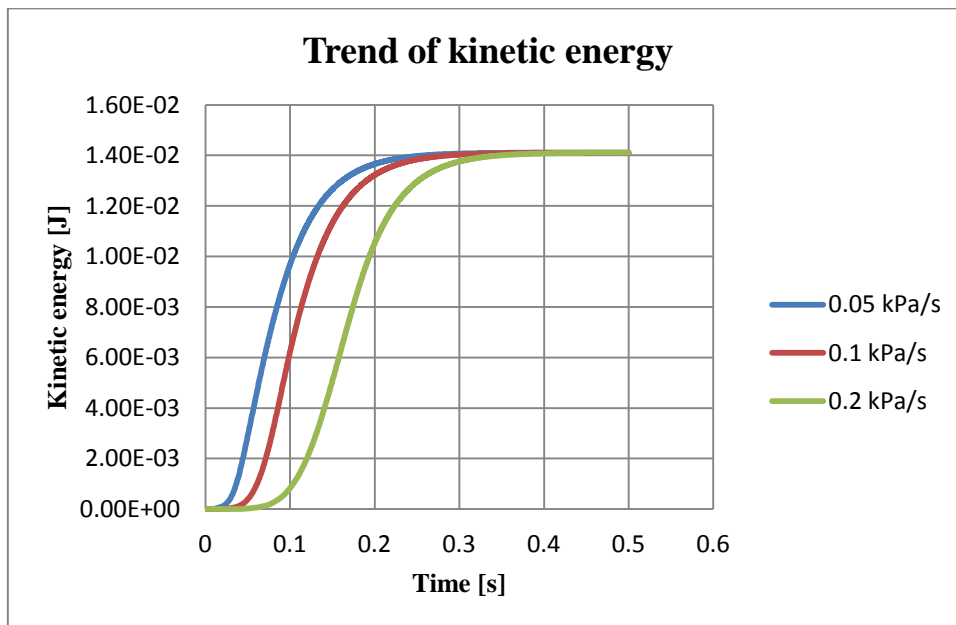
Figure 66 Trend of kinetic energy.

To adapt this model to reality the development of urine flow in time is also calculated (Figure 67).


Figure 67 Graphic urine flow-time.

In the first phase urine flow shows a high increase up to stabilization value that results in 1166 mm^3/s that corresponds to 1.166 cm^3/s.

4.4 Model 4

The fourth configuration considered represents the case with inlet pressure at 0.89 kPa. The dimensions of the diameters of this configuration are 6.82 mm and 3.2 mm, horizontal and vertical size respectively.

The model is composed by 5962 elements and 1732 nodes; four nodes are used to mesh this model, with size 0.8 at the top and bottom surfaces and size 2.5 along the wall (Figure 68).
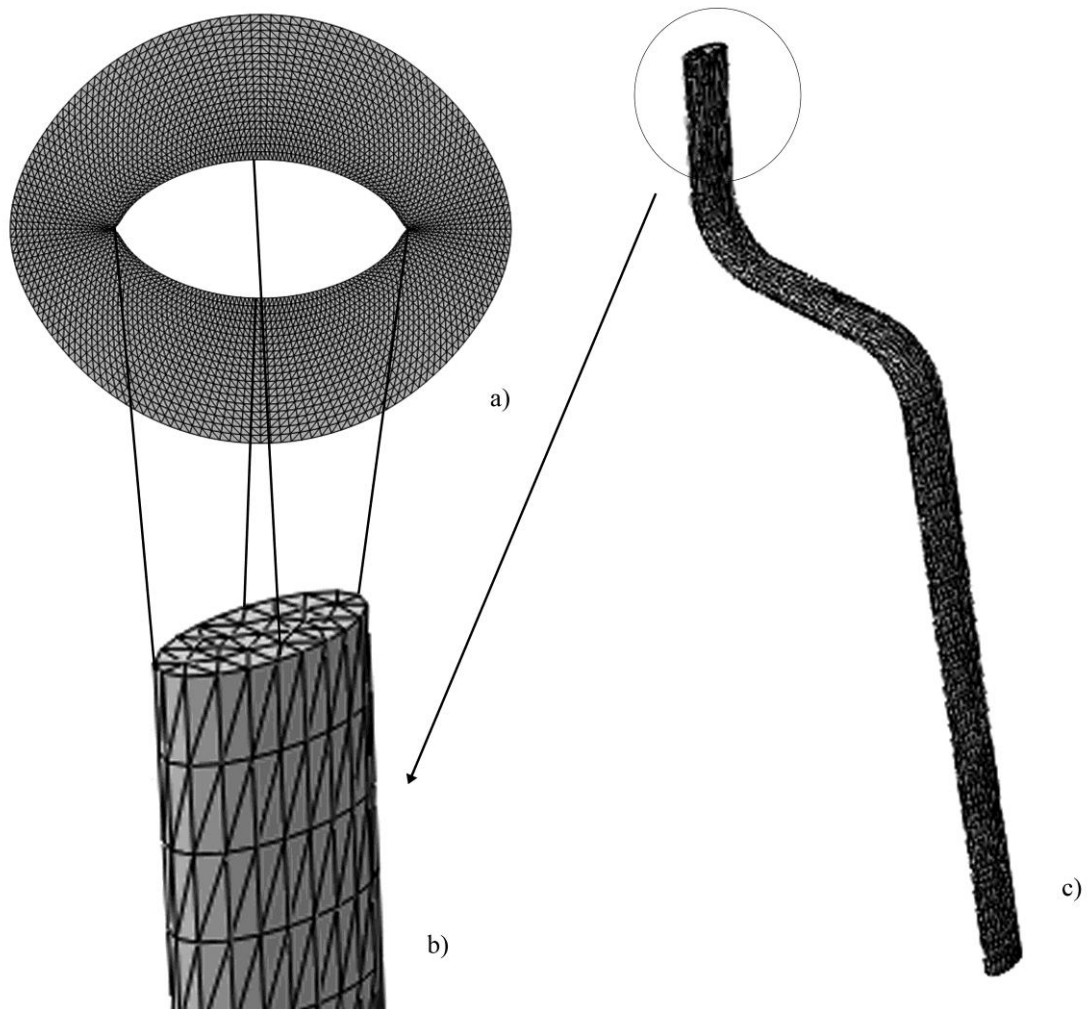
Figure 68 Geometrical section of urethral duct (a). Enlargement of corresponding urine flow (b). Complete corresponding urine flow (c).

Flow velocity in the elliptic tube shows a parabolic trend, so urine flow is calculated with the elliptic paraboloid formulation. The inlet pressure increas in the initial phase and reaches the final value at different times: 0.05 s, 0.1 s and 0.2 s of 0.5 s.

From the analysis results that outlet pressure reaches the same value in all three cases (Figure 69). So, the value reached is independent from the pressure imposition time.
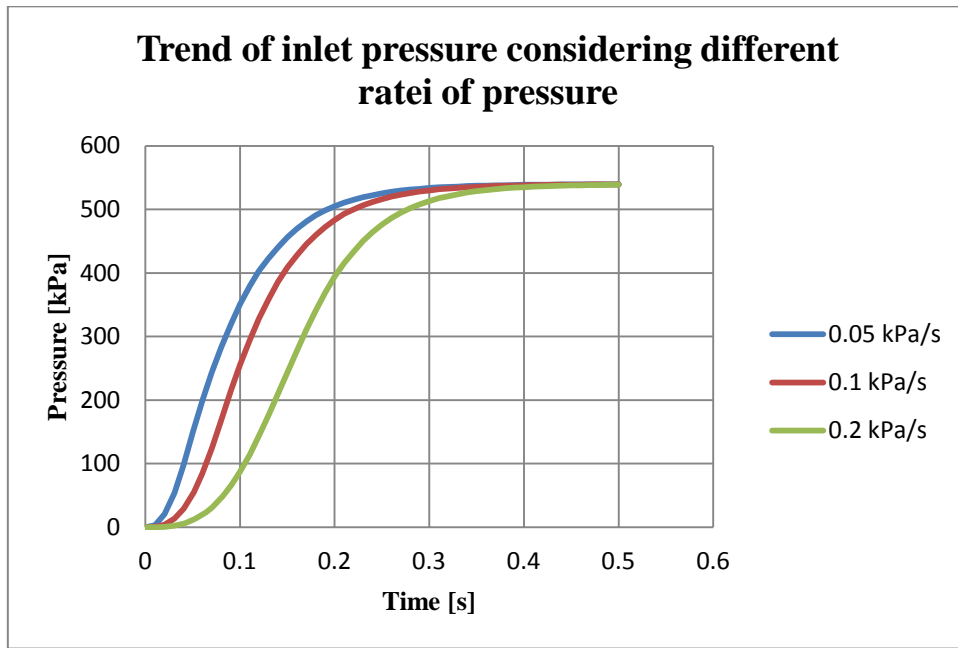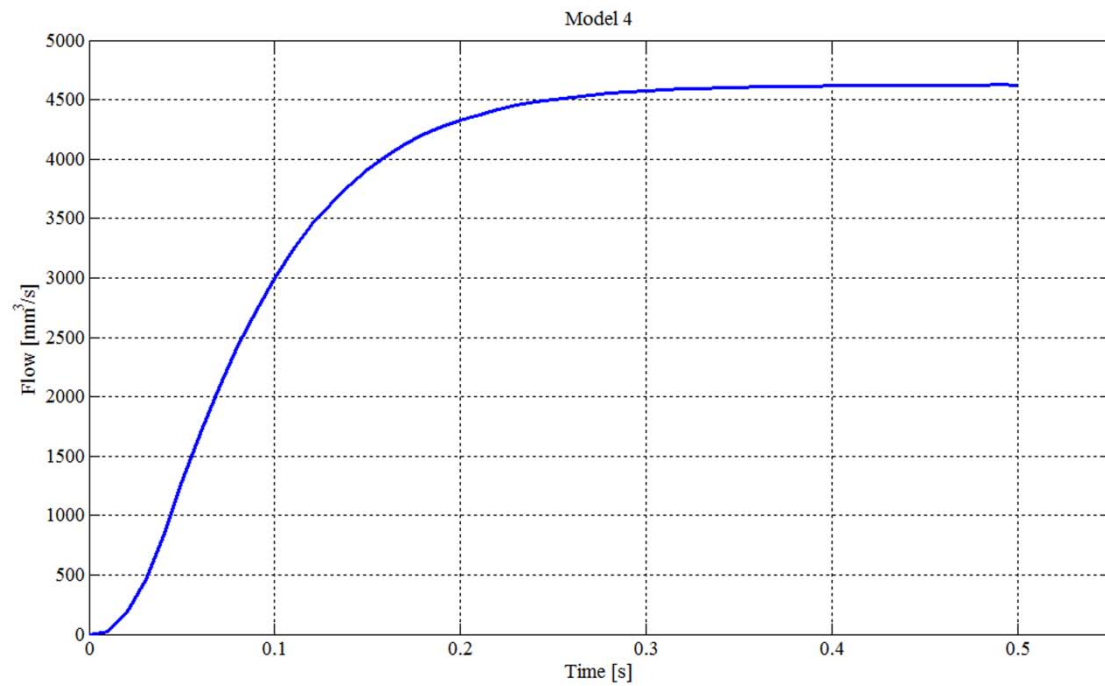

Figure 69 Trend of inlet pressure considering different ratei of pressure, 0.05 kPa/s, 0.1 kPa/s and 0.2 kPa/s.

Considering kinetic energy, it shows in fact that the value reached in all three cases is the same (Figure 70).
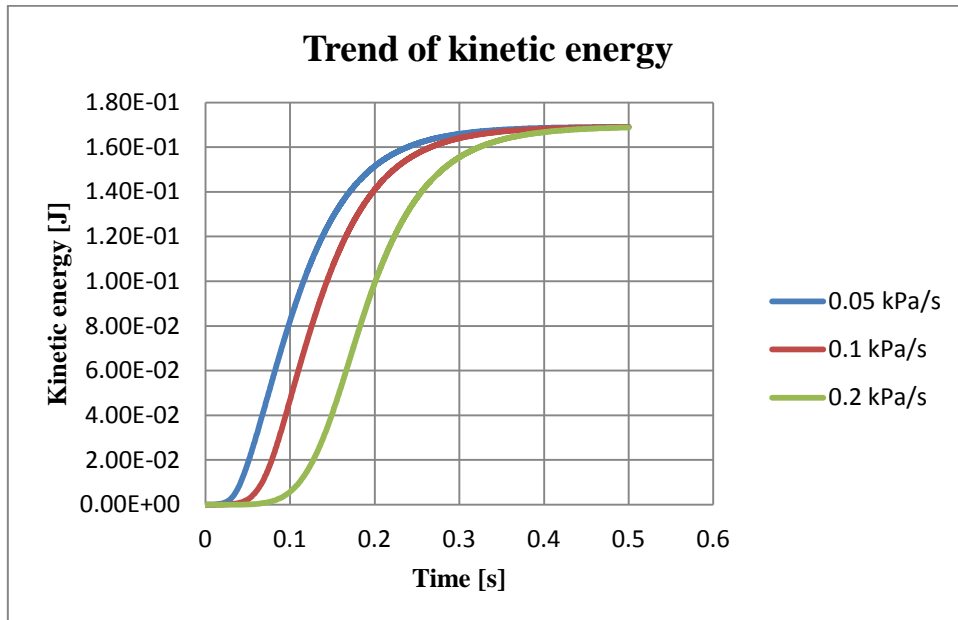
Figure 70 Trend of kinetic energy.

To adapt this model to reality the development of urine flow in time is also calculated (Figure 71).

**Figure 71** Graphic urine flow-time.

In the first phase urine flow shows a high increase up to stabilization value that results in 4623 mm^3/s that corresponds to 4.623 cm^3/s.

4.5 Model 5

The fifth configuration considered represents the case with inlet pressure at 1.3 kPa.

The dimensions of the diameters of this configuration are 7.1 mm and 4 mm, horizontal and vertical size respectively.

The model is composed by 15566 elements and 4236 nodes; four nodes are used to mesh this model, with size 0.5 at the top and bottom surfaces and size 2 along the wall (Figure 72).
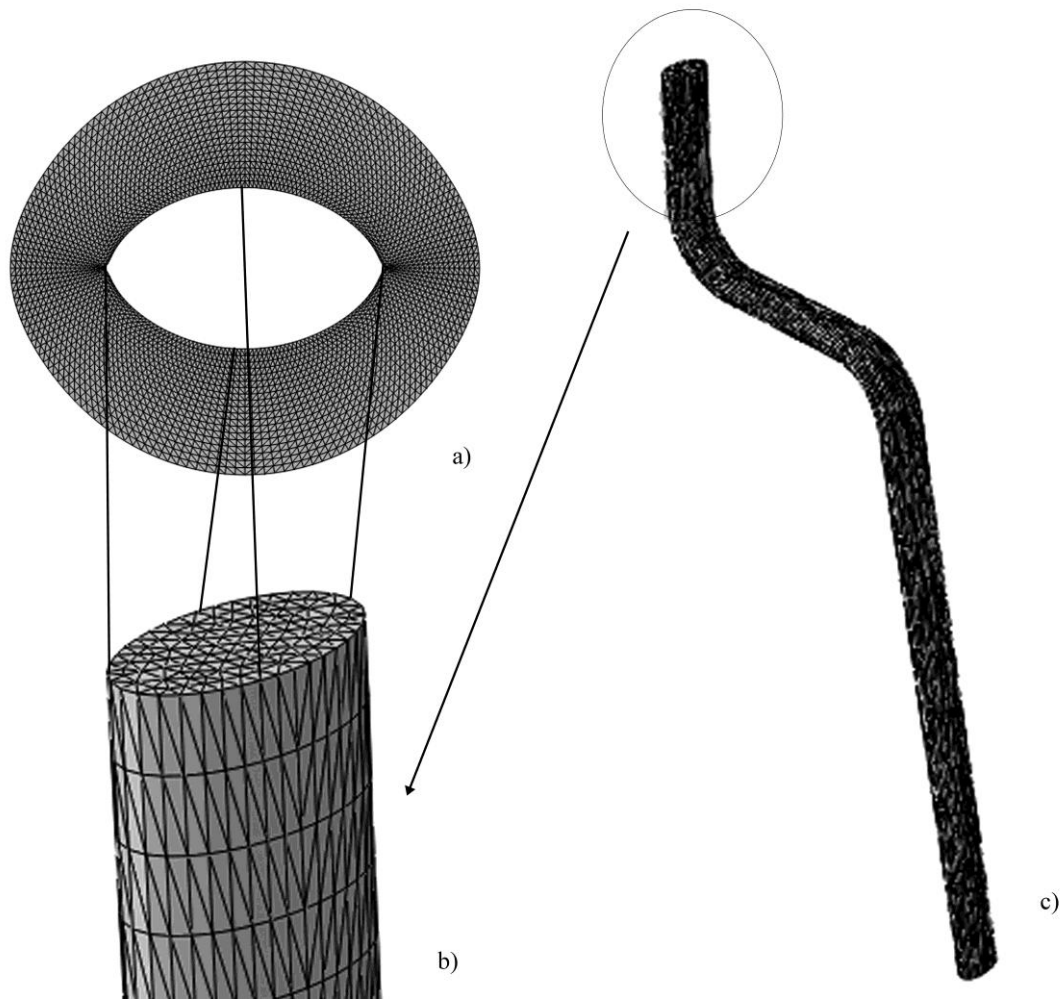

Figure 72 Geometrical section of urethral duct (a). Enlargement of corresponding urine flow (b). Complete corresponding urine flow (c).

Flow velocity in the elliptic tube shows a parabolic trend, so urine flow is calculated with the elliptic paraboloid formulation. The inlet pressure increas in the initial phase and reaches the final value at different times: 0.05 s, 0.1 s and 0.2 s of 0.5 s.

From the analysis results that outlet pressure reaches the same value in all three cases (Figure 73). So, the value reached is independent from the pressure imposition time.
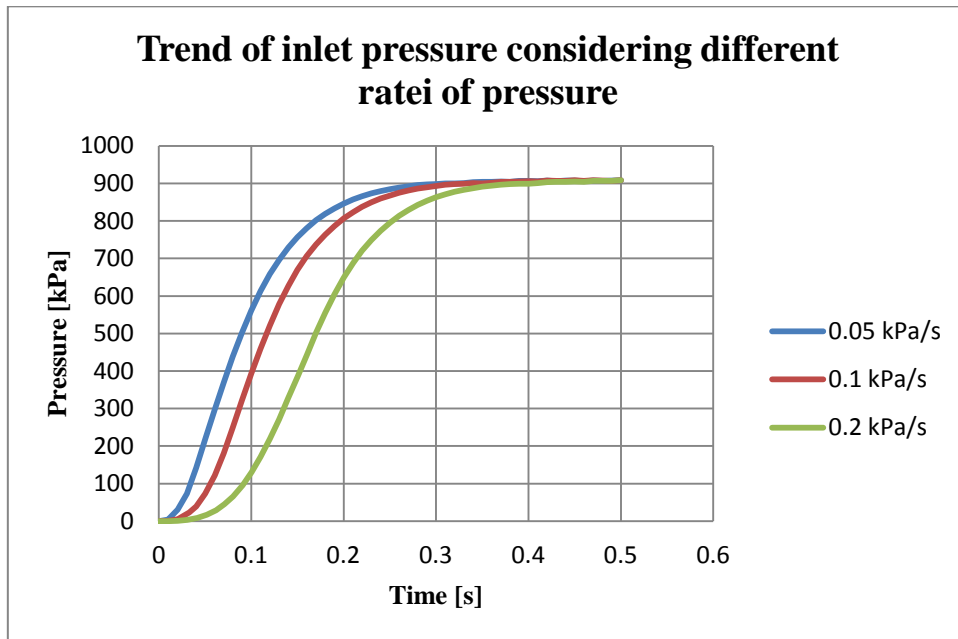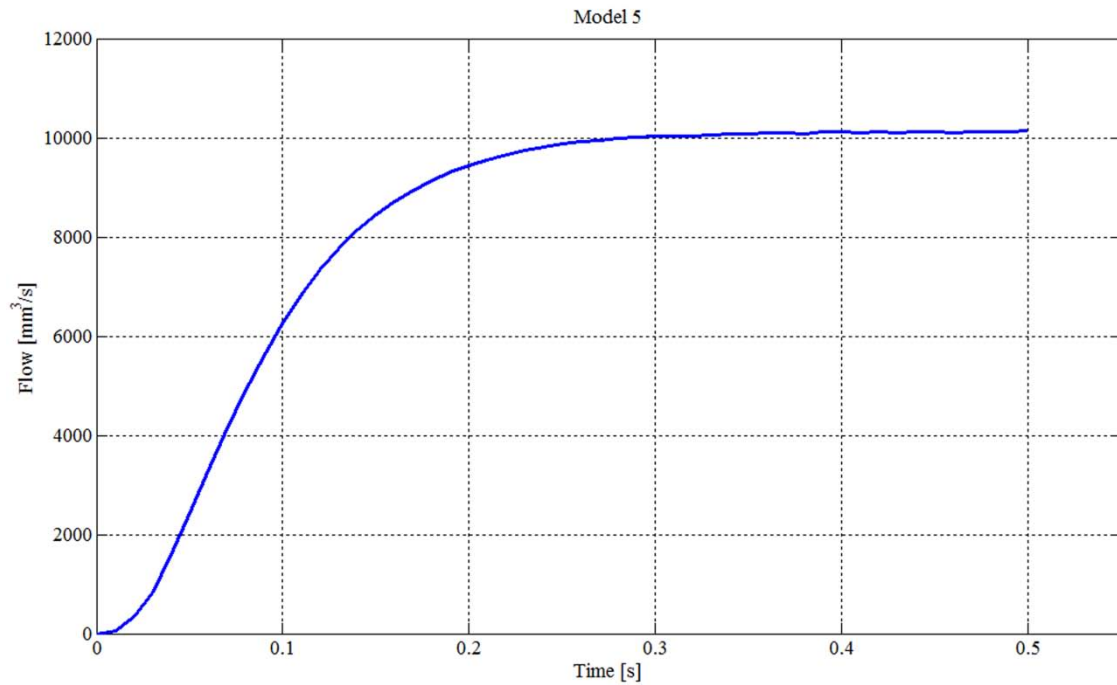

Figure 73 Trend of inlet pressure considering different ratei of pressure, 0.05 kPa/s, 0.1 kPa/s and 0.2 kPa/s.

Considering kinetic energy, it shows in fact that the value reached in all three cases is the same (Figure 74).
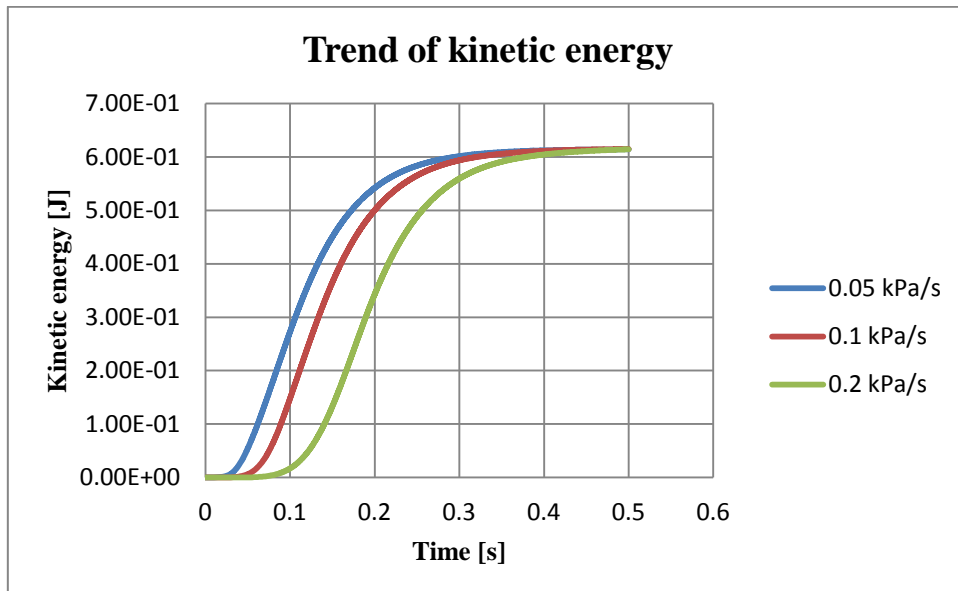
Figure 74 Trend of kinetic energy.

To adapt this model to reality the development of urine flow in time is also calculated (Figure 75).


Figure 75 Graphic urine flow-time.

In the first phase urine flow shows a high increase up to stabilization value that results in 10120 mm^3/s that corresponds to 10.12 cm^3/s.

4.6 Model 6

The sixth configuration considered represents the case with inlet pressure as 1.7 kPa. The dimensions of the diameters of this configuration are 7.34 mm and 4.76 mm, horizontal and vertical size respectively.

The model is composed by 8259 elements and 2286 nodes; four nodes are used to mesh this model, with size 0.8 at the top and bottom surfaces and size 2.5 along the wall (Figure 76).
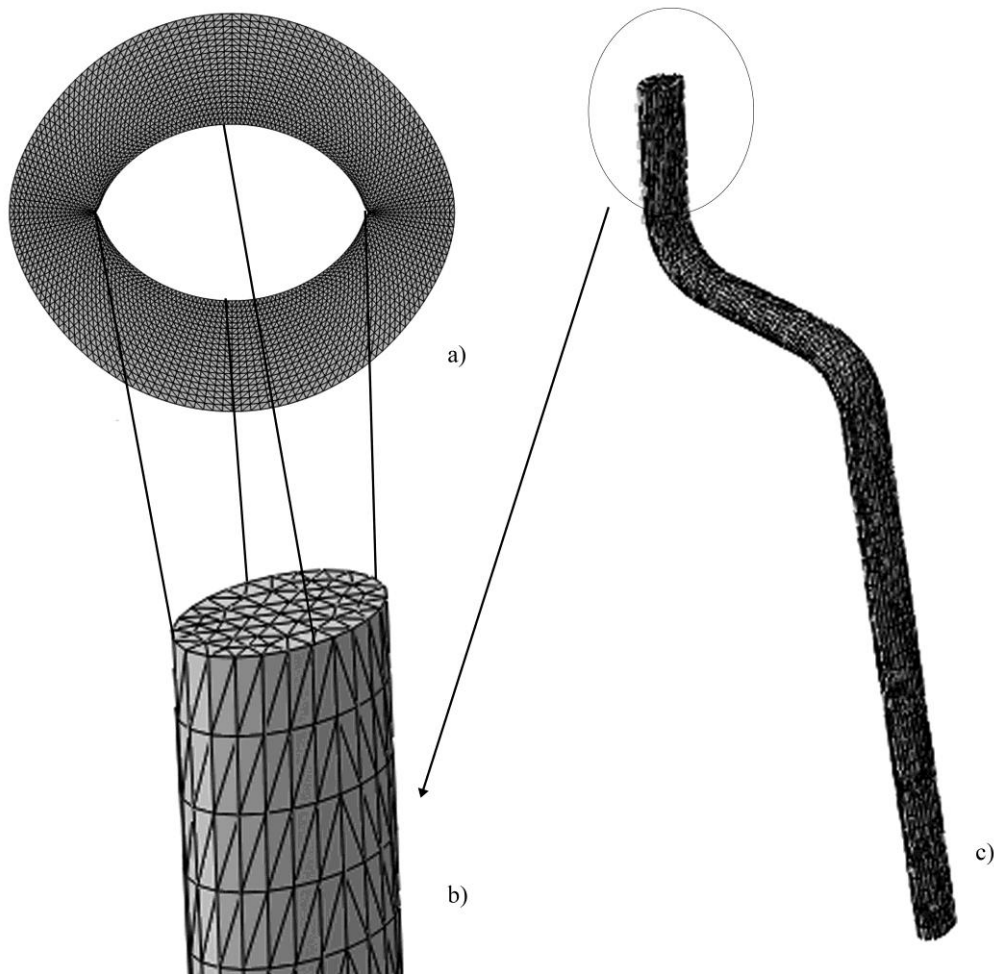

Figure 76 Geometrical section of urethral duct (a). Enlargement of corresponding urine flow (b). Complete corresponding urine flow (c).

In this model is considered also the turbulence; different settings are imposed in the model simulation in Abaqus/CAE 6.14 (Dassault Systèmes Simulia Corp., Providence, RI) but the result is similar to that obtained without turbulence.

Flow velocity in the elliptic tube shows a parabolic trend, so urine flow is calculated with the elliptic paraboloid formulation. The inlet pressure increas in the initial phase and reaches the final value at different times: 0.05 s, 0.1 s and 0.2 s of 0.5 s.

From the analysis results that outlet pressure reaches the same value in all three cases (Figure 77). So, the value reached is independent from the pressure imposition time.
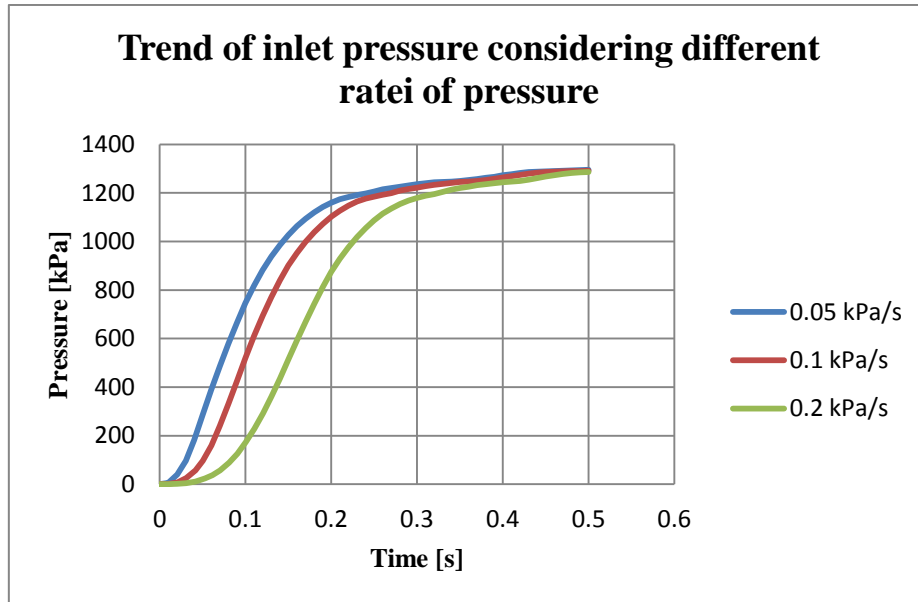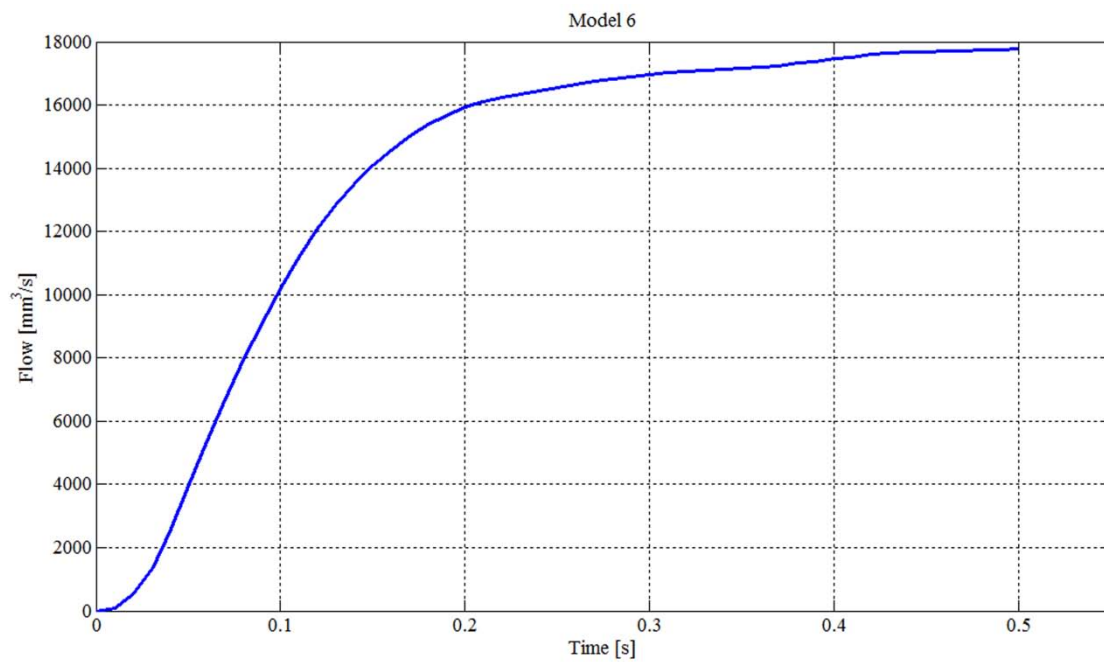

Figure 77 Trend of inlet pressure considering different ratei of pressure, 0.05 kPa/s, 0.1 kPa/s and 0.2 kPa/s.

Considering kinetic energy, it shows in fact that the value reached in all three cases is the same (Figure 78).
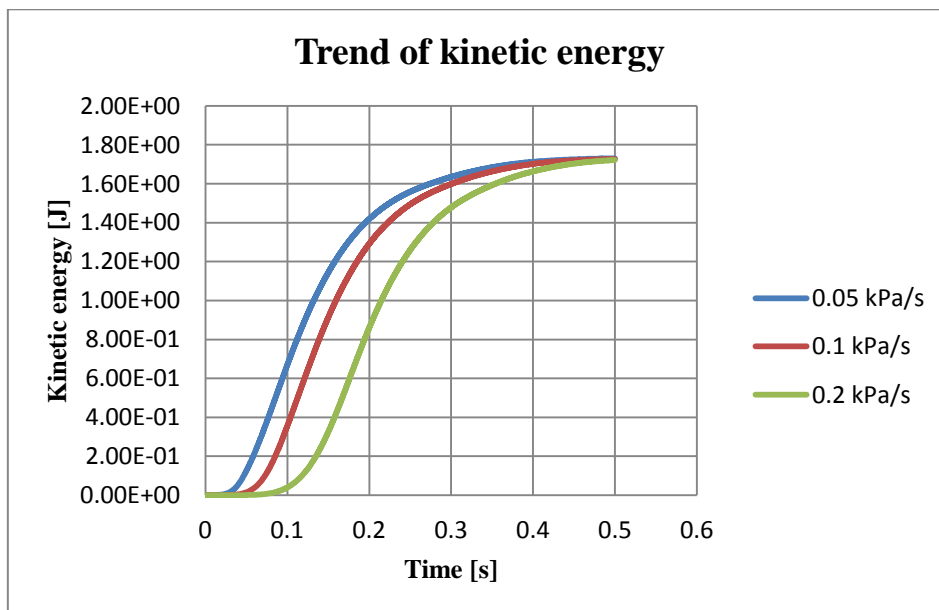
Figure 78 Trend of kinetic energy.

To adapt this model to reality the development of urine flow in time is also calculated (Figure 79).

Figure 79 Graphic urine flow-time.

In the first phase urine flow shows a high increase up to stabilization value that results in 17740 mm^3/s that corresponds to 17.74 cm^3/s.

4.7 Model 7

The last configuration considered represents the case with inlet pressure at 2.1 kPa.

The dimensions of the diameters of this configuration are 7.6 mm and 5.35 mm, horizontal and vertical respectively.

The model is composed by 7830 elements and 2258 nodes; four nodes are used to mesh this model, with size 0.8 at the top and bottom surfaces and size 2.5 along the wall (Figure 80).
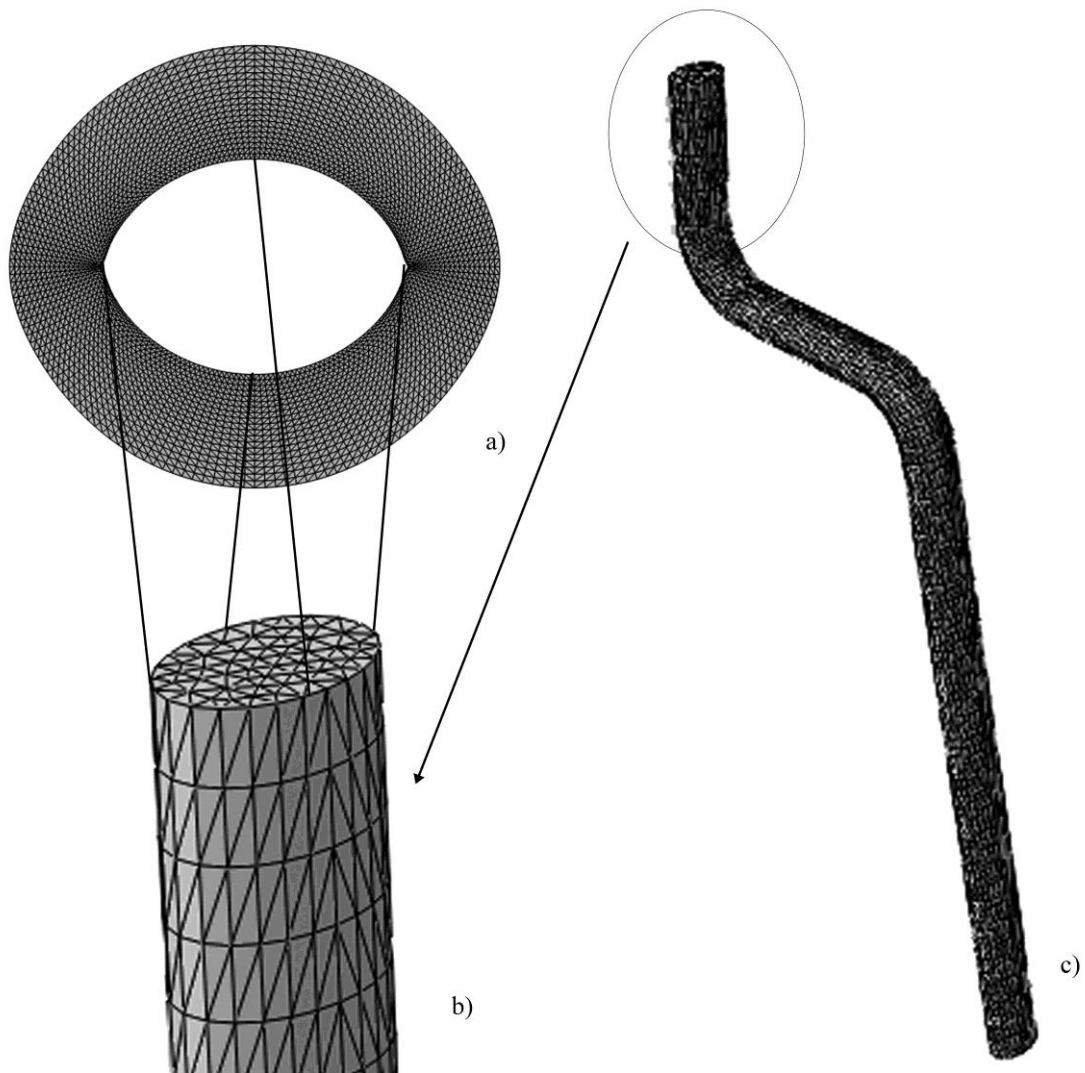

Figure 80 Geometrical section of urethral duct (a). Enlargement of corresponding urine flow (b). Complete corresponding urine flow (c).

Also in this model is considered the turbulence; different settings are imposed in the model simulation in Abaqus/CAE 6.14 (Dassault Systèmes Simulia Corp., Providence, RI) but the result is similar to that obtained without turbulence.

Flow velocity in the elliptic tube shows a parabolic trend, so urine flow is calculated with the elliptic paraboloid formulation. The inlet pressure increas in the initial phase and reaches the final value at different times: 0.05 s, 0.1 s and 0.2 s of 0.5 s.

From the analysis results that outlet pressure reaches the same value in all three cases (Figure 81). So, the value reached is independent from the pressure imposition time.
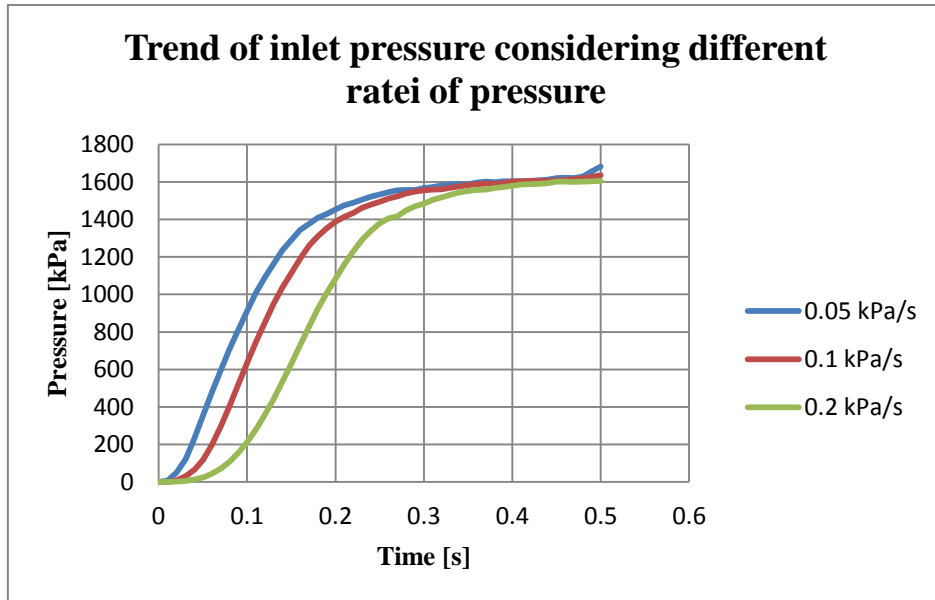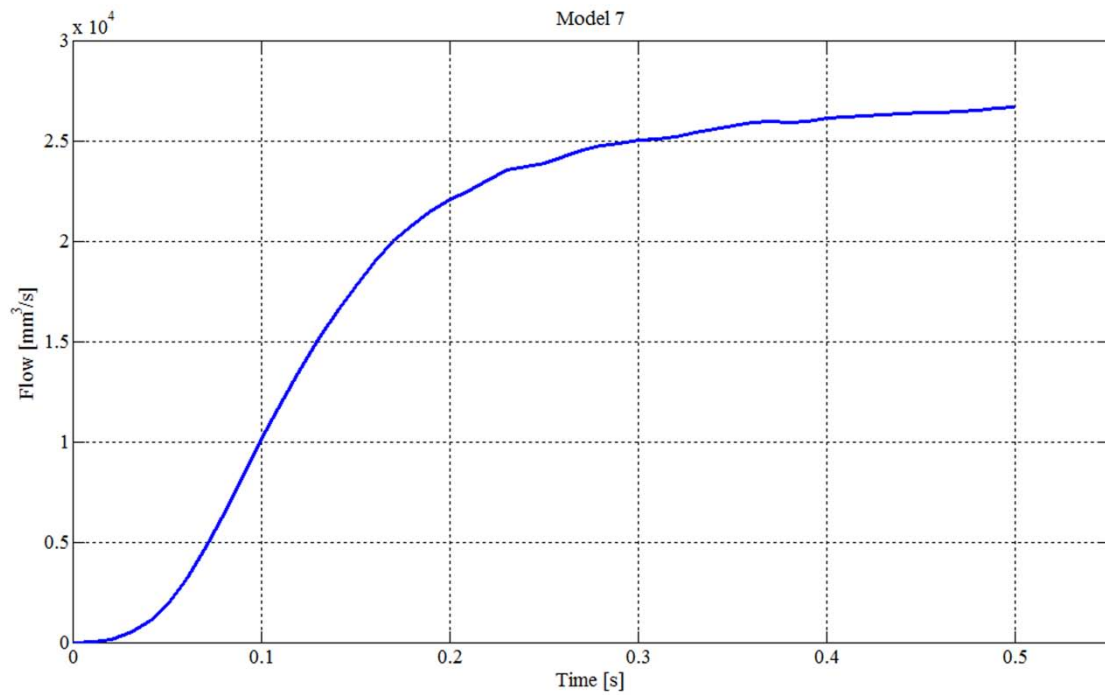

Figure 81 Trend of inlet pressure considering different ratei of pressure, 0.05 kPa/s, 0.1 kPa/s and 0.2 kPa/s.

Considering kinetic energy, it shows in fact that the value reached in all three cases is the same (Figure 82).
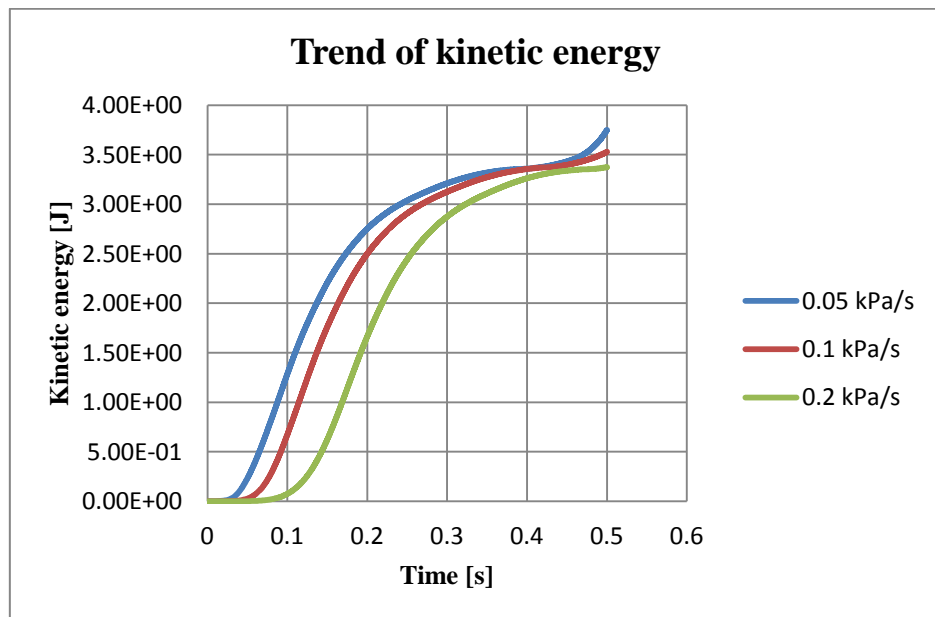
Figure 82 Trend of kinetic energy.

95

To adapt this model to reality the development of urine flow in time is also calculated (Figure 83).

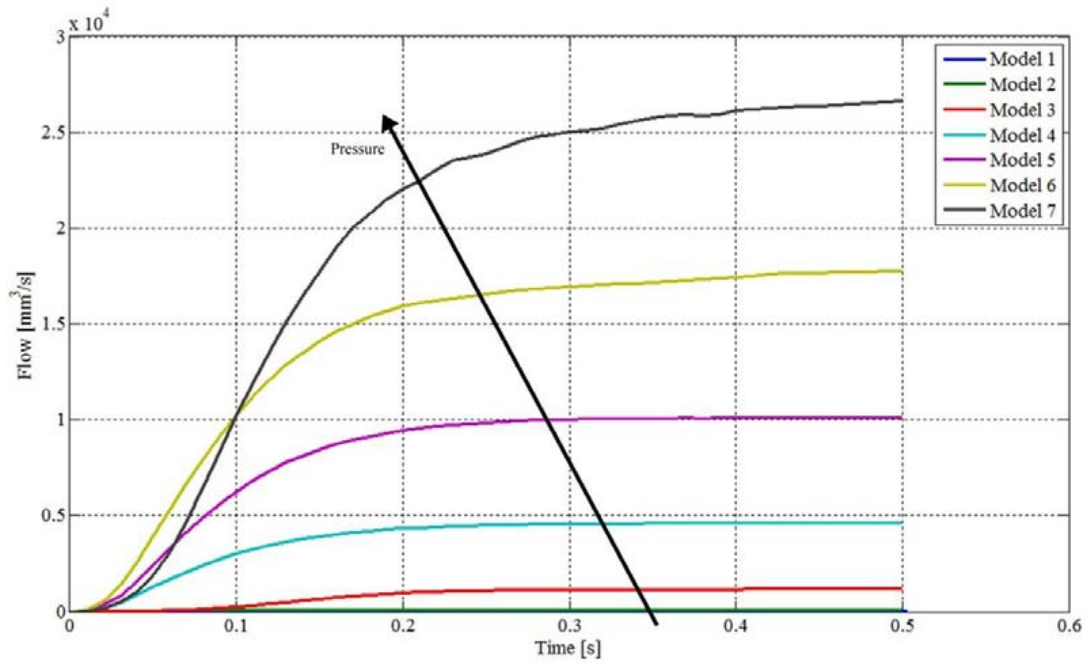**Figure 83** Graphic urine flow-time.

In the first phase urine flow shows a high increase up to stabilization value that results in 26610 mm^3/s that corresponds to 26.61 cm^3/s.

Then different flows are compared and reported in a single graph to compare different flow rates according to the opening of the urethral duct. Figure 84 shows different flows during the time in according to increasing pressure.

Figure 84 Graphic of urine flows-time.

Also the relationship between flow and corresponding pressure is evaluated and reported in the following figure.
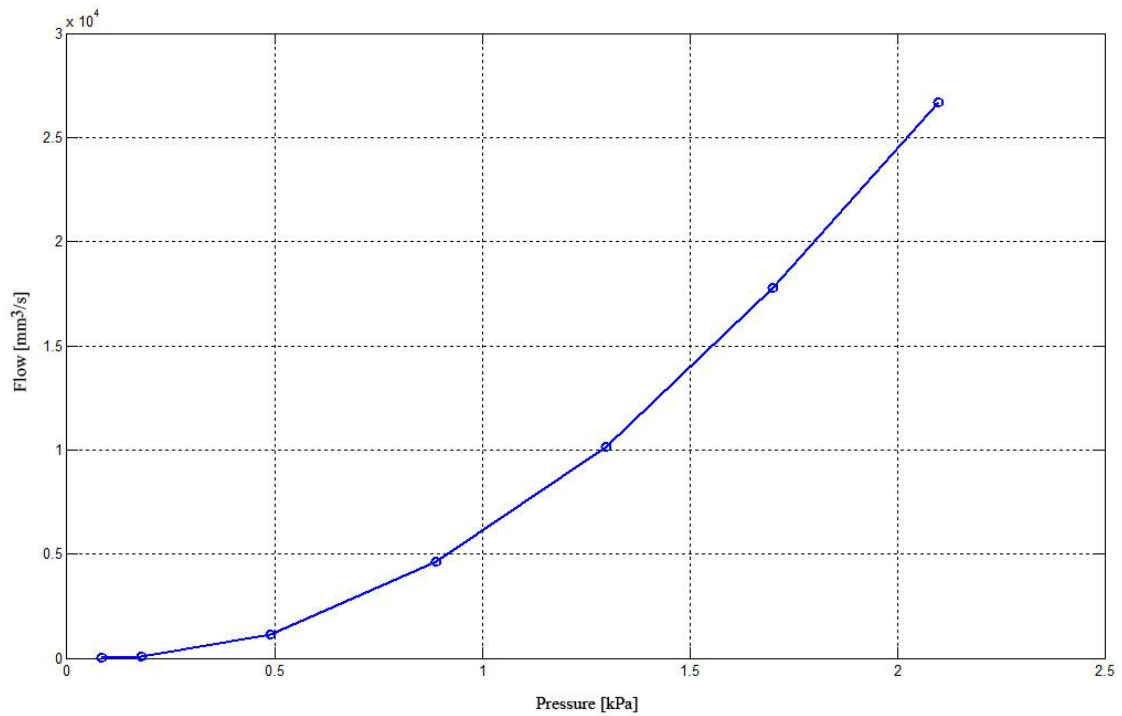

Figure 85 Graphic urine flow-pressure.

CONCLUSION

The aim of this study is to investigate the mechanism of sphincter occlusion and the urine flow conditions during urination through the use of software of finite element Abaqus 6.14 (Dassault Systèmes Simulia Corp., Providence, RI) and with the support of Matlab (The MathWorks Inc., Natick, MA, USA). Starting from analysis already carried out by Natali et al. (2016), based on their experimental tests, the 3D structural models are realized. Little changes are made in respect to the previous analysis and the new 3D models are evaluated.

As described in Chapter 3, Model A is realized to investigate the behavior of the 3D minimal model, starting from 2D model. In this regard 3D elements are used to create an extrusion from 2D model.

Considering Model A, 0.3 mm long, it is realized based on 2D tests, and in actuality the results obtained are similar (Figure 86).
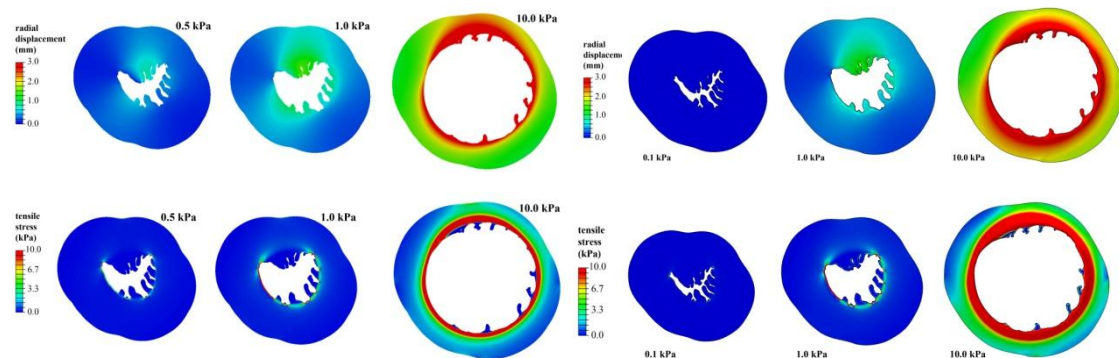
Figure 86 Comparison between 2D-model and 3D-model.

After that, in the same model is added the external pressure of 10 kPa, according to sphincter devices, and results in the volume of the lumen decreasing down to zero, as expected (Figure 87).
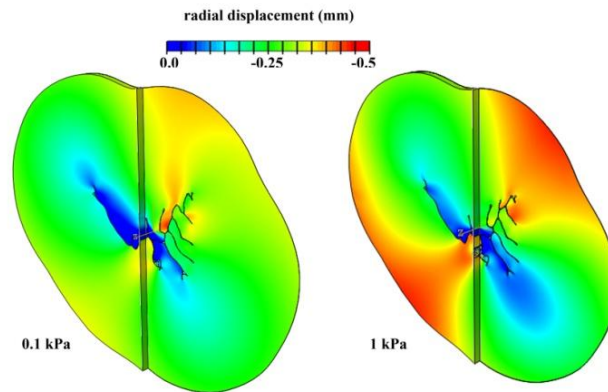
Figure 87 Contour of radial displacement field.

As described in Chapter 3, Model B is realized to test the Matlab program in a longer model with more elements along the longitudinal direction. The model is 3 mm long, with constant external pressure of 10 kPa.

To achieve a more precise analysis, it is also taken into account the internal pressure of 0.5 kPa. Results that the Matlab program works correctly and the model, with all three different intraluminal pressure, reaches the complete occlusion (Figure 88).
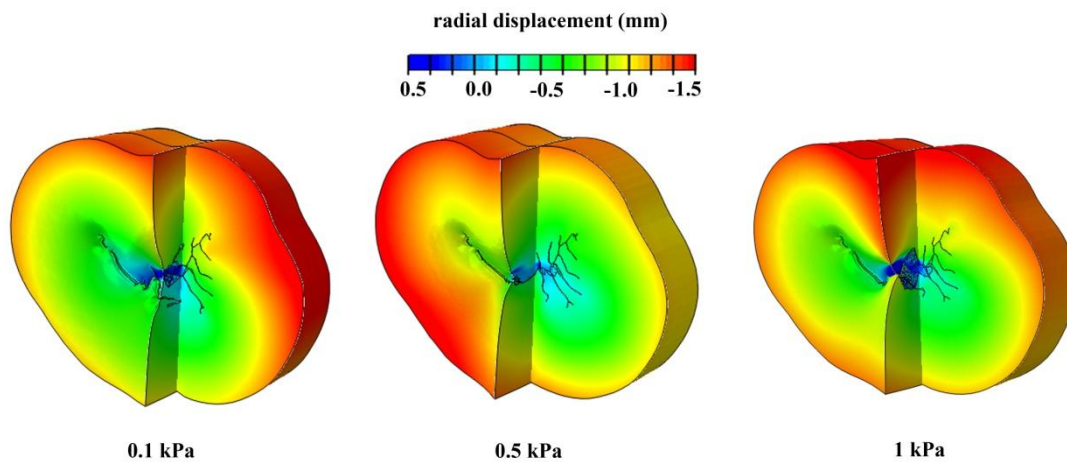
Figure 88 Contour of radial displacement field.

To realize models that are able to mimic the action of the artificial sphincter, models with length of 10 mm and 20 mm are considered. In these models are used different loading conformations, in particular different position of loading and force intensity.

It is decided to consider a greater duct portion, Model C, 10 mm long, to mimic more accurately the real situation. The external pressure is placed in the central portion of the urethral duct (Figure 89).
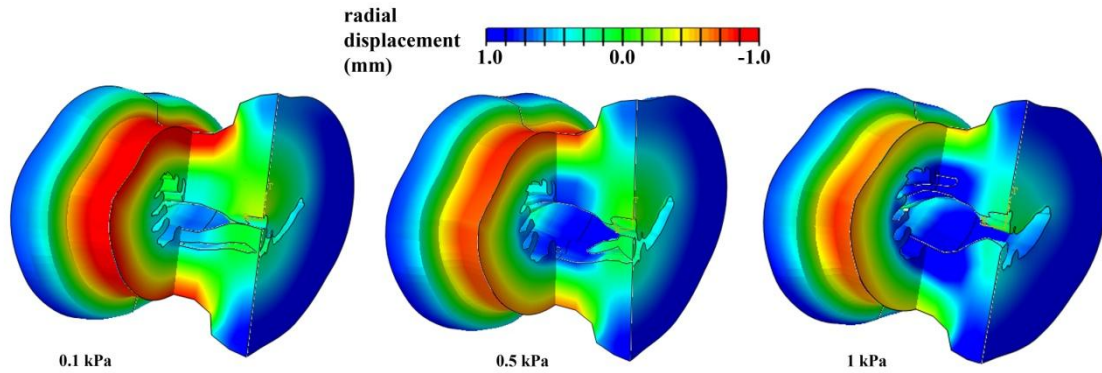
Figure 89 Contour of radial displacement field.

The last Model D, 20 mm long is considered with the aim to evaluate differences between a uniform pressure field and a parabolic pressure field. The present analysis pertains to the consideration of urethral tissues in healthy conditions under different loading configurations, just to represent the effects of different cuff conformations, according to the experience reported by surgical practice. Urethra occlusion is achieved in case of constant load along the overall length of the cuff, while marginal opening is present in border regions when a parabolic trend is assumed. The duct region in contact with borders of the cuff represents, in consideration of the sudden variation of deformational field, a potential source of problems in tissue mechanical response (Figure 90).
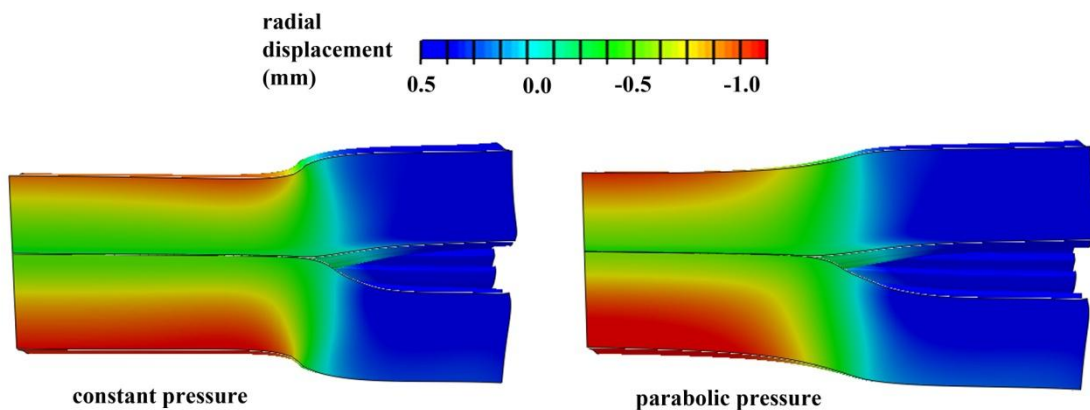
Figure 90 Contour of radial displacement field.

In fact, this condition can produce tissues degradation, because of the permanence of a localized deformation that does not interpret properly the physiological action induced by the natural sphincter.

Considering urine flow condition, different models based on different values of

100

intraluminal pressure are considered. Figure 91 shows the trend of different flows during time, according to increasing pressure.

Increasing the size of the elliptical structure and then the internal pressure, increases the corresponding flow rate. In fact, in Model 1 the flow is very low, such as 0.005 cm^3/s, while in Model 7 the flow reaches significant value such as 26 cm^3/s, that corresponds to a normal flow rate.
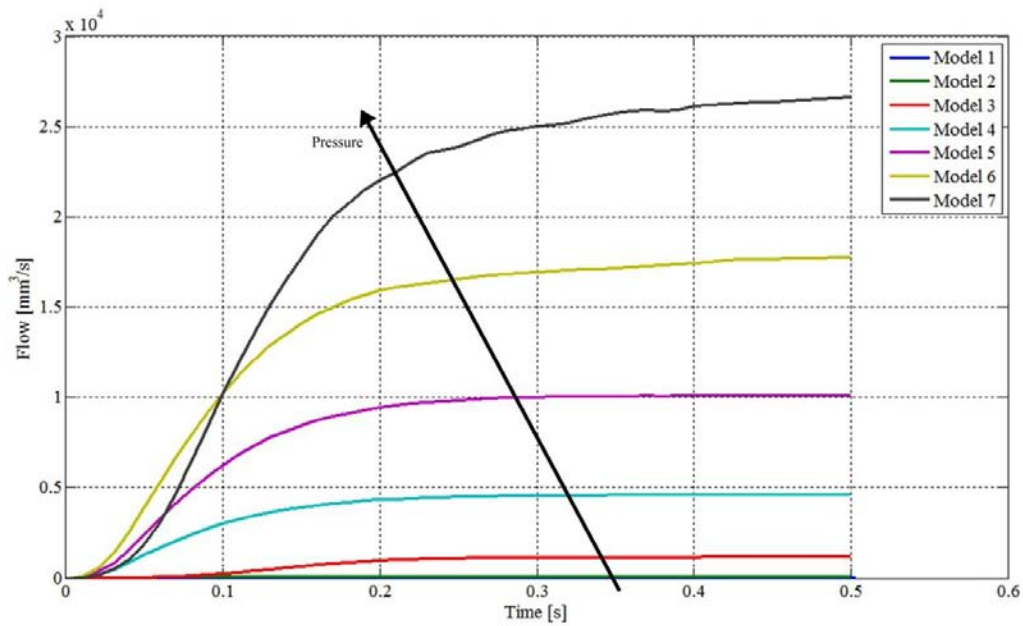
Figure 91 Graphic of urine flows-time.

Moreover, the relationship between flow and corresponding pressure is reported in the following Figure 92.
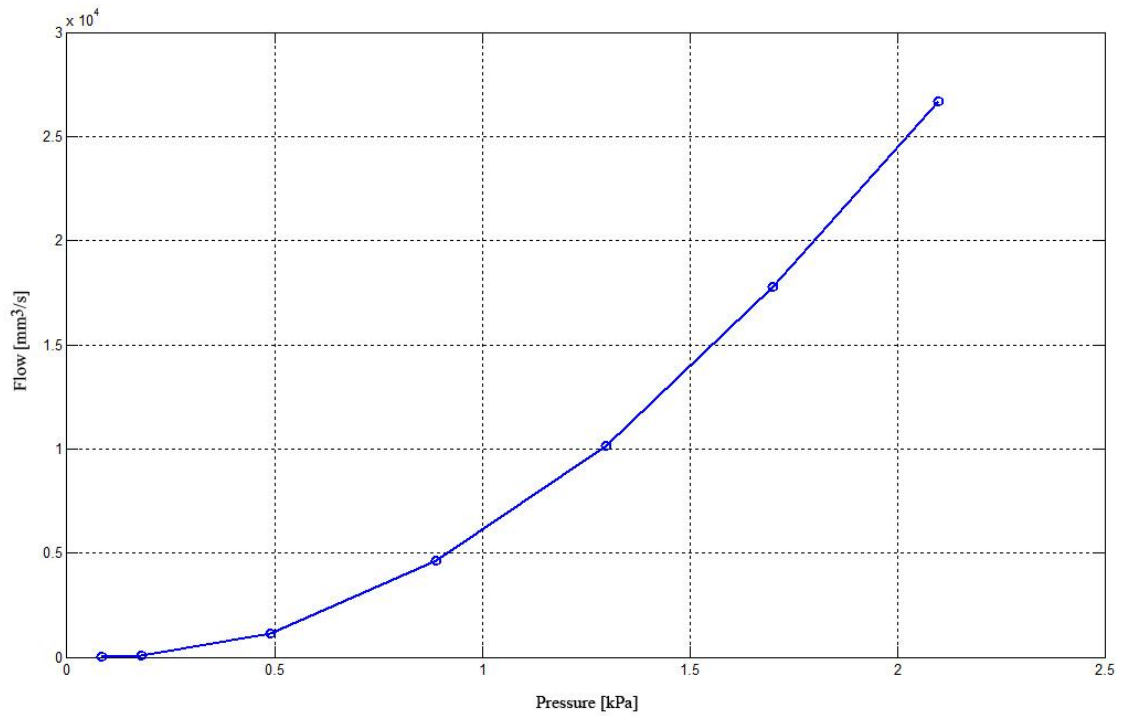
Figure 92 Graphic urine flow-pressure.

Other models with larger dimensions of diameters are considered but it is decided to neglect them because the quantity of flow resulted is too high for the portion of urethral duct that it is considered.

REFERENCES

Aagaard M., Klarskov N., Sønksen J., Bagi P., Colstrup H., Lose G., (2012). **Urethral pressure reflectometry; a novel technique for simultaneous recording of pressure and cross-sectional area: a study of feasibility in the prostatic urethra.** BJU International 110:1178–1183.

Abrams P., Cardozo L., Fall M., Griffiths D., Rosier P., Ulmstern U., van Kerrebroeck P., Victor A., Wein A. (2002). **The standardisation of terminology of lower urinary tract function: report from the Standardisation Sub-committee of the International Continence Society.** Neurourology and Urodynamics 21:167-178.

Arrighi S., Cremonesi F., Bosi G., Domeneghini C. (2004). **Endocrine-paracrine cells of the male urogenital apparatus: a comparative histochemical and immunohistochemical study in some domestic ungulates.** Anatomia Histologia Embryologia 33, 225-232.

Bates, A.S., Martin, R.M., Terry, T.R., (2015). **Complications following artificial urinary sphincter placement after radical prostatectomy and radiotherapy: a meta-analysis.** BJU International 116:623–633.

Brooks, J.D., (2007). **Anatomy of the lower urinary tract and male genitalia.** In: Wein A.J., Kavoussi L.R., Partin A.W., Peters C.A. (Eds.), Campbell-Walsh Urology, 9th edition. Saunders/Elsevier, Philadelphia, pp. 38–77.

Carniel E.L., Rubini A., Frigo A., Natali A.N. (2014a). **Analysis of the biomechanical behaviour of gastrointestinal regions adopting an experimental and computational approach.** Computer Methods and Programs in Biomedicine 113:338-345.

Carniel E.L., Gramigna V., Fontanella C.G., Stefanini C., Natali A.N. (2014b). **Constitutive formulations for the mechanical investigation of colonic tissues.** Journal of Biomedical Materials Research Part A 102, 1243–1254.

Cavalcanti A.G., Costa W.S., Baskin L.S., McAninch J.A., Sampaio F.J. (2007). **A morphometric analysis of bulbar urethral strictures.** BJU International 100:397-402.

Chen J., Ahmad R., Li W., Swain M., Li Q., (2015). **Biomechanics of oral mucosa.** Journal of the Royal Society Interface 12, 20150325.

Clark E.S., Semrad S.D., Bichsel P., Oliver J.E. (1987). **Cystometrography and urethral pressure profiles in healthy horse and pony mares.** *American Journal of Veterinary Research* 48:552-555.

Cordon B.H., Singla N., Singla A.K. (2016). **Artificial urinary sphincters for male stress urinary incontinence: current perspectives.** Journal of Medical Devices 9:175-183.

Dobrin, P.B., (1996). **Effect of histologic preparation on the cross-sectional area of arterial rings.** Journal of Surgical Research 61:413–415.

Dunnick N.R., Sandler C.M., Amis E.S. et al. (1997) **Textbook of uroradiology**, 2nd edn. Williams & Wilkins, Baltimore, pp 465-485.

Gasser T.C., Ogden R.W., Holzapfel G.A. (2006). **Hyperelastic modelling of arterial layers with distributed collagen fibre orientations.** Journal of the Royal Society Interface 3:15-35.

Griffiths, D.J., (1971). **Hydrodynamics of male micturition. I. Theory of steady flow through elastic-walled tubes.** Medical & Biological Engineering 9:581–588.

Hampel C., Thuroff J.W., Gillitzer R. (2010). **Epidemiology and etiology of male urinary incontinence.** Urologe 49:481-488.

Hampel C., Artibani W., Espuña Pons M., Haab F., Jackson S., Romero J., Gavart S., Papanicolaou S. (2004). **Understanding the burden of stress urinary incontinence in Europe: a qualitative review of the literature.** European Urology 46:15-27.

Hussain, M., Greenwell, T.J., Venn, S.N., Mundy, A.R., (2005). **The current role of the artificial urinary sphincter for the treatment of urinary incontinence.** Journal of Urology 174: 418–424.

Landefeld C.S., Bowers B.J., Feld A.D., Hartmann K.E., Hoffman E., Ingber M.J., King J.T., McDougal W.S., Nelson H., Orav E.J., Pignone M., Richardson L.H., Rohrbaugh R.M., Siebens H.C., Trock B.J. (2008). **National Institutes of Health State-of-the-Science conference statement: prevention of fecal and urinary incontinence in adults.** Annals of Internal Medicine 148:449-58.

Natali A.N., Carniel E.L., Fontanella C.G., Frigo A., Todros S., Rubini A., De Benedictis G.M., Cerruto M.A., Artibani W. (2016a). **Mechanics of the urethral duct: tissue constitutive formulation and structural modeling for the investigation of lumen occlusion.** Biomechanics and Modeling in Mechanobiology.

Natali A.N., Carniel E.L., Frigo A., Pavan P.G., Todros S., Pachera P., Fontanella C.G., Rubini A., Cavicchioli L., Avital Y., De Benedictis G.M. (2016b). **Experimental investigation of the biomechanics of urethral tissues and structures.** Experimental Physiology 101.5:641-656.

Natali A.N., Carniel E.L., Gregersen H. (2009). **Biomechanical behaviour of oesophageal tissues: Material and structural configuration, experimental data and constitutive analysis.** Medical Engineering and Physics 31, 1056-1062.

Natali A.N., Fontanella C.G., Carniel E.L. (2010). **Constitutive formulation and analysis of heel pad tissues mechanics.** Medical Engineering and Physics 32:516–522.

Natali A.N., Carniel E.L., Fontanella C.G., Todros S., De Benedictis G.M., Cerruto M.A., Artibani W. **Urethral lumen occlusion by artificial sphincteric devices: a computational biomechanics approach.**

Ostrowski I., Sledz E., Ciechan J., Golabek T., Bukowczan J., Przydacz M., Wiatr T., Stangel-Wojcikiewicz K., and Chlosta P.L. (2015). **Current interventional management of male stress urinary incontinence following urological procedures.** Central European Journal Of Urology, 68(3):340-347.

Pavlica P., Barozzi L., Menchi I. (2003). **Imaging of male urethra.** European Radiology 13:1583-1596.

Pozor M.A., McDonnell S.M. (2002). **Ultrasonographic measurements of accessory sex glands, ampullae, and urethra of normal stallions of various size types.** Theriogenology 58:1425-1433.

*Prinz J.F., de Wlijk R.A., Huntjens L., (*2007). **Load dependency of the coefficient of friction of oral mucosa.** Food Hydrocolloids 21:402–408.

Pullan, B.R., Phillips, J.I., Hickey, D.S., (1982). **Urethral lumen cross-sectional shape: its radiological determination and relationship to function.** BJU International 54:399–407.

Raub C.B., Mahon S., Narula N., Tromberg B.J., Brenner M., George S.C., (2010). **Linking optics and mechanics in an in vivo model of airway fibrosis and epithelial injury.** Journal of Biomedical Optics 15, 015004.

Wolfe D.F., Moll H.D. (1999). **Large animal urogenital surgery.** Baltimore MD, Williams & Wilkins.